



Dissertation

The purification of fermentatively produced hydrogen using gas permeation: A practical and simulative approach

ausgeführt zum Zwecke der Erlangung des akademischen Grades eines Doktors der
technischen Wissenschaften unter der Leitung von

Univ.Prof. Dipl.-Ing. Dr.techn. Anton Friedl

Ass.Prof. Dipl.-Ing. Dr.techn. Michael Harasek

E166

Institut für Verfahrenstechnik, Umwelttechnik und Technische Biowissenschaften

eingereicht an der Technischen Universität Wien

Fakultät für Maschinenwesen und Betriebswissenschaften

von

Tino Georg Lassmann

Matrikel Nummer: 0325476

Adresse: Thurnhofstraße 10, 9620 Hermagor

Wien, am _____

Tino Georg Lassmann

Prüfungskomitee:

Vorsitzender: Ao.Prof. Dr. WINTER, Franz

1.Prüfer: Prof. Dr. FRIEDL, Anton

2.Prüfer: Ao.Prof. Dr. NARODOSLAWSKY, Michael

Fachgebiete der Dissertation: MEMBRANTECHNIK

“Ich bin immer noch verwirrt, aber auf einem höheren Niveau.“

„I’m still confused – but on a higher level.“

Enrico Fermi

ABSTRACT

Today, there is an indispensable need in alternatives to fossil energy sources because its availability is timely limited. In addition to the sooner or later arising availability shortage, environmental effects caused by the utilization of fossil fuels are essential driving forces in pursuing a sustainable alternative. In this context, hydrogen is often mentioned as one of the most promising energy carriers of the near future and it is seen as potential emission-free fuel in the transportation sector. Unfortunately, most common hydrogen production methods are either based on fossil fuels or the energy intensive water electrolysis. These methods cannot fulfill modern energy provision requirements, because they are neither sustainable nor energy efficient. One possibility of a sustainable and energy efficient hydrogen production is the biotechnological pathway of dark fermentation, where biomass can be used to generate a hydrogen-rich gas. Besides hydrogen as main component carbon dioxide is also generated with its ratio depending on the respective process conditions. The carbon dioxide in the gas is considered as a contaminant and has to be separated subsequently to obtain pure hydrogen as a final product. Typically used hydrogen purification methods are amine absorption and pressure swing adsorption. These large-scale industry methods are well-established and may be suitable from a technological point of view. But, with gas capacities, compositions, and conditions different from typical applications, these methods might not be suitable for the purification of dark fermentation gas regarding their energy efficiency. For this particular application membrane technology seems to be very promising because gas permeation is a simple, flexible, and even mobile purification method. It is also characterized by a low energy requirement and low investment costs. Therefore, the goal of this work was to investigate the applicability of gas permeation for the purification of a dark fermentation gas. An innovative small scale process to upgrade the hydrogen rich gas was designed, with special attention to a flexible and energy-efficient separation process setup. Two areas of research were covered: an experimental investigation of commercially available membrane material, and a simulative investigation of different process setups. The experimental part included assembly and testing of membrane modules in the laboratory, using either PI or PP hollow fibers as membrane material. Pure gas measurements for PI membrane modules resulted in ideal H_2/CO_2 selectivities in the range of 3.45 to 3.91. Compared to that, using PP membrane material never surpassed an ideal H_2/CO_2 selectivity of 2.7, which made them unsuitable for the given purification task. Further investigation of PI membrane modules included measurements with two different mixtures, a binary with 66 vol% H_2 and 34 vol% CO_2 , and a ternary with 40 vol% H_2 , 30 vol% CO_2 and 30 vol% N_2 . These investigations showed that for binary or ternary gas mixtures the respective H_2/CO_2 selectivities decreased to values in the range of 2.29 - 2.49 or 2.43 -

2.7, respectively. The laboratory tests were followed by the design of a separation process to set up a small scale pilot plant. This pilot plant was then connected to a hydrogen fermenter and the obtained information on process data and gas qualities confirmed the results from laboratory measurements. Based on the experimental work it can be concluded that an actual online fermenter gas upgrading is possible. In the simulative part of this work, the simulation tool Aspen Custom Modeler[®] was used to develop a gas permeation unit operation which was implemented into the flow sheeting and process optimization software Aspen Plus[®] at a later stage. This single-stage model was successfully validated and used to design various multi-stage processes in Aspen Plus[®]. Implementing a second (setups 1 and 2) and third stage (setup 4) into the process resulted in a H₂-recovery increase compared to a single-stage configuration. The models were able to display the behavior of the membranes due to changing process conditions, but when using H₂-selective membranes the achievable product quality was unfortunately not reached. Compared to setups 1 and 2, the utilization of CO₂-selective membranes (setup 3) did reach the required product purity of at least 98 vol%. It furthermore resulted in a lower specific energy demand. All in all, the purification of fermentatively produced hydrogen to a hydrogen combustion engine suitable gas quality could only be maintained with CO₂-selective material. Possible scenarios for the off-gas utilization were developed, to gain insight into the available unused energy potential. For all four multi-stage setups, it was shown that a thermal utilization of the off-gas' energy content could provide a significant amount of heat and power. In conclusion, this thesis showed that the utilization of commercially available membrane material has its possibilities but also its restrictions. Regarding sustainability and emission reduction, this pathway of fermentative hydrogen with subsequent membrane purification seems very promising.

KURZFASSUNG

Heutzutage ist es eine unabdingbare Notwendigkeit eine Alternative zu fossilen Energiequellen zu finden, da ihre Verfügbarkeit zeitlich begrenzt ist. Neben dem früher oder später eintretenden Engpass an fossilen Brennstoffen, so sind ihre Umweltauswirkungen eine weitere Triebkraft für die Suche nach einer nachhaltigen Alternative. Wasserstoff wird in diesem Zusammenhang gerne als ein vielversprechender Energieträger der Zukunft angesehen. Jedoch sind die gängigen Methoden zur Wasserstoffproduktion entweder auf fossilen Brennstoffen basierend oder mittels der energieintensiven Elektrolyse von Wasser. Diese Methoden erfüllen aber nicht die Grundvoraussetzungen für eine moderne Energiebereitstellung, denn sie sind weder nachhaltig noch energieeffizient. Eine Möglichkeit für eine nachhaltige und energieeffiziente Wasserstoffproduktion ist der biotechnologische Weg der Dunkelfermentation, in der Biomasse verwendet wird um ein wasserstoffreiches Gas herzustellen. Je nach Prozessbedingungen wird neben dem Hauptbestandteil Wasserstoff auch noch ein entsprechender Anteil an Kohlendioxid produziert. Das Kohlendioxid im Gas wird als Verunreinigung angesehen und muss daher nachfolgend abgetrennt werden um reinen Wasserstoff als Endprodukt zu erhalten. Typische Trenntechniken in der Wasserstoffreinigung sind die Aminwäsche und die Druckwechsel Adsorption. Diese in der Industrie großtechnisch etablierten Anwendungen sind aus technischer Sicht sehr gut geeignet. Da sich aber die Gas-Kapazitäten, Gas-Zusammensetzungen, und Betriebsbedingungen von typischen Anwendungen unterscheiden, sind diese bezüglich der benötigten Energieeffizienz nicht für die Aufbereitung von Fermentationsgas geeignet. Für diesen speziellen Anwendungsfall könnte das Membrantrennverfahren vielversprechende Ergebnisse erzielen, da Gaspermeation ein einfaches, flexibles, und mobiles Trennverfahren ist. Des Weiteren charakterisiert sich dieses durch einen niedrigen Energiebedarf und geringe Investitionskosten. Das Ziel dieser Arbeit war es daher die Anwendbarkeit von Gaspermeation für die Reinigung eines Fermentationsgases zu untersuchen. Ein innovativer klein-industrieller Prozess zur Aufbereitung eines wasserstoffreichen Gases wurde entworfen, mit speziellem Augenmerk auf einen flexiblen und energieeffizienten Trennprozess. Dabei wurden zwei Bereiche abgedeckt: die experimentelle Untersuchung von kommerziell erhältlichen Membranmaterialien und die simulationstechnische Untersuchung von verschiedenen Membrananordnungen. Der experimentelle Teil inkludierte die Anfertigung von Membranmodulen unter Verwendung von Polyimid (PI) oder Polypropylen (PP) Hohlfasermembranen und deren Überprüfung unter Laborbedingungen. Die Reingasmessungen für PI Membranmodule ergaben ideale H_2/CO_2 -Selektivitäten im Bereich von 3.45 bis 3.91. Im Vergleich dazu konnte mit PP Membranmaterial eine ideale H_2/CO_2 -Selektivität von

2.7 nie übertroffen werden, was sie wiederum für die gegebene Reinigungsaufgabe ungeeignet machte. Weitere Untersuchungen der PI Membranmodule enthielten Messungen mit zwei verschiedenen Gasmischungen, einem binären Gemisch mit 66 vol% H₂ und 34 vol% CO₂ und einem ternären Gemisch mit 40 vol% H₂, 30 vol% CO₂ und 30 vol% N₂. Diese Untersuchungen zeigten, dass für die binären oder ternären Gasgemische die jeweiligen H₂/CO₂-Selektivität auf Werte im Bereich von 2.29 bis 2.49 bzw. 2.43 bis 2.7 sanken. Auf die Labortests folgte die Entwicklung eines Trennprozesses der als Grundlage für den Bau einer klein-maßstäblichen Versuchsanlage diente. Nachfolgend wurde die Versuchsanlage an einen Wasserstoff-Fermenter angeschlossen. Die daraus gewonnen Informationen der Prozessparameter und Gasqualitäten gingen mit denen der Labortests einher. Daraus konnte der Schluss gezogen werden, dass eine Online-Aufbereitung des Fermentationsgases realisierbar ist. Im simulationstechnischen Teil der Arbeit wurde mittels der Simulationssoftware Aspen Custom Modeler[®] eine Gaspermeations-Grundoperationseinheit entwickelt, welche zu einem späteren Zeitpunkt in das Fließschema- und Prozessoptimierungs-Programm Aspen Plus[®] implementiert wurde. Die Validierung dieses einstufigen Modells war erfolgreich und es konnte zur Untersuchung verschiedener Mehrstufenkonzepte in Aspen Plus[®] verwendet werden. Die Implementierung einer zweiten (Setups 1 und 2) und dritten Stufe (Setup 4) in den Prozess führte zu einem H₂-Recovery-Anstieg verglichen mit einer einstufigen Konfiguration. Mittels der Modelle war es möglich das Verhalten der Membranen unter wechselnden Prozessbedingungen zu simulieren. Jedoch ergab sich, dass bei der Verwendung der betrachteten H₂-selektiven Membranen die erforderliche Produktqualität nicht erreicht werden konnte. Im Gegensatz zu Setups 1 und 2 führte die Verwendung von CO₂ selektive Membranen (Setup 3) zur gewünschten Produktreinheit von mindestens 98 vol% H₂. Des Weiteren resultierte diese Variante in einen geringeren spezifischen Energiebedarf. Alles in allem ließ sich erkennen, dass die Aufreinigung von fermentativ produziertem Wasserstoff zu einer für den Wasserstoff-Verbrennungsmotor geeigneten Gasqualität unter den gegebenen Voraussetzungen nur mittels CO₂-selektiven Materials zu erreichen ist. Eine Analyse für die Möglichkeiten der Abgasverwertung wurde ebenfalls durchgeführt um einen Einblick in das ungenutzte Energiepotential der anfallenden Abgasströme zu bekommen. Es zeigte sich, dass der Energiegehalt in den Abgasströmen der jeweiligen Prozesskonfigurationen für die Bereitstellung von Strom und Wärme genutzt werden kann. Trotz alledem scheint dies in Bezug auf Nachhaltigkeit und Emissionsreduzierung ein sehr vielversprechender Weg zu sein. Zusammenfassend zeigt diese Arbeit, dass die Verwendung von Membranen zur Aufbereitung von fermentative hergestelltem Wasserstoff eine vielversprechende Variante darstellt, speziell im Hinblick auf Nachhaltigkeit und Emissionsreduktion.

ACKNOWLEDGEMENT

I wish to thank, first and foremost, my Professors Anton Friedl and Michael Harasek for their support and trust in my capabilities. During the course of this work they pushed me to find the right solutions and showed a lot of patience with me...

I would also like to show my deepest gratitude to Dr. Martin Miltner – it was a great honor working with you. All of this would never have been possible without our support.

It is a pleasure to thank Antonia Rom, Angela Miltner, Adela Drljo, Elke Ludwig, Orestis Almpanis Lekkas, Ala Modarresi, Felix Weinwurm, Walter Wukovits and Marcus Hrbek – you are more than just colleges to me.

Furthermore, I would like to express my deepest appreciation to my friends, Hannes, Felix, Michael, Jan, and Marc. Special thanks to Markus for keeping me on track and always giving me the right perspective.

Thank you to Sarah, for being the kind and loving person you are.

Last but not least, I owe a very important debt to my family - especially my mother Veronika and my brother Sandro, who never stopped supporting the everlasting student.

This doctoral thesis is dedicated to my late father, Dr. Georg Lassmann.

TABLE OF CONTENT

List of Publications	IX
List of Figures	X
List of Tables	XII
List of Symbols	XIV
Abbreviations	XVIII
1. Motivation	1
2. Introduction	3
2.1 Production, purification and storage of hydrogen	3
2.1.1. State of the art in hydrogen production.....	3
2.1.2. Hydrogen market	11
2.1.2.1. Hydrogen on a renewable basis	13
2.1.3. Purification of renewable hydrogen from bioprocesses	13
2.1.3.1. Absorptive CO ₂ separation techniques	14
2.1.3.2. Adsorptive CO ₂ separation techniques	17
2.1.3.3. Cryogenic separation techniques	18
2.1.3.4. Membrane separation techniques	18
2.1.3.5. Emerging technologies for CO ₂ capture	18
2.1.4. Storage of hydrogen	19
2.1.5. Power to gas concept.....	21
2.2 Utilization of hydrogen	22
2.2.1. Hydrogen for industrial use.....	23
2.2.2. Hydrogen as fuel.....	24
2.2.2.1. Direct use in combustion engines	25
2.2.2.2. Hydrogen fuel cell	25
2.3 Standards for hydrogen utilization	27
3. Aim of this work	29
4. Description of the overall process	30
4.1 Fermentative production of hydrogen	31
4.2 Membrane separation for H ₂ purification: In general.....	35
4.2.1. Membrane material	35
4.2.1.1. H ₂ -selective membrane material	35
4.2.1.2. CO ₂ -selective membrane material	38
4.2.2. Membrane modules.....	39
4.3 Membrane separation for H ₂ purification: Selected system	42
4.4 Off gas utilization.....	43

5. Materials & Methods	44
5.1 Experimental part.....	44
5.1.1 Assembly of membrane modules.....	44
5.1.1.1 Prearrangement.....	44
5.1.1.2 End outlet potting.....	45
5.1.1.3 Description of the modules.....	47
5.1.2 Material screening and membrane module testing.....	47
5.1.2.1 Module testing rig ‘GP2’.....	48
5.1.2.2 Procedure of pure gas tests.....	49
5.1.2.3 Procedure of gas mixture tests.....	50
5.1.3 Small scale pilot plant.....	52
5.1.4 Fermenter.....	55
5.1.4.1 Fermenter design, utilized bacteria and operational conditions.....	55
5.1.4.2 Gas analysis tool AwiFLEX [®]	57
5.1.5 Online gas separation with small scale pilot plant.....	57
5.1.5.1 Online gas separation field tests.....	57
5.1.6 Data Reconciliation with MatLab [®]	58
5.1.6.1 Data reconciliation principle.....	58
5.1.6.2 Data reconciliation for membrane module measurements.....	60
5.2 Simulative part.....	65
5.2.1 Principles of Gas Permeation.....	65
5.2.1.1 Gas transport in dense membranes.....	65
5.2.1.2 Temperature dependency.....	67
5.2.1.3 Concentration polarization and plasticization.....	67
5.2.1.4 Pressure drop in hollow fiber membranes.....	70
5.2.2 Simulation software (ACM, Aspen Plus).....	70
5.2.3 Single-stage module.....	71
5.2.3.1 ACM base case model: Counter-current operational mode.....	71
5.2.3.2 ACM base case model: Co-current operational mode.....	73
5.2.3.3 Comparison of the counter-current and co-current operational mode.....	74
5.2.3.4 ACM detailed model: Counter-current operational mode.....	75
5.2.3.5 Implementation into Aspen Plus [®]	76
5.2.3.6 Determination of multi-component permeances with Aspen Plus [®] model.....	76
5.2.4 Multi-stage processes in Aspen Plus [®] based on counter-current modules.....	76
5.2.4.1 Two-stage process in Aspen Plus [®] : Setup 1.....	78
5.2.4.2 Two-stage process in Aspen Plus [®] : Setup 2.....	78
5.2.4.3 Two-stage process in Aspen Plus [®] : Setup 3.....	79
5.2.4.4 Three-stage process in Aspen Plus [®] : Setup 4.....	79
5.2.4.5 Membrane area variation for two-stage processes.....	80
5.2.4.6 Membrane area variation for three-stage processes.....	81
5.3 Validation of the single-stage module.....	81
5.3.1 Validation via measurements.....	82
5.3.2 Validation due to comparison with Makaruk&Harasek model.....	83
5.3.3 Verification of the ACM detailed model by comparison with CFD simulation.....	84

6. Results & Discussion.....	86
6.1 Experimental part	86
6.1.1 Pure gases.....	86
6.1.1.1 Comparison of membrane modules	89
6.1.1.2 Temperature dependency of the permeances	92
6.1.2 Gas mixtures	94
6.1.2.1 Feed gas mixture: 66/34/0	95
6.1.2.2 Feed gas mixture: 30/30/40	96
6.1.2.3 Comparison of pure gases and gas mixtures.....	98
6.1.3 Integrated gas separation.....	101
6.1.3.1 Fermentation.....	102
6.1.3.2 Purification with small-scale pilot plant	103
6.1.3.3 Comparison of the utilized membrane modules before and after field tests	104
6.1.4 Application of data reconciliation.....	106
6.2 Simulative part	108
6.2.1 Single stage	108
6.2.1.1 Influence of number of cells	108
6.2.1.2 Comparison of counter-current and co-current operational mode	111
6.2.2 Validation of the ACM base case model.....	112
6.2.2.1 Validation via experimental data	113
6.2.2.2 Validation due to comparison with Makaruk&Harasek model.....	113
6.2.2.3 Verification of the ACM detailed model by comparison with CFD simulation ..	114
6.2.3 Multi-stage	117
6.2.3.1 Membrane area variation	117
6.2.3.2 Comparison of different setups.....	118
6.2.4 Utilization of the off-gas	121
7. Summary and conclusion	123
8. Outlook	126
References.....	127
Appendix.....	XXII
A. Fermentation.....	XXII
B. Measurement data	XXIV
B.1 Pure gas measurements	XXIV
C. SEM pictures of fibers.....	XXVII
C.1 Polyimide fibers	XXVII
C.2 Polypropylene fibers	XXVIII

LIST OF PUBLICATIONS

Journal Articles:

Haddadi, B., Jordan, C., Schretter, P., Lassmann, T., Harasek, M., 2016, “*Designing Better Membrane Modules Using CFD*”; Chemical Product and Process Modeling, manuscript accepted for publication

Lassmann, T., Miltner, M., Harasek, M., Makaruk, A., Wukovits, W., Friedl, A. “*The purification of fermentatively produced hydrogen using membrane technology: a simulation based on small-scale pilot plant results*”; Clean Technologies and Environmental Policy, (2015), 1-8.

Lassmann T., Kravanja P., Friedl A.: “*Simulation of the downstream processing in the ethanol production from lignocellulosic biomass with ASPEN Plus® and IPSEpro*”; Energy, Sustainability and Society, 4 (2014), 7.

Lassmann T., Kravanja P., Friedl A.: “*Downstream Prozess in der Bioethanol Produktion aus lignozellulosehaltigen Rohstoffen*”; Chemie Ingenieur Technik, 84 (2012), 8, 1307 - 1308.

Lassmann T., Kravanja P., Friedl A.: “*Prozesssimulation der Produktion von Ethanol und Methan aus lignocellulosehaltigen Rohstoffen*”; Chemie Ingenieur Technik, 83 (2011), 10, 1609 - 1617.

LIST OF FIGURES

Figure 2.1: Technological routes in hydrogen production based on feedstock	4
Figure 2.2: Global hydrogen production and utilization in 2008, based on a total hydrogen production of approximately 50 Mt per year	12
Figure 4.1: Overall process with allocation of the H ₂ MemClean project partners' main competences....	30
Figure 4.2. Pathways for fermentative hydrogen production; picture taken from [Ren, et al., 2006].....	32
Figure 4.3: Scheme of H ₂ -selective material.....	36
Figure 4.4: Principle of CO ₂ -selective material	38
Figure 4.5: Schematic illustration of a hollow fiber module with shell-side feed operational mode and the possibly utilization of a sweep gas.....	40
Figure 4.6: Schematic illustration of a hollow fiber module with dead end shell-side feed geometry.....	40
Figure 4.7: Schematic illustration of a hollow fiber module with bore-side feed geometry	41
Figure 4.8: Counter-current operational mode in a pore side feed membrane module.....	41
Figure 4.9: Co-current operational mode in a pore side feed membrane module.....	42
Figure 5.1: Hollow fiber membrane module, with declaration of different length types	45
Figure 5.2: Assembly of the membrane modules.....	46
Figure 5.3: Potting of the membrane modules.....	46
Figure 5.4: Flow sheet of the test rig used for analysis of the membrane modules	48
Figure 5.5: Membrane test rig GP2 at the Vienna University of Technology, with a detailed view on the control unit.....	49
Figure 5.6: Flow sheet of the small scale pilot plant.....	54
Figure 5.7: Declaration of measured and unmeasured values for DR	61
Figure 5.8: Sample scheme for the multi-resistance model considering a hollow fiber membrane.....	68
Figure 5.9: Scheme of the model routine for the ACM models	71
Figure 5.10. Example graph of the countercurrent model.....	72
Figure 5.11: Example graph of the co-current model.....	73
Figure 5.12: Setup 1, with two-stage configuration and H ₂ -selective membranes	78
Figure 5.13: Setup 2, with two-stage configuration and H ₂ -selective membranes	79
Figure 5.14: Setup 3, with two-stage configuration and CO ₂ -selective membranes.....	79
Figure 5.15: Setup 4, with three-stage configuration and H ₂ -selective material.....	80
Figure 5.16: Design of a single fiber for CFD simulation in OpenFoam [®] , designed by Schretter, P. [2015].....	84
Figure 6.1: Membrane module M-1 - Influence of temperature and pressure difference on trans- membrane flow of H ₂ and CO ₂	87
Figure 6.2: Membrane module M-1 - H ₂ /CO ₂ selectivity and H ₂ volume flow against the pressure difference at three different temperature levels (30°C, 40°C, 50°C).....	87
Figure 6.3: Membrane module M-2 - Influence of temperature and pressure difference on trans- membrane flow of H ₂ and CO ₂	90
Figure 6.4: Membrane module M-3 - Influence of temperature and pressure difference on trans- membrane flow of H ₂ and CO ₂	90
Figure 6.5: Membrane module M-4 - Influence of temperature and pressure difference on trans- membrane flow of H ₂ and CO ₂	91
Figure 6.6: Temperature dependency of permeance for PI membranes M-1, M-2, M-3 with linear regression for Arrhenius equation.....	93

Figure 6.7: Temperature dependency of permeance for PP membrane M-4 with linear regression for Arrhenius equation	93
Figure 6.8: H ₂ -recovery and H ₂ -purity in a single-stage for the 66-34-0 feed gas mixture depending on the stage cut; all data is taken from laboratory results	96
Figure 6.9: H ₂ and CO ₂ permeances depending on temperature, Arrhenius equation for 66-34-0 mixture	96
Figure 6.10: H ₂ -recovery and H ₂ -purity in a single-stage for the 30-30-40 feed gas mixture depending on the stage cut; all data are taken from laboratory results	97
Figure 6.11: H ₂ , CO ₂ and N ₂ permeances depending on temperature, Arrhenius equation for 30-30-40 mixture	98
Figure 6.12: Fermenter gas composition over time during online gas separation	102
Figure 6.13: Fermenter gas composition for different measurements	103
Figure 6.14: H ₂ -recovery and H ₂ -purity during online gas separation measurements depending on the stage cut	104
Figure 6.15: ACM calculation of H ₂ and CO ₂ content in the permeate and retentate flow for three different number of cells; base case model with counter-current operational mode	109
Figure 6.16: ACM calculation of the hydrogen partial pressure in the retentate for three different numbers of cells; base case model with counter-current operational mode	109
Figure 6.17: ACM calculation of the hydrogen partial pressure in the permeate for three different numbers of cells; base case model with counter-current operational mode	110
Figure 6.18: Simulation results of H ₂ -recovery and H ₂ -purity depending on the stage cut for binary and ternary feed gas mixtures; Comparison of counter-current and co-current operational mode	111
Figure 6.19: Simulation results for the correlation between H ₂ -purity in the permeate and H ₂ -recovery for binary and ternary feed gas mixtures; Comparison of counter-current and co-current operational mode	112
Figure 6.20: Validation of the ACM base case model with measurements	113
Figure 6.21: Comparison of ACM and CFD results for permeate composition depending on the stage cut	115
Figure 6.22: Comparison of ACM and CFD results, with detailed look at H ₂ and CO ₂ composition in the permeate depending on the stage cut	115
Figure 6.23: Comparison of ACM and CFD results, pressure drop over the fiber length for different gas flows	116
Figure 6.24: CFD results, H ₂ concentration gradient outside (left) and inside (right) the fiber	117
Figure 6.25: Results of the sensitivity analysis with varying membrane areas at stage one (A ₁) and two (A ₂) for setups 2 and 3	118
Figure A.1: Fermentation, H ₂ yield over course of time, including malfunctions during operation	XXII
Figure C.1: SEM pictures of the utilized polyimide fibers, magnification: upper left x500, upper right x3000, lower left x3000, lower right x16000	XXVII
Figure C.2: SEM pictures of the utilized polypropylene fibers, magnification: left x93, right x500 ..	XXVIII

LIST OF TABLES

Table 2.1: Characteristics for hydrogen purity based on ISO 14687:1999 of the ISO/TC 197	28
Table 5.1: Description of the homemade membrane modules with commercial fiber material.....	47
Table 5.2: Parameters for the membrane module pure gas tests.....	50
Table 5.3: Composition of the test gases applied for membrane testing.....	51
Table 5.4: Parameters for the membrane module mixed gas tests.....	51
Table 5.5: Presumed conditions and composition of the fermentation gas for the design of the mobile small scale pilot plant.....	53
Table 5.6: Characterization of the utilized substrate.....	55
Table 5.7: Thermophilic fermentation conditions, utilized nutrient salt and inoculum	56
Table 5.8: Plan for the gradually increase of hydraulic retention time during fermentative hydrogen production	56
Table 5.9: Parameters for the small scale pilot plant field tests	58
Table 5.10: Measured and unmeasured variables for data reconciliation problem of the membrane measurements	61
Table 5.11: Deviations given for the utilized measuring equipment	63
Table 5.12: Input parameters for the ACM models	72
Table 5.13: Variables and assumptions for comparison of counter-current and co-current operational mode using the Aspen Plus [®] sensitivity analysis tool.....	74
Table 5.14: Feed gas conditions defined for the Aspen Plus [®] two-stage simulation: source: [Lassmann et al., 2015].....	77
Table 5.15: Assumptions for the multi-stage Aspen Plus [®] simulation; source: [Lassmann et al., 2015]	77
Table 5.16: Sensitivity analysis of membrane area variation for 2-stage processes.....	81
Table 5.17: Sensitivity analysis of membrane area variation for 3-stage processes.....	81
Table 5.18: Parameters for the validation of the ACM simulation model by comparison with measurements	82
Table 5.19: Parameters varied for validation of the ACM simulation by comparison with Makaruk&Harasek model	83
Table 5.20: Parameters varied and assumptions taken for validation of the ACM simulation by comparison with CFD simulation.....	85
Table 6.1: Pure gas measurement results for membrane module M-1.....	88
Table 6.2: Comparison of membrane modules M-1, M-2, M-3, and M-4 regarding ideal selectivity and permeance	91
Table 6.3: Arrhenius parameters and estimation of purification parameters at elevated temperature	94
Table 6.4: Comparison of permeances and selectivities of gas mixtures and pure gases.....	99
Table 6.5: Comparison of theoretical and measured H ₂ composition in permeate for a 66-34-0 feed gas mixture	100
Table 6.6: Comparison of theoretical and measured H ₂ composition in permeate for a 30-30-40 feed gas mixture	101
Table 6.7: Comparison of pure gas permeances before and after the field tests for membrane module M-1.....	105
Table 6.8: Comparison of ideal selectivities before and after the field tests for membrane module M-1.....	105

<i>Table 6.9: Measurement data before DR</i>	106
<i>Table 6.10: Measurement data after DR</i>	107
<i>Table 6.11: Deviations of the validation results for comparison with the Makaruk&Harasek model</i>	114
<i>Table 6.12: Comparison of the investigated setups with a fixed H₂-recovery</i>	119
<i>Table 6.13: Comparison of the investigated setups 1 and 2 at an operational temperature of 80°C and with fixed H₂-recovery</i>	120
<i>Table 6.14: Results of the investigated setup 4 with a fixed H₂-recovery</i>	120
<i>Table 6.15: Combustion parameters of the off-gas stream in various setups</i>	121
<i>Table 6.16: Output of the combustion heat of the off-gas stream in different setups as well as decoupled electric and thermic power</i>	122
<i>Table B.1: Pure gas measurement results for membrane module M-2</i>	XXIV
<i>Table B.2: Pure gas measurement results for membrane module M-4</i>	XXV
<i>Table B.3: Comparison of pure gas permeances before and after the field tests for membrane module M-2</i>	XXVI
<i>Table B.4: Comparison of ideal selectivities before and after the field tests for membrane module M-2</i>	XXVI

LIST OF SYMBOLS

Latin letters:

Letter	Description	Unit
A_{Cell}	Membrane area	m^2
b	Langmuir affinity constant	bar^{-1}
c'_H	Langmuir capacity constant	$m^3_{(STP)} \cdot m^{-3} \cdot bar^{-1}$
c_i	Concentration of component i	$mol \cdot m^{-3}$
c_M	Concentration of gas in polymer	$m^3_{(STP)} \cdot m^{-3}$
ΔH_K	Partial molar enthalpy of sorption	$J \cdot mol^{-1}$
$d_{i,Fiber}$	Inner diameter of the fiber	m
d_i	Inner diameter of the fiber	m
D_i	Diffusion coefficient for component i	$cm^2 \cdot s^{-1}$
D_j	Diffusion coefficient for component j	$cm^2 \cdot s^{-1}$
dx	Differential length through membrane wall	m
E_D	Activation energy of diffusion	$J \cdot mol^{-1}$
E_p	Activation energy of permeation	$J \cdot mol^{-1}$
F	Feed flow	$kmol \cdot h^{-1}$
J_i	Transmembrane mass flow of component i	$kg \cdot s^{-1}$
$J_{i,k}^{A,mol}$	Area specific transmembrane molar flow of component i in Cell k	$kmol \cdot h^{-1} \cdot m^{-2}$
K_i	Gas phase sorption coefficient for component i	$cm^3_{(STP)} \cdot cm^{-3} \cdot cmHg^{-2}$
K_j	Gas phase sorption coefficient for component j	$cm^3_{(STP)} \cdot cm^{-3} \cdot cmHg^{-2}$
$P_{i,0}$	Pre-exponential factor in Arrhenius equation	$m^3 \cdot m \cdot m^{-2} \cdot s^{-1} \cdot Pa^{-1}$
P_i	Permeability of component i	$m^3 \cdot m \cdot m^{-2} \cdot s^{-1} \cdot Pa^{-1}$
dp_k	Pressure drop in fiber	Pa
k_D	Henry's constant	$m^3_{(STP)} \cdot m^{-3} \cdot bar^{-1}$
l	Thickness of membrane's selective layer	m
l_{Fiber}	Fiber length	m

Letter	Description	Unit
N	Number of fibers	-
N_{Fiber}	Number of fibers	-
N_{Cells}	Number of Cells in Simulation	-
$\dot{n}_{Feed,0}$	Feed molar flow in Cell 0 (inlet)	kmol.h ⁻¹
\dot{n}_{Feed}	Feed molar flow	mol.s ⁻¹
$\dot{n}_{Permeate,0}$	Permeate molar flow in Cell 0 (outlet)	kmol.h ⁻¹
$\dot{n}_{Permeate,N_{Cells}}$	Permeate molar flow in Cell 0 (inlet)	kmol.h ⁻¹
$\dot{n}_{Permeate,N_{Cells}+1}$	Permeate molar flow in Cell $N_{Cells}+1$ (inlet)	kmol.h ⁻¹
$\dot{n}_{Permeate,k}$	Permeate molar flow in Cell k	kmol.h ⁻¹
$\dot{n}_{Permeate,k+1}$	Permeate molar flow in Cell $k+1$	kmol.h ⁻¹
$\dot{n}_{Permeate,k-1}$	Permeate molar flow in Cell 0 (inlet)	kmol.h ⁻¹
$\dot{n}_{Permeate}$	Permeate molar flow	mol.s ⁻¹
$\dot{n}_{Retentate,N_{Cells}}$	Retentate molar flow in Cell N_{Cells} (outlet)	kmol.h ⁻¹
$\dot{n}_{Retentate,k}$	Retentate molar flow in Cell k	kmol.h ⁻¹
$\dot{n}_{Retentate,k-1}$	Retentate molar flow in Cell $k-1$	kmol.h ⁻¹
P	Permeate flow	kmol.h ⁻¹
p_{Fiber}	Absolute pressure in the fiber	Pa
$p_{i,0}$	Feed side partial pressure of component i	Pa
$p_{i,Permeate,k}$	Permeate partial pressure of comp. i in Cell k	bar
$p_{i,Permeate,k-1}$	Permeate partial pressure of comp. i in Cell $k-1$	bar
$p_{i,Retentate,k}$	Retentate partial pressure of comp. i in Cell k	bar
$p_{i,Retentate,k-1}$	Retentate partial pressure of comp. i in Cell $k-1$	bar
$p_{i,l}$	Permeate side partial pressure of component i	Pa
R	Retentate flow	kmol.h ⁻¹
R	Gas constant	J.mol ⁻¹ .K ⁻¹
T	Operating temperature	K
\dot{v}_{Fiber}	Volume flow in the fiber	m ³ .s ⁻¹
$x_{F,i}$	Mole fraction of component i in feed	mol.mol ⁻¹

Letter	Description	Unit
$x_{F,j}$	Mole fraction of component j in feed	mol.mol^{-1}
$x_{F,k}$	Mole fraction of component k in feed	mol.mol^{-1}
$x_{P,h}$	Mole fraction of component h in permeate	mol.mol^{-1}
$x_{P,i}$	Mole fraction of component i in permeate	mol.mol^{-1}
$x_{R,i}$	Mole fraction of component i in retentate	mol.mol^{-1}
$y_{\text{Permeate},k}$	Permeate molar fraction in Cell k	mol.mol^{-1}
$y_{\text{Permeate},k-1}$	Permeate molar fraction in Cell $k-1$	mol.mol^{-1}
$y_{\text{Retentate},k}$	Retentate molar fraction in Cell k	mol.mol^{-1}
$y_{\text{Retentate},k+1}$	Retentate molar fraction in Cell $k+1$	mol.mol^{-1}

Greek letters:

Letter	Description	Unit
$\Pi_{i,k}$	Permeance of component i in Cell k	$\text{m}^3_{(\text{STP})}.\text{m}^{-2}.\text{s}^{-1}.\text{Pa}^{-1}$
Π_i	Permeance of component i	$\text{m}^3_{(\text{STP})}.\text{m}^{-2}.\text{s}^{-1}.\text{Pa}^{-1}$
$\alpha_{i,h}$	Ideal membrane selectivity for better permeating component i and less permeating component h	-
$\alpha_{i,j}$	Ideal membrane selectivity for better permeating component i and less permeating component j	-
$\alpha_{j,h}$	Ideal membrane selectivity for better permeating component j and less permeating component h	-
θ	Stage cut	-
μ	Dynamic viscosity	$\text{kg.m}^{-1}.\text{s}^{-1}$

Data reconciliation – letters:

Letter	Description
A_y	Jacobian matrix of measured values
A_z	Jacobian matrix of unmeasured values
b	First order Taylor series

$f(\hat{\mathbf{y}}, \hat{\mathbf{z}})$	Nonlinear constraints
$J(\hat{\mathbf{y}}, \hat{\mathbf{z}})$	Objective function
K	Tolerance criterion
n	Number of iterations
Q_1	Partition 1 of Q-R factorization matrix; dimension (M x N)
Q_2	Partition 2 of Q-R factorization matrix; dimension (M x M-N)
R_1	Partition 1 of upper triangular matrix; dimension (N x N)
R_2	Partition 2 of upper triangular matrix; dimension (N x M-N)
V	Covariance matrix of measurements (M x M)
y	Vector of measured variables; dimension (M x 1)
\hat{y}	Vector of estimates to measured values; dimension (M x 1)
z	Vector of unmeasured variables; dimension (N x 1)
\hat{z}	Vector of estimates to unmeasured values; dimension (N x 1)

Data reconciliation – indices:

Letter	Description
C	Total number of equality constraints
i	Iteration number during linearization
M	Total number of measured variables
N	Total number of unmeasured variables
r	Rank of A_z

ABBREVIATIONS

Abbr.	Description
6FDA	4,4'-(Hexafluoroisopropylidene)-diphthalic anhydride
APR	Aqueous phase reforming
ATP	Adenosine triphosphate
ATR	Autothermal reforming
$C_6H_{12}O_6$	Glucose
CFD	Computational fluid dynamics
CH_3COCOO^-	Pyruvate
CH_4	Methane
CHP	Combined heat and power unit
CO	Carbon monoxide
CO_2	Carbon dioxide
COD	Chemical oxygen demand
COFs	Covalent organic frameworks
DEA	Diethanolamine
DETA	Diethylenetriamine
DI	Direct injection
DIPA	Diisopropylamine
DME	Dimethyl ether
FC	Fuel cell
FCV	Fuel cell vehicle
H_2	Hydrogen
H_2ICE	Hydrogen internal combustion engine
H_2S	Hydrogen sulfide
HRT	Hydraulic retention time
ICE	Internal combustion engine
LFL	Lower flammability limit

Abbr.	Description
LOHC	Liquid organic hydrogen carriers
MDEA	Methyl diethanolamine
MEA	Monoethanolamine
MEC	Microbial aided electrolysis cell
MMM	Mixed matrix membrane
MMOMs	Micro porous metal coordination materials
MOFs	Metal-organic frameworks
NADH	Nicotinamide adenine dinucleotide
NH ₃	Ammonia
Ni	Nickel
NMP	N-methyl-2-pyrrolidone
NO _x	Nitrogen oxides
O ₂	Oxygen
OLR	Organic loading rate
PBI	Polybenzimidazole
Pd	Palladium
PDMS	Poly dimethyl siloxane
PEBAX	Poly(amide-b-ethylene oxide)
PEC	Photo electrolysis
PEM	Proton exchange membrane
PFI	Port fuel injection
PFL	Pyruvate formate lyase
PFOR	Pyruvate ferredoxin oxidoreductase
PI	Polyimide
POX	Partial oxidation
PP	Polypropylene
PR	Plasma reforming
PrOx	Preferential oxidation

Abbr.	Description
PSA	Pressure swing adsorption
Pt	Platinum
PtG	Power to gas
RC	Relative correction
Rh	Rhodium
SMR	Steam methane reforming
SO ₂	Sulfur dioxide
SOEC	Solid oxide electrolysis cells
TEA	Terminal electron acceptor
TSA	Temperature swing adsorption
UFL	Upper flammability limit
VPSA	Vacuum pressure swing adsorption
WGS	Water-gas-shift
WWTP	Waste water treatment plant

1. Motivation

Rising sea level, warming oceans, shrinking ice sheets, glacial retreat, and global temperature rise are just a few signs that cannot be ignored and which indicate that climate change is happening rather fast than slow. Therefore, climate change can be seen as one of the greatest challenges of our generation which needs to be tackled as soon as possible. In this context, reducing greenhouse gases (GHGs) is seen to be a potential solution, as increasing GHG emissions are a major contributor to climate change [Mondal et al., 2012]. Among all GHGs, CO₂ has the most harmful impact accounting for approximately 64% of the greenhouse effect [IPCC, 2007]. Hence, carbon dioxide is the targeted component which needs to be reduced towards a climate friendly future. With coal-fired power plants as the main contributor, fossil fuel power plants account for nearly 40% of total CO₂ emission [Mondal et al., 2012]. As short and mid-term solution, CO₂ capture and separation is a much discussed and investigated route for CO₂ emission reduction. But this route is not applicable for the transport sector, which is another big carbon dioxide contributor that needs to be targeted in order to reduce global emissions. According to Balat and Kirtay [2010] one-fifth of global carbon dioxide emissions are created by the transport sector. It is therefore more reasonable to get down to the root of the problem by addressing the energy sources – fossil fuels. Today fossil fuels primarily cover the global energy demand, with crude oil, natural gas and coal accounting for nearly 85% [Balat and Kirtay, 2010, Mondal et al., 2012]. Taking a closer look on the transport sector shows that almost 100% of the energy used is generated from fossil sources [Westermann et al., 2007] which accounts for approximately 60% of global oil consumption [Balat and Kirtay, 2010]. Obviously a shift from fossil based to renewable energy sources would have an immediate impact on the environment. Unfortunately, there are still many obstacles to overcome before this shift will be possible. One of these obstacles is referred to world's growing energy demand, which accounted for 500 EJ in 2011 and is predicted to reach 1000 EJ in 2050 [Dincer and Acar, 2015, Suleman et al., 2015]. Even if the increase in energy demand is only a fraction of the predicted growth rate, in combination with the progressing scarcity of resources it will make a transition towards a renewable energy system inevitable [Schiebahn et al., 2015]. Duić [2015] states that as long as the user has the benefit from using fossil fuels, while the resulting damage is global, the effect of climate change won't will not be a strong enough reason to push the development of alternatives. Contrary to that, Bulatov and Klemeš [2011] see global warming and greenhouse gas emissions as growing issues not only on technological, but rather on societal and political levels. Several countries in the world have recently addressed important political routes to counteract the predicted trend by setting actual actions away from a fossil fuel based economy and towards renewable energy carriers. For

example, the United Arab Emirates have decided to turn towards solar energy, building an enormous solar power center. In the United States California and New York are calling for an increase of the renewable energy amount in the energy mix, with a targeted share of 60% by 2030. Regarding the transportation sector, several alternatives to fossil fuel based engines have been developed and tested over the past decades with electric and hydrogen powered engines being the most promising ones. Unfortunately none of these two technologies was able to assert itself, still causing a broad discussion about which will prevail and lead towards a carbon-neutral economy. Numerous researchers and engineers argue that a hydrogen energy system would be the best option to replace the existing fossil fuel system [Saxena et al., 2009, Uddin and Daud, 2014]. This goes in hand with the statement of Ehret and Bonhoff [2015] who see hydrogen as the energy carrier of the future. Hydrogen is frequently associated with its positive effect on global warming and greenhouse gas emissions [Bulatov and Klemeš, 2011] and hydrogen fuel cells are often considered as a key technology for sustainable energy supply [Balat and Kirtay, 2010]. In a recent study on hydrogen as the future transportation fuel by Sharma and Ghoshal [2015] it is seen to hold the promise to be the fuel of the future, provided that the major technological barriers will be resolved, which are mostly cost-based. But, Sharma and Ghoshal [2015] point out that the most important barrier relates to the provision of a sustainable production route. Therefore, to enable the transition towards a hydrogen-based economy the provision of high-quality hydrogen gas from renewable sources needs to be an inevitable requirement. Several renewable hydrogen production routes are already state of the art, such as water electrolysis driven by wind energy or photovoltaics. Another possibility is the utilization of biomass as feedstock for hydrogen production. Biomass gasification seems to be a promising pathway towards a sustainable hydrogen economy. Besides this thermo-chemical conversion of biomass, another step towards a sustainable energy supply could be the hydrogen production based on biotechnological pathways, such as dark fermentation. An advantage of dark fermentation is that biomass residues, second generation biomasses, agricultural and agro-industrial solid wastes as well as wastewater can be utilized to produce a hydrogen-rich gas. According to Urbaniec and Bakker [2015], dark fermentation is considered as one of the most environmentally friendly hydrogen production routes. One issue concerning dark fermentation is the subsequent purification of the fermentation gas. Well established upgrading methods, such as amine absorption or pressure swing absorption may be suitable from a technological point of view, but might not be the most energy efficient method because gas capacity, composition and conditions differ considerably from industrial processes. In this regard membrane technology, more precisely gas permeation, is a very interesting option for the upgrading of fermentative produced hydrogen. Hence, it is important to investigate this concept regarding its applicability and limitations.

2. Introduction

As mentioned before, hydrogen is seen as a promising alternative to fossil energy sources. But it is important to mention that hydrogen is only a secondary form of energy and it needs to be generated from primary energy sources [Kothari et al., 2008]. This can be seen as a disadvantage, but it is offset by numerous advantages. Dincer and Acar [2015] list the advantages of hydrogen as following: i.) high energy conversion efficiencies, ii.) no emissions when produced from water, iii.) abundance, iv.) different storage possibilities, v.) long distance transportation, and vi.) simple conversion to other energy forms. Even though these characteristics sound very promising, it is important to take a closer look at the overall concept of hydrogen. Thereto, an overview about hydrogen production, purification and storage methods is provided in this chapter. Finally, the utilization of hydrogen is discussed followed by product gas standards regarding fuel quality.

2.1 Production, purification and storage of hydrogen

The subsequent chapters provide information about the state of the art in hydrogen production, the present hydrogen market and information about hydrogen produced on a renewable basis. Furthermore, purification and storage methods are described, followed by a short description of the power-to-gas concept.

2.1.1. State of the art in hydrogen production

There are many different processes to produce hydrogen and they can be classified in many different forms. One possibility is to classify the processes according to the method, which classifies them into three major categories: i.) thermochemical, ii.) electrochemical, and iii.) biological methods [Chaubey et al., 2013]. In the subsequent classification of hydrogen production processes a different approach is chosen, which is based on feedstock and inspired by the form used of Holladay et al. [2009]. In Figure 2.1 this form of process classification is shown, with hydrocarbon fuels, biomass and water as the three main feedstock sources. The most common methods can be classified in two main technological routes, the fuel processing technologies and the non-reforming hydrogen production technologies. Typical fuel processing technologies are hydrocarbon reforming, coal gasification, pyrolysis, plasma reforming (PR), aqueous phase reforming (APR), and ammonia reforming. Non-reforming hydrogen production can be maintained either by the water-based methods such as electrolysis, thermolysis, and photo electrolysis (PEC), or by the biomass-based methods such as biomass gasification, direct photolysis, dark fermentation, photo-fermentative processes, and microbial electrolysis cells. One process that cannot be put in one of the following categories is the stem-iron process, as coal, oil and biomass are

consumed. The steam-iron process is considered as one of the oldest methods for hydrogen production [Chaubey et al., 2013].

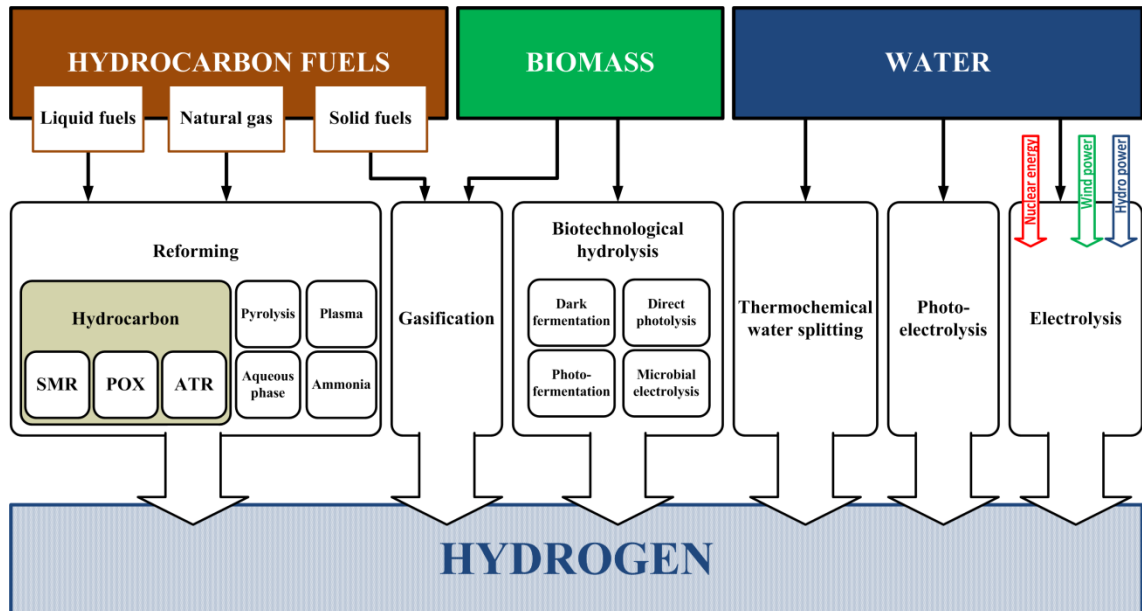


Figure 2.1: Technological routes in hydrogen production based on feedstock

It is a thermo-chemical process that comprises two steps: At first, a reduction step where the feedstock is gasified to a hydrogen-rich reducing gas, which reacts with iron oxides (hematite, magnetite, wuestite) to a reduced form of iron oxide and/or metallic iron. At second, an oxidation step where the reduced iron oxide reacts with steam to generate hydrogen. The resulting hydrogen purity is larger 99.9 vol% [Chaubey et al., 2013]. Subsequently the common hydrogen production methods based on feedstock are briefly discussed.

Feedstock: Hydrocarbon fuels

Hydrocarbon reforming

Today, the reforming of methane is the most common commercially used hydrogen production method [Alves et al., 2013]. There are three different techniques that have to be distinguished: i.) steam methane reforming (SMR), ii.) partial oxidation (POX), and iii.) autothermal reforming (ATR).

In industry, *steam methane reforming* is the preferred application for hydrogen production, as it produces a reformat containing hydrogen, methane, carbon dioxide and carbon monoxide with a high H_2/CO ratio. Sharma and Ghoshal [2015] state respective H_2 , CH_4 , CO_2 and CO contents in the range of 70-75%, 2-6%, 6-14%, and 7-

10%, on a dry mass basis. The reforming takes place at temperatures around 300 to 500 °C. As the process is highly endothermic an external heat source has to be applied. Furthermore, it causes higher emissions compared with the other two reforming techniques, which is a big disadvantage from an environmental point of view [Kothari et al., 2008]. Typical catalysts in steam reforming are nickel (Ni), platinum (Pt) or rhodium (Rh) based, with nickel catalysts used almost universally in industry [Alves et al., 2013]. Steam reforming achieves thermal efficiencies up to 85%, based on the higher heating values.

As the name *partial oxidation* indicates, the hydrocarbons are partially oxidized with oxygen which yields in a mixture of hydrogen and carbon monoxide. Contrary to SMR the required temperatures are between 1300-1500 °C to ensure a complete conversion [Kalamaras and Efstathiou, 2013]. The process is moderately exothermic, which has a positive effect on the energy costs [Alves et al., 2013]. No catalysts are required, but can be applied to lower the operational temperature to 700 - 900 °C. The benefit of POX is its tolerance against sulfur, which is often a contaminant in hydrocarbon fuels. Contrary, the biggest disadvantage of POX is the emission of carbon monoxide [Kothari et al., 2008]. POX achieves thermal efficiencies up to 60-75%, based in the higher heating values.

In *autothermal reforming*, the benefits from steam reforming and POX are combined, as the required heat is provided by the partial oxidation and the hydrogen production is increased due to the steam reforming. With thermal efficiencies for ATR of 60-75% based on the higher heating value, this technique is in the range of POX. Furthermore, ATR is seen to be favorable in the gas-liquids industry as the product gas composition is more suitable for the Fischer-Tropsch synthesis. It is also simpler and less expensive than SMR [Kalamaras and Efstathiou, 2013].

Because the before mentioned reforming techniques produce a certain amount of carbon monoxide, a subsequent water-gas-shift (WGS) reaction can be used to reduce CO and increase the hydrogen content in the final product. If a further reduction of carbon monoxide is needed, preferential oxidation (PrOx) or carbon monoxide selective methanation reactions are typically applied [Kalamaras and Efstathiou, 2013].

Coal gasification

The mechanism of coal gasification is similar to partial oxidation. Coal gasification can either be carried out via the synthane process or the CO₂ acceptor process. In the second that method, coal reacts with steam to a product mainly containing H₂, CO₂ and CO. CO₂ needs to be removed via washing, which leads to a final hydrogen content up to 97 – 98 % [Kothari et al., 2008]. During the CO₂ acceptor process, lime is introduced during the steam with coal reaction. As a result, carbon

dioxide can be removed as calcium carbonate. From an environmental point of view, coal gasification is not suitable for industrial hydrogen production due to the large amount of carbon dioxide emitted.

Pyrolysis

In pyrolysis technology the hydrocarbon is split into hydrogen and carbon with neither oxygen nor water present. This saves the need for subsequent elimination of carbon oxides, as CO cannot be generated under the absence of air or water. As a result fewer emissions will occur. Additionally to the emission reduction, fuel flexibility and a clean carbon by-product are in pyrolysis technology's favor. The temperature range for pyrolysis can be divided into three sub-groups: i.) low temperature pyrolysis takes place at up to 500 °C, ii.) medium temperature pyrolysis occurs between 500 and 800 °C, and iii.) above 800 °C it is defined as high temperature [Kalamaras and Efstathiou, 2013]. Kalamaras and Efstathiou [2013] state, that pyrolysis is a well-developed hydrogen production method and could already be used in a commercial scale.

Plasma reforming

This technology applies the same basic reforming reactions as all other reforming technologies. The main difference is that in this case plasma is used to provide the energy and free radicals needed for the reforming [Kalamaras and Efstathiou, 2013]. Due to the thermal plasma activity natural gas dissociates to hydrogen and carbon black [Dincer and Acar, 2015]. Among the advantages of PR, it can be operated at low temperatures and it is quite tolerant with sulfur. Disadvantages are the electrical requirements and a higher erosion of the electrode. There are two different types of plasma reforming, i.) thermal PR, which uses a high electric discharge, and ii.) non-thermal PR, which requires only a mere fraction of power. Possible applications of PR could be the on-board generation of hydrogen for fuel cells or as a stationary source for hydrogen refueling [Kalamaras and Efstathiou, 2013].

Aqueous phase reforming

In aqueous phase reforming the reforming process and the WGS reaction take place at the same time. In other words, oxygenated hydrocarbons or hydrocarbons are used to generate hydrogen. This reforming technology is still under development, with a certain focus on the utilized catalysts. Its main advantages are the low operating temperature in the range of 220 – 270 °C, a hydrogen yield increase, the elimination of CO, and that there is no need in vaporization of the water in the feedstock [Kalamaras and Efstathiou, 2013].

Ammonia reforming

This reforming method has been especially developed for the hydrogen utilization via fuel cell technology. When applying solid oxide fuel cells, the ammonia can be fed directly to produce hydrogen. For ammonia reforming typically used catalysts are iron oxide, molybdenum, ruthenium and nickel.

Feedstock: Water

Electrolysis

Kalamaras and Efstathiou [2013] mention electrolysis as a promising method for the production of hydrogen in the near future. During electrolysis the chemical bonds in water molecules are broken into hydrogen and oxygen by applying two electrodes, a cathode and an anode, which are connected to an electrical current. The system efficiencies of commercial electrolyzers are in the range of 56-73%. According to Sharma and Ghoshal [2015] electrolysis is currently performed from a few kW up to 2000 kW per electrolyzer. In this hydrogen production method three different electrolysis technologies need to be distinguished: i.) alkaline electrolyzers, ii.) proton exchange membrane (PEM) electrolyzers, and iii.) solid oxid electrolysis cells (SOEC). Alkaline electrolyzers are the most commonly used technology, utilizing an aqueous alkaline electrolyte, in which the electrodes and a microporous separator are located. Typically used cathode material is nickel with a catalytic coating, for example platinum. The anode is commonly made of nickel or copper metals with a metal oxide coating, such as ruthenium or manganese. Hydrogen is formed on the cathode side and stays in the alkaline solution. To separate hydrogen from water a gas liquid separation needs to be applied subsequently to the electrolyzer. In PEM this separation unit is redundant, as the applied membrane causes a gas separation effect which holds the generated O₂ on the anode side. Common electrodes used in PEM electrolyzers are iridium, rhodium, and Pt black based. The principal of SOEC is similar to the alkaline technology, with the difference that some part of the water is split with thermal energy and a solid electrolyte is used.

Thermochemical water splitting

Water can be decomposed to hydrogen and oxygen by using just heat. Thereto, a temperature of 2500°C needs to be applied. This process is known as thermochemical water splitting, or thermolysis. For thermolysis one of the biggest challenges comes with the operational conditions, as high-temperature materials need to be used for effective H₂ and O₂ separation process [Kalamaras and Efstathiou, 2013]. Overall efficiencies of thermolysis are close to 50%, which is a fairly low value compared to the before mentioned water splitting methods.

Water splitting with nuclear energy

Nuclear energy can either be used directly for the electrolysis of water or as thermal energy in form of waste high temperature steam heat for thermochemical water splitting¹. Both applications are attractive from a carbon-limiting perspective, but are not reasonable from an environmental point of view.

Water splitting with renewable energy

The energy from renewable sources, such as wind and water, can also be used to provide the required electricity for water electrolysis. The utilization of wind-turbines in connection with an electrolysis process is mentioned to have great potential, as it is renewable and pollution-free [Kothari et al., 2008]. Electricity from hydropower is another possibility to supply the electrolysis process with renewable energy.

Photoelectrolysis

In PEC sunlight is used to split water directly into hydrogen and oxygen. Because semiconductor materials are used, its principle can be compared to the procedure occurring in photovoltaics, except that water is decomposed to hydrogen and oxygen instead of electricity production. Unfortunately, the conversion efficiency from solar energy to hydrogen of today's photoelectrodes used in PEC is just 16% [Riis et al., 2006]. As photoelectrolysis uses solar energy, it has the big advantage to be a zero emissions process [Sharma and Ghoshal, 2015]. Kalamaras and Efstathiou [2013] consider photoelectrolysis as an environmental friendly application, but also mention that it has a low applicability for large industrial use.

Feedstock: Biomass

Biomass is often considered to be the most likely renewable organic substitute to petroleum [Holladay et al., 2009]. It is a biological material that can be extracted from many sources, for example existing or recently existing organisms, plants like agricultural residues or wastes, different crops, aquatic plants, as well as agro industrial wastes [Uddin and Daud, 2014, Al-Shorgani et al., 2013]. According to Balat and Kirtay [2010] using biomass for hydrogen production has the advantages of being independent from oil imports, the feedstock can be obtained within the country, and improvement of the CO₂ balance.

¹ U.S. Department of Energy, Nuclear Hydrogen R&D Plan, March 2004; accessed online: http://energy.gov/sites/prod/files/2015/01/f19/fcto_nuclear_h2_r%26d_plan.pdf

Biomass gasification

Gasification is a well-established technology that is used to convert fossil or organic fuel based carbonic material into methane, hydrogen, carbon dioxide and carbon monoxide. During gasification process, the conversion is achieved by pyrolysis, respectively partial oxidation, of the components reduction and combustion reactions. There to either air, or pure oxygen, subcritical steam, or a mixture of these is used as reaction agent [Parthasarathy and Narayanan, 2014]. The resulting product gas is also known as syngas or producer gas with a hydrogen content higher 40 vol% [Wilk and Hofbauer, 2016]. Generally, the gasification is carried out at high temperature to obtain an optimal gas production [Balat and Kirtay, 2010, Pfeifer et al., 2009]. There are several types of reactors used for gasification, such as fixed bed, or fluidized bed, just to name a few. Depending on the task, catalysts may be required. To achieve a higher hydrogen quality the syngas can be fed to a WGS process following gasification. One of the challenges with biomass gasification is the significant amount of tar occurring in the product gas. The efficiencies of biomass gasification are in the range of 35-50%, based on the lower heating value. The relatively low thermal efficiency of this technology is caused by the relatively high moisture content in the feedstock which needs to be vaporized [Kalamaras and Efstathiou, 2013]. Typical biomass gasification reactors are built on a large scale, which results in a high amount of feedstock needed. The commercialization of hydrogen from biomass gasification is still limited by the logistic costs for biomass provision and the removal of tar to acceptable levels [Kalamaras and Efstathiou, 2013].

Direct photolysis or photosynthesis

During photosynthesis solar energy is used to generate carbohydrates and oxygen from carbon dioxide and water. The process can be either oxygenic or anoxygenic. Oxygenic organisms, such as green algae, use solar energy to decompose water to hydrogen and oxygen ions [Allakhverdiev et al., 2010]. This decomposition process by algae is also known as direct photolysis [Show and Lee, 2013]. The main drawbacks of this technology are the large surface area that is needed for solar collectors, the requirement in a subsequent gas separation unit, and the maximum theoretical efficiency of just 1%. As water and algae are the main process components, this process could also be listed in the section with feedstock water.

Photo-fermentative process

During the photo-fermentative process organic material is fermentative converted to hydrogen under the presence of light. This can be achieved by bacteria with nitrogenase functionality. Light is used to split water into oxygen, electrons and hydrogen ions, which are then converted by the hydrogenase enzymes into hydrogen

gas [Zhang et al., 2015a]. A major challenge for this process is the large areas that photobioreactors demand [Westermann et al., 2007]. The efficiency of this process is currently in the range of 1.9%, but the theoretical limit is 68% according to the U.S.DOE². At the current state of the art, photo-fermentative hydrogen has been considered economically unrealistic [Westermann et al., 2007].

Microbial electrolysis cell

In microbial electrolysis cells hydrogen is produced via the bio-catalyzed electrolysis from biodegradable material. Thereto, a microbial aided electrolysis cell (MEC) is used, which only requires a small amount of electricity.

Dark fermentation

Anaerobic bacteria are used to convert a carbohydrate rich substrate to a product gas mainly containing hydrogen and carbon dioxide. The theoretical maximum hydrogen production for the standard fermentative pathway is 4 moles of hydrogen per mole of glucose. During anaerobic fermentation acetic, butyric and other organic acids are formed, which can inhibit the hydrogen formation. When compared with photosynthesis, fermentation is a more efficient and stable hydrogen production process [Azwar et al., 2014]. Detailed information about the hydrogen production via dark fermentation will be presented in section 4.1 of this thesis.

Combined processes

The production of hydrogen via combined photo- and dark fermentation has been investigated in some studies [Foglia et al., 2010, Foglia et al., 2011, de Vrije and Claassen, 2003, Claassen et al., 2010]. Foglia et al. [2010] describes the process as a thermophilic fermentation step which is followed by a photo-heterotrophic fermentation step that utilizes the organic acids to further produce hydrogen.

Industrial processes:

From all before mentioned processes for hydrogen production Chaubey et al. [2013] considers four as industrial:

- i.) Steam methane reforming
- ii.) Partial oxidation
- iii.) Auto-thermal reformation
- iv.) Steam-iron process.

² U.S. Department of Energy, Hydrogen, Fuel Cells and Infrastructure Technologies Program, 2007, Multi-Year Research, Development and Demonstration Plan.

Furthermore, natural gas is still the industrially most favored feedstock due to its abundant availability and advantageous price, even though there are already numerous alternative feedstocks industrially used [Chaubey et al., 2013].

2.1.2. Hydrogen market

From 2008 to 2014 the annual production of hydrogen rose from approximately 50 to 57 million metric tons. Currently, up to 96% of this commercially produced hydrogen is based on fossil fuels [Uddin and Daud, 2014, Zhang et al., 2015], because reforming of gas and heavy oil, gasification of coal, heavy oil and petroleum coke are the dominating industrial production routes [Sharma and Ghoshal, 2015]. The remaining 4% are produced by electrolysis, which is indirectly fossil fuel dependent as the utilized electricity is partly generated through fossil fuels [Kothari et al., 2008, Kalamaras and Efstathiou, 2013]. With regard to the production routes that use fossil fuels directly, the biggest share of the global hydrogen production is contributed by steam reforming of natural gas accounting for little less than 50% [Kalamaras and Efstathiou, 2013]. About 30% are generated by reforming of heavy oils and naphtha which is provided by refinery or chemical industrial off-gases [Dincer and Acar, 2015]. The third biggest share is attributed to coal gasification which accounts for 18% of global hydrogen production [Muradov and Veziroglu, 2005, Balat and Kirtay, 2010]. In Figure 2.2 the left pie chart pictures the respective contributions of different feedstocks on global hydrogen production in 2008. Not displayed in this chart is the < 1% share of hydrogen generated from biomass [Balat and Kirtay, 2010]. The pie chart on the right side displays the worldwide application areas of hydrogen with their respective shares. As the presented graph refers to the year 2008 it should be seen as an indicator of allocation. It can be seen that largest consumption of hydrogen occurs in petroleum refining [Kothari et al., 2008]. According to Balat and Kirtay [2010] the production of ammonia consumed approximately 51% of all globally produced hydrogen. In oil refining 35% were utilized and methanol synthesis required 8% of the total hydrogen production. The remaining 6% account for miscellaneous smaller-volume uses, e.g. energy generation [Balat and Kirtay, 2010]. Furthermore, Balat and Kirtay [2010] state that the global market for hydrogen is already greater than U.S.\$ 40 billion per year and that the present utilization of hydrogen is equivalent to 3% of the global energy consumption. Not considered in the before displayed hydrogen production routes are the processes where hydrogen is only a by-product. For example, in the iron and steel industry hydrogen-containing gases are generated during coke production, in the blast furnace and the basic oxygen furnace. Globally, these gas streams account for

approximately 8 EJ/year and in 2012 around 68% were reused in iron and steel production processes to displace other fossil fuels for heating purposes³.

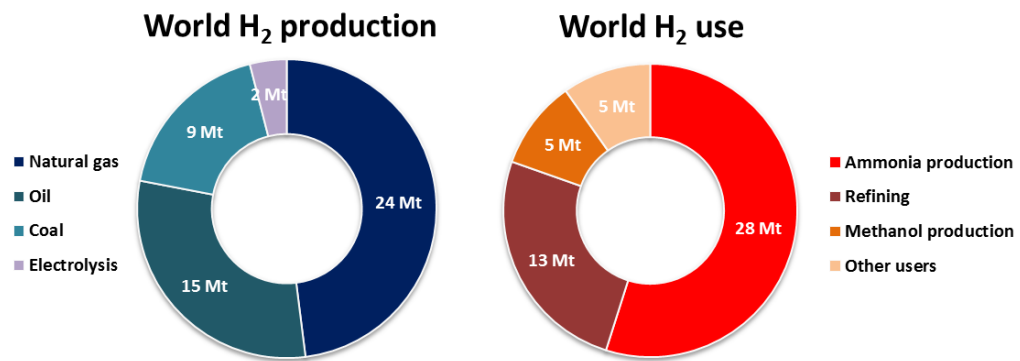


Figure 2.2: Global hydrogen production and utilization in 2008, based on a total hydrogen production of approximately 50 Mt per year⁴

Breaking the global hydrogen production down into geographical regions shows that the United States accounted for 30% of it, followed by South Korea and Japan with respective shares of 10% each and Kuwait with 5%. DoE's Hydrogen Energy Data Book⁵ further reveals that the production of hydrogen in 2014 in the United States and Canada accounted for 14,588 tons per day, of which 98.3% were compressed gas and the remaining 1.7% cryogenic liquid. The main share, around 90%, of the produced hydrogen came from the United States. Compared to that, European production quantity is rather small with a total of 2.366 t/d. The biggest contributor in Europe is Germany accounting for 4.7% the globally produced hydrogen, which is 10-times more than Austria's contribution.

A crucial factor to establish hydrogen as a competitive energy carrier is its production cost and, associated therewith, the achievable hydrogen price. Subsequently, estimations for production cost of the different production routes will give an insight into the current hydrogen economy and its potential. Today's cheapest hydrogen can be obtained from coal and natural gas with estimated prices in the range of 0.36 - 1.83 U.S.\$/kg and 2.48 - 3.17 U.S.\$/kg, respectively [Bartels et al., 2010]. From an energy related point of view, hydrogen production costs from natural gas using SMR

³ Online source: <https://www.iea.org>, Free publications: *TechnologyRoadmapHydrogenandFuelCells.pdf*; accessed: 03.08.2015

⁴ Online source: <http://hub.globalccsinstitute.com>, Publication: *CCS roadmap for industry: high purity CO₂ sources*, accessed 03.08.2015

⁵ U.S. Department of Energy, Hydrogen Energy Data Book, <http://hydrogen.pnl.gov/>, subsection: hydrogen production, 04.08.2015

are approximately 6 U.S./GJ [Uddin and Daud, 2014]. Compared to that, the estimated production costs for electrolysis with light water reactors using grid electricity are between 4.36 and 7.36 U.S./kg [Bartels et al., 2010].

Even though the production prices of hydrogen will further decrease with increasing demand, there are still concerns relating this energy carrier. One of the biggest concerns is relating to the hydrogen production from natural gas using the SMR route, because in a typical SMR plant each million m³ of H₂ per day simultaneously produces 0.3-0.4 million standard m³ of CO₂ per day [Balat and Kirtay, 2010].

2.1.2.1. Hydrogen on a renewable basis

With regard to a sustainable and environmentally friendly energy future the focus has turned towards a renewable hydrogen production. At present, with regard to the hydrogen production costs only the gasification of biomass seems to be competitive, as the estimated costs are in the range of 1.44 - 2.83 U.S./kg [Uddin and Daud, 2014]. Compared to that, as well as to SMR, the production cost of hydrogen from gasification of lignocellulosic biomass is 3 times higher with 10-14 U.S./GJ [Balat and Kirtay, 2010]. Estimated costs for electrolysis are between 2.27-6.77 U.S./kg when using wind energy in the range of 5.78 to 23.27 U.S./kg when using solar energy [Bartels et al., 2010].

From a commercialization point of view many of the before mentioned production routes are still in their infancy. Large-market opportunities could increase the level of manufacturing volume which would result in substantial production cost reductions. The DoE identified two particular areas in their report⁶, the transportation sector with an FCV market being on the verge of emerging and probably the most discussed. Secondly, hydrogen production could be used as storage option for surplus renewable electricity. In this case electricity is used to produce hydrogen via electrolysis, which is then stored in tanks or caverns or could be injected into the hydrogen grid.

2.1.3. Purification of renewable hydrogen from bioprocesses

Most common methods for the purification of hydrogen are used in industrial applications with the task to separate various impurities from a hydrogen-rich product gas. The methods particularly for CO₂ separation can be divided into absorptive, adsorptive, membrane and cryogenic separation techniques. Choosing a suitable technology for the separation of carbon dioxide depends mostly on the characteristics of the feed gas stream, especially the CO₂ partial pressure, extent of CO₂ recovery

⁶ U.S. Department of Energy, Report of the Hydrogen Production Expert Panel to HTAC, May 2013

required, and regeneration of the solvent [Olajire, 2010]. Subsequently, common used methods of the before mentioned CO₂ separation techniques are presented.

2.1.3.1. Absorptive CO₂ separation techniques

Typical absorptive separation methods can be divided into three categories, based on their type of binding: I.) physical, II.) chemical, and III.) mixed physical-chemical.

I.) **Physical:**

Physical solvent processes use organic solvents to physically absorb certain gas components, based on the respective solubility within the solvent [Olajire, 2010]. The solubility of a gas component mainly depends on the partial pressure and temperature of the gas.

Pressure scrubbing

Using water at elevated pressure for the absorption of carbon dioxide has been an important industrial process, especially for the purification of synthesis gas in ammonia production. The pressure dependency of the carbon dioxide solubility is a limiting factor, as the CO₂ partial pressure in the gas should be greater 50 psia to ensure an economically useful carbon dioxide capacity of the water [Kohl and Nielsen, 1997a]. The main advantages of this method are the simple plant design, H₂S can be separated additionally to CO₂, and a solvent is used that is inexpensive and not reactive with O₂ or other trace constituents. But, using water as a solvent causes also the principal disadvantages of pressure scrubbing, such as the very high pumping load, a poor CO₂ removal efficiency, and an impure by-product [Kohl and Nielsen, 1997a]. To make practical applications of pressure scrubbing work economically feasible, a gas feed stream of at least 250 Nm³/h is required [Kohl and Nielsen, 1997a].

Purisol[®] method

In the Purisol[®] method N-methyl-2-pyrrolidone (NMP) is used as physical solvent to capture CO₂ and H₂S [Padurean et al., 2012]. The process is operated at ambient temperature or at reduced temperatures around -15 °C and is reportedly capable of yielding gas streams containing less than 0.1 percent carbon dioxide [Kohl and Nielsen, 1997b].

Rectisol[®] method

The Rectisol[®] method is another physical solvent process that uses low temperature methanol for the removal of CO₂. It was the first physical solvent process [Kohl and Nielsen, 1997b] and has mainly been used to treat synthesis gas or hydrogen

to remove impurities such as carbon dioxide [Olajire, 2010]. Operating temperatures of the Rectisol[®] process are as low as -73 °C, which is much lower than for other physical solvent processes [Kohl and Nielsen, 1997b]. Methanol's carrying capacity for CO₂ at these low temperatures becomes very high, with a still low viscosity so that mass and heat transfer are not significantly impaired [Kohl and Nielsen, 1997b]. Advantages of the Rectisol[®] method cover inter alia: it is non-corrosive, there are no degradation problems, and the solvent can be easily regenerated. One of the disadvantages is that there is a need to refrigerate the solvent, which results in high capital and operating costs [Olajire, 2010].

Selexol[®] method

This method has been applied for decades to process natural gas, using dimethyl ether of polyethylene glycol as scrubbing solvent. It was originally used to remove CO₂ in ammonia plants, but soon found its application in H₂S and CO₂ removal from natural gas [Kohl and Nielsen, 1997b]. Among the advantages of this process are its minimal plant and operation costs, low operation pressure, and low heat rise, since no chemical reaction occurs. Disadvantages are the solvent's high affinity to heavy hydrocarbon and the demand in high operating pressure for a more efficient process [Olajire, 2010]. The utilization of polyethylene glycol dimethyl ether as an alternative solvent in the Selexol[®] method is known as the Genosorb[®] process [Yave et al., 2010].

Flour process

For separation of carbon dioxide with high partial pressure in the feed gas, the Flour solvent method is one of the most attractive processes [Olajire, 2010]. The utilized physical solvent is propylene carbonate, which has a high affinity for CO₂ [Olajire, 2010, Kohl and Nielsen, 1997b]. This high CO₂ affinity results into one of the process advantages, a high solubility and enhanced CO₂ loading. Another advantage is that there are only low modifications necessary if the CO₂ content in the feed gas changes. Unfortunately, propylene carbonate is very expensive [Olajire, 2010].

II.) Chemical:

Chemical absorption of CO₂ depends on acid-base neutralization reactions using basic solvents. Absorption is preferred for low to moderate CO₂ partial pressures, but carbon dioxide is much more easily absorbed into solvents at a high total pressure [Olajire, 2010]. This limits the recovery of carbon dioxide.

Potassium carbonate washing

The application of potassium salts for CO₂ removal is well known and its use is widely spread. Potassium carbonate washing is seen as an extremely simple process

[Kohl and Nielsen, 1997c], where carbonate is transformed into bicarbonate during the absorption cycle [Borhani et al., 2015]. The utilization of hot potassium carbonate results in a high-absorber temperature which makes the need of additional heat for the stripper column redundant [Kohl and Nielsen, 1997c]. One disadvantage of this method is that it is not suitable for fine purification at low CO₂ partial pressures [Borhani et al., 2015].

Amine-based methods

The utilization of amine solution for stripping is a commercialized and probably the most matured technology in natural gas industry [Olajire, 2010]. There are different amine solutions in use, which can be divided into: i.) primary amines, such as monoethanolamine (MEA), ii.) secondary amines, such as diethanolamine (DEA) and diisopropylamine (DIPA), iii.) tertiary amines, such as methyl diethanolamine (MDEA), and iv.) sterically hindered amines, such as aminoethers, aminoalcohols and piperazine derivatives [Olajire, 2010]. For primary, secondary and tertiary amines the majority of the CO₂ is captured by the formation of bicarbonate [Kenarsari et al., 2013].

Aqua ammonia process

A method to capture all three major acid gases (SO₂, NO_x, CO₂) is the aqueous ammonia process. The major by-products are ammonium bicarbonate, ammonium nitrate, and ammonium sulfate. These can be used as fertilizers for certain crops. Aqueous ammonia scrubbing is mentioned to be able to avoid the shortcomings of the MEA process [Olajire, 2010].

Dual-alkali absorption approach

A modified Solvay dual-alkali approach, with ammonia as a catalyst, can be used to generate sodium carbonate via the reaction of CO₂ with sodium chloride [Olajire, 2010].

III.) Mixed physical-chemical:

With the combined use of the physical desorption by flash and the chemical desorption by heating the absorption process can be improved. These processes are also known as mixed solvent processes.

Sulfinol[®] washing

In a mixed solvent process, the physical solvent removes the bulk of the acid gas while the chemical solvent (e.g. alkanolamine in the Sulfinol[®] process) purifies the process gas to stringent levels, all in a single step. The presence of the physical solvent enhances the solution capacity, especially when the feed gas stream is at high pressure

and acidic components are present in high concentrations. The Sulfinol[®] solvent consists of sulfolane (tetra-hydrothiophene dioxide), an alkanolamine which is usually diisopropanolamine or MDEA, and water [Kohl and Nielsen, 1997b].

Amisol[®] method

The Amisol[®] process, which is similar to the Sulfinol[®] process, can be used for either selective desulfurization or complete removal of CO₂, H₂S, and other organic sulfur compounds. Specific alkylamines are used for the absorption process, namely diisopropylamine (DIPA) and diethylamine (DETA). According to Kohl and Nielsen [Kohl and Nielsen, 1997b], these water soluble alkylamines differ from MEA and DEA as they have i.) greater chemical stability, ii.) higher acid gas loading, iii.) high H₂S selectivity, iv.) easier regeneration, and v.) higher volatility.

2.1.3.2. Adsorptive CO₂ separation techniques

Adsorption addresses the physical or chemical attachment of a gaseous substance to a solid material. In the case of CO₂ adsorption, carbon dioxide adheres on the surface of an adsorbent [Mondal et al., 2012]. Depending on the solid material used and regeneration technique applied, different methods need to be distinguished: i.) pressure swing adsorption, ii.) temperature swing adsorption, iii.) vacuum pressure swing adsorption, and iv.) electrical swing adsorption. There are also different adsorbents that are utilized in adsorptive CO₂ separation techniques. Molecular sieves, for example, separate molecules based on their molecular mass or molecular size and they are believed to be cost-effective [Mondal et al., 2012]. Activated carbons, on the other hand, have well developed micro- and meso-porosities and are used in a wide range of industrial processes [Olajire, 2010].

PSA – Pressure swing adsorption

In PSA elevated pressure is used to enhance the absorption of CO₂ in the absorbent. The absorbent can be regenerated by reducing the pressure and purging with a gas that has low absorptivity [Mondal et al., 2012].

TSA – Temperature swing adsorption

When using TSA the absorption of CO₂ takes place in the same way as for PSA, but the regeneration of the solvent occurs under elevated temperature, which needs to be supplied additionally [Mondal et al., 2012].

VPSA – Vacuum pressure swing adsorption

Vacuum swing adsorption is a commercially available technology for gas purification and seems very promising for the removal of CO₂. High pressure is applied

during the adsorption of preferential components and in contrast to PSA, the regeneration of the adsorbent occurs under low pressure. This technology is simple to operate and has a relatively low energy requirement. VPSA is an economical adsorption technique, especially at CO₂ gas concentrations in the range from 15% to 55% [Ling et al., 2015].

ESA – Electrical swing adsorption

ESA is believed to be more cost-effective for CO₂ capture than PSA, TSA, and VPSA. The difference to the other methods is that low voltage electric current is passed through the adsorbent for regeneration purposes [Mondal et al., 2012].

2.1.3.3. Cryogenic separation techniques

Cryogenic methods are used to purify process gases for applications requiring very high purity and high-tech industries such as semi-conductors, the space industry, or particle accelerators. It is used commercially to separate CO₂ from gas streams with high carbon dioxide content [Mondal et al., 2012]. The CO₂ can be separated from the gas by fractional condensation and distillation at low temperature [Olajire, 2010]. The main advantages are that it can be operated at atmospheric pressure and no chemical absorbents are required [Mondal et al., 2012].

2.1.3.4. Membrane separation techniques

A novel method to separate CO₂ from a gas stream is the utilization of selective membranes. Membranes are semi-permeable barriers that separate gases based on diverse mechanisms, such as solution-diffusion, adsorption-diffusion, molecular sieving or ionic transport. Typically used material types are based on polymers, carbons, zeolites, ceramics, or metals and can be from porous to non-porous [Olajire, 2010]. For all transport mechanisms the basic separation principle stays the same, where a certain component of a gas passes the membrane at a higher rate than the other components. Detailed information about the utilization of membrane for the purification of hydrogen-rich gases will be given in chapter 4.1.2.

2.1.3.5. Emerging technologies for CO₂ capture

There are several technologies under investigation for carbon dioxide capture. For example enzyme based separation, hydrate based separation, and calcium looping [Mondal et al., 2012]. Furthermore, several investigations on new membrane materials such as facilitated transport membranes or mixed matrix membranes give reason to be confident about their application in CO₂ separation processes.

2.1.4. Storage of hydrogen

Like any other product, hydrogen needs to be stored and transported to bring it from production to final use. In this content it is an indomitable challenge to find a cost-effective method. An overview about currently available hydrogen storage technologies is given by Niaz et al. [2015], addressing the possibilities for hydrogen to be stored in compressed form, in liquid form or in certain storage material. When hydrogen is compressed, it is typically up to 350 bar which requires high pressure tanks. Unfortunately, this method is volumetrically and gravimetrically inefficient. Compared to that, liquefying hydrogen via the cryogenic storage method is much more efficient. But, as hydrogen is cooled down to 20 K, the tanks need to be well insulated. Another option is to store hydrogen in certain material. In this case, two options have to be distinguished, the chemical storage and the storage via physisorption. Chemical storage uses technologies in which hydrogen is generated through chemical reaction, with typically used materials like ammonia, metal hydrides, formic acid, carbohydrates, and liquid organic hydrogen carriers. Contrary to that, physisorption is a process where the hydrogen molecules get absorbed at the surface of the material. Commonly used materials for physisorption are porous materials such as carbon materials, zeolites, metal organic frameworks, covalent organic frameworks, micro porous metal coordination materials, clathrates and organotransition metal complexes. Subsequently, the before mentioned hydrogen storage techniques are discussed briefly:

Compressed hydrogen

Hydrogen can be stored in its pure form in compressed cylinders at common pressure values between 200 and 350 bar [Dalebrook et al., 2013]. The resulting volumetric capacity is in the range of 30 – 40 kg/m³. According to the U.S. DOE systems with up to 700 bar are already been demonstrated in hundreds of prototypes and are also commercially available with low production volumes. There are still some issues that need further improvement, such as rapid H₂ loss in an accident or hydrogen's long-term effects on the materials under cyclic or cold conditions [Riis et al., 2006]. Even though compressing hydrogen is a simple technology, the process can be seen as volumetrically and gravimetrically inefficient [Niaz et al., 2015].

Liquid hydrogen

The most common way to liquefy hydrogen is to cool it down to cryogenic temperatures [Riis et al., 2006]. The liquefaction of hydrogen results in higher densities compared to compressed hydrogen systems, with a volumetric capacity of 70 kg/m³. The theoretically possible volumetric density is 80 kg/m³, but in today's applications only 20 wt% are reached. Another drawback of this technology is that 30 – 40 % of the energy contained in the hydrogen need to be provided to generate the required low

temperatures (20 K) for liquefaction [Riis et al., 2006]. Furthermore, high efficiency insulated cryogenic vessels are needed for the storage [Barthélémy, 2012].

Hydrogen storage in material

For the subsequent presented hydrogen storage methods in materials, the capture and release mechanisms are based either on adsorption, diffusion, chemical bonding, or Van der Waals attraction and dissociation. According to Niaz et al. [2015], there are two major categories to distinguish: i.) chemical storage, and ii.) physisorption.

In chemical storage the hydrogen is bonded and released through a chemical reaction. The utilized chemical storage media can be comprised of solid or liquid phase components. In both cases, thermal or catalytic decomposition needs to be initiated to release the hydrogen from the source material [Dalebrook et al., 2013]. Typical liquid source materials are ammonia, hydrazine, alcohols, formic acid and liquid organic hydrogen carriers (LOHC). Solid chemical hydrogen storage materials are metal hydrides, metal hydride alloys, and complex hydrates including borohydrides, alanates and transition metal hydrides. The synthesis of hydrogen and nitrogen to ammonia is a well-developed technology, with ammonia tending to possess ease in catalytic decomposition. When ammonia is mixed with water it can be stored in liquid form at room temperature and pressure [Niaz et al., 2015]. LOHCs are rechargeable organic liquids that are used to indirectly store hydrogen in liquid form. An ideal reaction results in volumetric and gravimetric densities of 43 kg/m³ and 6.1 wt%, respectively. The biggest issue with LOHCs such as methyl cyclohexane or toluene is that these liquids need to be handled with great care [Riis et al., 2006].

In physisorption, or physical adsorption, hydrogen is stored on the surface of a porous material. Physical adsorption is a reversible process and occurs on a molecular level. When using carbon materials as carrier material, the hydrogen gets absorbed on the surface by Van der Waals bonding. These amorphous carbonaceous materials possess high degrees of porosity accompanied by large specific surface areas. Typical carbon materials are fullerenes, carbon nanotubes and graphene, with respective hydrogen capacities of 9 wt%, 6 wt%, and 2.6 wt% as reported in literature [Dalebrook et al., 2013, Niaz et al., 2015]. Another possibility for physisorption is the utilization of zeolites, which are complex aluminosilicates with engineered pore size and high surface areas [Riis et al., 2006]. They are commonly used in non-hydrogen gas capturing processes and have been trialed as applications for hydrogen storage over the last several decades [Dalebrook et al., 2013]. The basic principle of hydrogen storage in zeolites is the following: i.) when elevated pressures and temperatures are applied, the hydrogen is forced into the cavities of the zeolite; ii.) cooling the zeolite back to room temperature keeps the hydrogen trapped in the cavities; and iii.) to release the hydrogen

from the zeolite the temperature has to be increased again. Typically used zeolites are metal-organic frameworks (MOFs), covalent organic frameworks (COFs), micro porous metal coordination materials (MMOMs), and clathrate hydrates [Niaz et al., 2015]. Further physisorption materials are glass capillary arrays, glass microspheres and organotransition metal complexes.

Another possibility would be the utilization of hydrogen to generate electricity and store it in an electric form. However, the work of Marchenko and Solomin [Marchenko and Solomin, 2015] shows that a comparison in terms of energy and expenditure favors the hydrogen pathway over electricity as a long-term energy storage system. It is apparent that the development of secure, economic and efficient storage systems is a major factor in establishing a hydrogen society.

2.1.5. Power to gas concept

To enable the transition to a renewable energy system, large scale energy storage will be required. On the one hand, to compensate for short-term and seasonal imbalances due to the fluctuating and intermittent nature of renewable energy sources such as solar and wind power [Gahleitner, 2013]. On the other hand, to save temporary excess power from renewable energy sources that could easily substitute fossil fuels in many sectors, e.g. the transportation sector [Varone and Ferrari, 2015]. This can be achieved by the conversion of electricity into hydrogen via electrolysis, which is also known as power-to-gas (PtG) technology. The total concept of PtG can also include a subsequent conversion of H₂ to CH₄ by using external CO or CO₂ sources. Whether if its hydrogen or methane, in this concept the power grid and the gas grid are linked via the conversion of surplus power into a grid compatible gas [Götz et al., 2016]. The process of water electrolysis is the core element of this concept. Typically used electrolysis concepts are alkaline water electrolysis, acidic proton exchange membrane electrolysis, and high temperature electrolysis [Schiebahn et al., 2015]. These have already been discussed in section 2.1.1. The hydrogen produced by these means can take three different routes to the end-user: i.) storage and/or further use of hydrogen via fuel cell or in industrial processes; ii.) direct feed-in of hydrogen into the gas grid; and iii.) methanation of the hydrogen with CO₂ and subsequent feed-in into the gas grid.

Storage

Several possibilities for hydrogen storage have been discussed in chapter 2.1.4. With regard to PtG, Kötter et al. [Kötter et al., 2015] states that it has the potential to become the principal energy storage concept for large-scale implementation and to be the optimal long-term energy storage technology. But, to store hydrogen in long-term Schiebahn et al. [2015] point out that this requires capacities in a high order, which can

only be provided by underground reservoirs. This can be realized by depleted oil and gas fields, aquifers, and/or salt caverns.

Feed-in into the gas grid

Another important topic in the PtG concept is the distribution of hydrogen. As most countries have a well-developed infrastructure, the natural gas distribution system can be used for the feed-in of hydrogen. Unfortunately, the feed-in has its limitations as the maximum allowable concentration of hydrogen in the gas distribution network needs to be taken into account [Schiebahn et al., 2015]. This restriction can be circumvented by converting hydrogen to methane via methanation and feeding it subsequently into the gas grid.

Methanation

Methane can be generated from hydrogen and carbon dioxide via the Sabatier process. The needed CO₂ for the reaction shall be provided at a high purity with low economic and energy effort. According to Schiebahn et al. [2015] possible sources for CO₂ are i.) fossil power plants, ii.) biomass, iii.) industrial processes, or iv.) air. There are several reactor concepts for catalytic methanation used, typically fixed-bed and fluidized-bed reactors, but novel concepts such as three-phase and structured reactors are also under development. An alternative approach is the biological methanation, where methanogenic microorganisms serve as biocatalysts to produce methane from H₂ and CO₂. Biological methanation has the advantage of a higher tolerance according to impurities compared to catalytic methanation, but it is just an option for small plant sizes [Götz et al., 2016].

The major drawbacks of the PtG concept are the low efficiencies and the high costs, and need to be addressed by research [Götz et al., 2016]. For a better understanding of the PtG concept, Gahleitner [2013] provides information about capacities and operating experiences of numerous PtG pilot plants all over the world, which apply hydrogen for electricity generation or feed it into the gas distribution system.

2.2 Utilization of hydrogen

In this section common areas of hydrogen application are described. The bulk of worldwide produced hydrogen is used in refineries, as already shown in chapter 2.1.2. These large-scale utilization routes are described in the following subsections, as well as applications which currently seem to be on the fringes.

2.2.1. Hydrogen for industrial use

Hydrogen is an essential raw material in many industrial applications. It is used in petroleum, chemical, electronics, metallurgical, aerospace, food, and pharmaceutical industry, to mention a few. According to Ramachandran and Menon [1998], the majority of worldwide produced hydrogen finds its application as a reactant in chemical and petroleum processing industries. In chemical industry it is used to manufacture ammonia and methanol, which are two very important basic chemicals. Ammonia production consumes 53% of worldwide produced hydrogen, followed by 20% for refinery processes, 7% for methanol synthesis⁷.

Ammonia production

The synthesis of ammonia is based on the Haber-Bosch process, where hydrogen and nitrogen are reacted at high pressure. Ammonia is needed in great extent for fertilizer production and in plant industries.

Methanol production

Methanol is produced via the catalytic synthesis of synthesis gas, which consists of carbon monoxide, carbon dioxide and hydrogen. Furthermore, synthesis gas is used in the hydro formulation of olefins to aldehydes and other alcohols.

Oil refinery processes

An oil refinery is both a producer and a consumer of hydrogen, with the amount of hydrogen internally produced usually being smaller. As a consequence, there is demand in additional hydrogen. Its main application is as reactant in hydro-processing and hydrocracking. Hydro-processing describes the hydrogenation of sulfur and nitrogen compounds, and hydrocracking is the simultaneous cracking and hydrogenation of hydrocarbons to produce refined fuels [Ramachandran and Menon, 1998].

Hydrogenation process

Hydrogenation is a chemical reaction between molecular hydrogen and an organic compound, in the presence of heterogeneous or homogeneous catalysts. It finds its application in petrochemical, pharmaceutical, food and agricultural industry. Examples are hydrogenation of adipic acid dinitrile to hexamethylene diamine, hydrogenation of benzene to cyclohexane, or the hydrogenation of phenol to cyclohexanone.

⁷ Online source: <http://www.essentialchemicalindustry.org/chemicals/hydrogen.html>

Metallurgical industry

Hydrogen is used in the reduction stage during the production of nickel [Ramachandran and Menon, 1998]. It is also used to remove oxygen in annealing stainless steel alloys, magnetic steel alloys, sintering, and furnace brazing. Furthermore, it is used as reducing agent for the reduction of metallic ores to extract metals.

Electronics industry

In electronics industry, hydrogen's task is to reduce silicon tetrachloride to silicon for the growth of epitaxial silicon, which is a common process during wafer and circuit manufacturing [Ramachandran and Menon, 1998]. Hydrogen is also used as a carrier gas for such active trace elements as arsine and phosphine.

Pharmaceutical industry

In pharmaceutical industry hydrogen is used to a great extent to manufacture vitamins and other pharmaceutical products.

Food industry

Hydrogen is used to hydrogenate unsaturated fatty acids in animal and vegetable oils, producing solid fats for margarine and other food products.

Aerospace industry

In the history of aerospace industry many propellant combinations have been investigated. A mixture of liquid oxygen and liquid hydrogen has immediately been accepted and extensively used internationally due to its unique high release of energy [Cecere et al., 2014].

Nuclear power reactors

As water dissociates under neutron flux, hydrogen is used as an oxygen scavenger to generate a protective atmosphere and thereby prevent corrosion.

Manufacture of catalysts

Hydrogen is commonly used to reduce metal oxides to their active metallic form and to regulate chain length in the polymerization of propylene to polypropylene. Furthermore, it is applied during manufacturing of polyethylene.

2.2.2. Hydrogen as fuel

There are several pathways for the utilization of hydrogen as fuel. Hydrogen can be used directly as liquid or gaseous fuel, it can be converted to methane and

subsequently used as gaseous fuel, and it can be used in a fuel cell to generate electric power. In the following chapters the direct use and the utilization in a fuel cell are described in detail.

2.2.2.1. Direct use in combustion engines

In the late 90's the primary application of hydrogen as a fuel was in the aerospace industry. But, long before aerospace industry's interest a lot of research was already done regarding hydrogen as fuel for internal combustion engines. For example, in 1807 a first internal combustion engine (ICE) was invented, which was fueled with a mixture of hydrogen and oxygen [Verhelst and Wallner, 2009]. Since then, the interest in hydrogen and other non-conventional fuels as replacement of fossil based fuels in the transportation sector did not diminish. Like gasoline, hydrogen can be used as fuel directly in ICEs. Spark-ignited engines fueled with hydrogen are known as hydrogen internal combustion engines (H₂ICE). Same as for the principle mechanism of gasoline engines, gaseous hydrogen is injected into the engine, where it is burned. Two different hydrogen injection systems are used in H₂ICEs, i.) port fuel injection (PFI), and ii.) direct injection (DI). The respective advantages of these systems are a homogeneous fuel and air mixture for PFI, and that the specific power output for DI exceeds that of gasoline [Verhelst, 2014]. According to Verhelst and Wallner [2009], a 15% increase of power density in DI has been demonstrated, when compared with gasoline. H₂ICEs have less knocking tendency compared to gasoline engines due to its high auto-ignition temperature, finite ignition delay, and high flame velocity. Advantages of hydrogen use in ICEs compared to hydrocarbon fuels are a higher flame propagation speed, wider ignition limits, lower ignition energy [Gupta, 2008]. Furthermore, it offers a less NO_x-emitting and CO₂-free combustion. Another factor in H₂ICEs favor is its utilization allows a bi-fuel operation, as these engines are capable of operating with gasoline as a second fuel option. The main problems with H₂ICEs are the costs, the low density of hydrogen, on-board storage, backfiring, pre-ignition [Verhelst and Wallner, 2009, Verhelst, 2014]. Compared to fuel cell technology, the ICE concept does not rely on rare materials which need to be supplied in large quantities.

2.2.2.2. Hydrogen fuel cell

Fuel cells (FC) are electrochemical power generation devices that are classified based on the electrolyte material used. A fuel cell consists of two electrodes, a negative anode and a positive cathode which are connected by an electrolyte. Hydrogen is fed to the anode, and air is fed to the cathode. A catalyst at the anode separates hydrogen molecules into protons and electrons, which take different paths to the cathode. The electrons go through an external circuit, creating a flow of electricity. The protons migrate through the electrolyte to the cathode, where they unite with oxygen and the

electrons to produce water and heat. There are six different types of fuel cells, i.) alkaline fuel cell (AFC), ii.) direct methanol fuel cell (DMFC), iii.) molten carbonate fuel cell (MCFC), iv.) phosphoric acid fuel cell (PAFC), v.) proton exchange membrane fuel cell (PEMFC), and vi.) solid oxide fuel cell (SOFC) [Gupta, 2008].

Characteristics of fuel cell types [Gupta, 2008, Alves et al., 2013]

AFC	Electrolyte: potassium hydroxide; Operating temperature: 60 – 90 °C.
DMFC	Electrolyte: polymer membrane; Op. temp.: 60 – 130 °C. Pure methanol can also be used as fuel.
MCFC	Electrolyte: immobilized liquid molten carbonate; Op. temp.: 650 °C. This type of fuel cell can also be fueled with coal-derived fuel gases, methane, or natural gas.
PAFC	Electrolyte: immobilized liquid phosphoric acid; Op. temp.: 200 °C. The anode and cathode are made of a carbon and silicon carbide structure with a platinum catalyst coating. It is the most commercially developed fuel cell type.
PEMFC	Electrolyte: ion exchange membrane; Op. temp.: 80 °C. The membrane is coated with platinum, which acts as a catalyst. This fuel cell type is most suited for powering automobiles, because of its durability, low operating temperatures, rapid change in power on demand, and low pollution and noise emissions.
SOFC	Electrolyte: ceramic; Operating temperature: 1000 °C. This type can also utilize other fuels additionally to hydrogen, such as natural gas, biogas, gasoline, methanol and ethanol. It is expected to be used in industry to generate electricity and heat.

The efficiencies for the before mentioned fuel cell types are in a range from 35 – 65 %. PAFCs, MCFCs and SOFCs are of interest for electric stations, whilst PEMFCs stand out as key option for transportation use and small scale power generation facilities. With respect to the transportation sector, hydrogen is one of the main alternatives to gasoline and its utilization in fuel cell powered vehicles is seen as one of only two truly zero-emission vehicle options [Ball and Weeda, 2015] According to Verhelst [2014] FCVs have a potential efficiency at part load, low emissions, and quiet running. Furthermore, they combine the comfort and benefits of electric driving with short refueling time and moderate vehicle range [Ball and Weeda, 2015]. The major

challenges for FCVs are the durability and the costs, with the reason for the high costs in the use of palladium [Verhelst, 2014].

2.3 Standards for hydrogen utilization

This section provides a brief description of the directives for hydrogen utilization in H₂ICEs and FCVs, regarding fuel quality. In 2008 the California Air Resources Board and the Department of Food and Agriculture agreed on specifications for hydrogen fuels for use in internal combustion engines and fuel cells in motor vehicles. Depending on the hydrogen production route, contaminants such as ammonia, carbon monoxide, carbon dioxide, formic acid, hydro carbons or sulfur can occur. These contaminants can harm the engines' or fuel cells' performance and efficiency. The defined specifications contain a minimum hydrogen purity of 99.97 vol% [California Department of Food and Agriculture, 2008]. For H₂ICEs the specifications regarding H₂ and CO₂ content are a little exaggerated, because internal combustion engines would be able to run at lower hydrogen quality [Miltner et al., 2010]. Another product specification standard for hydrogen as fuel is in the ISO 14687:1999 of the ISO/TC 197. This standard differentiates according to application resulting in three types with respective sub groups.

Type I - grade A	Internal combustion engines for transportation; residential or commercial appliances.
Type I - grade B	Industrial fuel, for use e.g. in power generation or as a heat energy source.
Type I - grade C	Aircraft and space-vehicle ground support systems.
Type II	Aircraft and space-vehicle onboard propulsion and electrical energy requirements; off-road vehicles.
Type III	Aircraft and space-vehicle onboard propulsion.

Additionally to the minimum hydrogen content, the maximum permitted values for defined impurities are given. Impurities are water, total hydrocarbon, oxygen, argon, nitrogen, helium, carbon dioxide, carbon monoxide, mercury, sulfur, and permanent particulates. For H₂ICE (Type I, grade A) a minimum hydrogen mole fraction of 98 % is requested. Table 2.1 lists the respective characteristics of the ISO 14687:1999 standard.

Table 2.1: Characteristics for hydrogen purity based on ISO 14687:1999 of the ISO/TC 197

Sub clause	Characteristics (assay)	Type I			Type II	Type III
		Grade A	Grade B	Grade C		
6.2	Hydrogen purity (minimum mole fraction, %)	98	99.9	99.995	99.995	99.995
6.3	<i>Para</i> -hydrogen (minimum mole fraction, %)	NS	NS	NS	95.0	95.0
Impurities (maximum content)						
	Total gases			50	50	
6.4	Water (cm ³ /m ³)	NC	NC	b	b	
6.5	Total hydrocarbon	100	NC	b	b	
6.6	Oxygen	a	100	c	c	
6.7	Argon	a		c	c	
6.7	Nitrogen	a	400	b	b	
6.7	Helium			39	39	
6.8	CO ₂			d	d	
6.9	CO	1		d	d	
6.1	Mercury		0.004			
6.11	Sulfur	2	10			
6.12	Permanent particulates	f	e	e	e	
	Density					e

Dimensions in micromoles per mole unless otherwise stated

NOTE 1 NS: Not specified

NOTE 2 NC: Not to be condensed

a - Combined water, oxygen, nitrogen and argon: max 1900 pmol/mol

b - Combined water, nitrogen and hydrocarbon: max 9 pmol/mol

c - Combined oxygen and argon: max 1 pmol/mol

d - Total CO₂ and CO: max 1 pmol/mol

e - To be agreed between supplier and customer

f - The hydrogen shall not contain dust, sand, dirt, gums, oils, or other substances in an amount sufficient to damage the fuelling station equipment or the vehicle (engine) being fuelled.

3. Aim of this work

The main objective of this work was the design and development of an innovative small scale bio-hydrogen purification process using membrane technology. Thereto, commercially available membrane material was installed into membrane modules and tested in the laboratory for its suitability. To investigate the membrane material under real conditions the designed small scale pilot plant was connected to a dark fermenter, which produced a hydrogen and carbon dioxide rich biogas. During these field tests the effect of varying operational conditions on the purification performance was examined. The insights gained during experimental tests together with previous simulation work served as design basis for a simulation model of a membrane unit operation. This unit operation was then further developed and adjusted for the present purification task. To confirm the accuracy of the developed model, data obtained from laboratory and field tests served for validation. The validated unit operation was applied in various multi-stage configurations to determine an effective and robust purification process. Besides the utilization of commercially available membrane material as prerequisite, a certain purification quality was also prescribed. This hydrogen quality and the related hydrogen recovery were two of several factors used to determine the process' purification performance. Furthermore, the required membrane area, specific energy demand and possibilities for off-gas utilization were also taken into consideration. In the end, these factors were used for comparison and to determine which process configuration was best suitable for separation of hydrogen and carbon dioxide during fermentative hydrogen production.

4. Description of the overall process

This chapter will provide a short introduction into the overall process containing fermentation, CO₂ separation with membrane technology and the potential of a subsequent off-gas utilization. The process was developed in course of the H₂MemClean project (FFG number 829890) founded by the Austrian Research Promotion Agency. Figure 4.1 shows the overall process, including the main competences of the project partners.

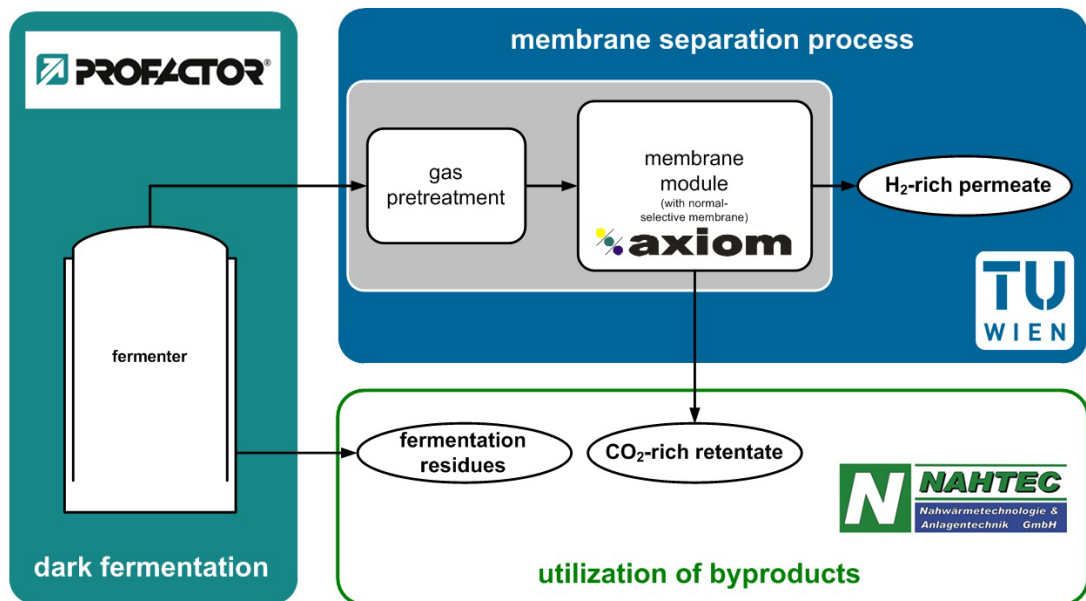
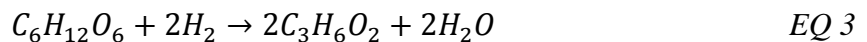
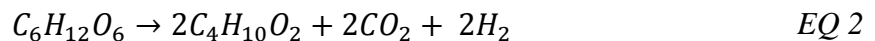


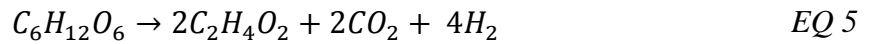
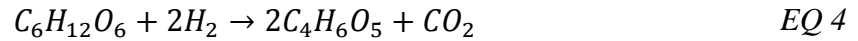
Figure 4.1: Overall process with allocation of the H₂MemClean project partners' main competences

The subsequent chapters address the principles of hydrogen production via dark fermentation, with regard to the anaerobic metabolism and several pathways in fermentative hydrogen production. Furthermore, utilized bacteria and operational conditions are presented. The chapter of fermentative production of hydrogen is concluded by information about suitable substrates for dark fermentation. Hereinafter the focus shifts to membrane separation, particularly on membrane materials suitable for hydrogen upgrading and types of modules available for purification applications. The Chapter is concluded with the utilization of by-products, with regard to the energy potential remaining in the off-gas.

4.1 Fermentative production of hydrogen

Dark fermentation has already been mentioned in chapter 2.1.1 as a possible hydrogen production route from biomass feedstock. Urbaniec and Bakker [Urbaniec and Bakker, 2015] consider it as one of the most environmentally friendly alternatives for satisfying future hydrogen demand. The fermentative production of hydrogen actually refers to the dark-fermentative bio-hydrogenases. During dark-fermentative bio-hydrogenases an obligate series of microbial processes occur under the absence of air, which is also known as an anaerobic metabolism [Westermann et al., 2007]. During an anaerobic metabolism four stages occur, namely hydrolysis, acidogenesis, acetogenesis, and methanogenesis [Mohan and Pandey, 2013]. For hydrogen production via dark fermentation the utilized anaerobic bacteria need a carbohydrate rich substrate. This requirement is fulfilled by biomass, mainly containing of cellulose, hemicellulose and lignin [Saxena et al., 2009]. Cellulose, which is generally the largest fraction in biomass, is a glucose polymer. Hemicellulose is a mixture of polysaccharides composed of sugars, and lignin consists of cross-linked phenol polymers. The glucose in biomass is the main target point of dark fermentative bio-hydrogenases, as glycolysis is the primary metabolic pathway which is shown in Figure 4.2. During glycolysis the glucose ($C_6H_{12}O_6$) is converted into pyruvate (CH_3COCOO^-), with a simultaneous release of free energy. In the presence of a terminal electron acceptor (TEA) the free energy is used to generate biological energy molecules (ATP). Simultaneously to ATP the free energy also causes the generation of energy-rich reducing powers such as the coenzyme nicotinamide adenine dinucleotide (NADH), which is subsequently re-oxidized during respiration [Mohan and Pandey, 2013]. Under anaerobic conditions typically utilized compounds as TEA are NO_3^- , SO_4^{2-} organic and inorganic compounds. The pyruvate enters the acidogenic pathway which results in hydrogen, but also generates volatile fatty acids (VFA) and alcohols (EQ 5) [Westermann et al., 2007]. Most commonly generated VFA acids during bio-hydrogenases are acetic acid (EQ 1) and butyric acid (EQ 2) [Ghimire et al., 2015]. In the presence of hydrogen, propionic acid (EQ 3), and malic acid (EQ 4) can also be formed. Equation EQ 1 for example shows that a maximum yield of 4 mol hydrogen per mol glucose can be achieved when acetic acid is formed as byproduct.





It can be seen from equations EQ 1 to EQ 5, that the listed fermentation pathways and respective byproducts affect the total amount of produced hydrogen. Producing larger amounts of hydrogen could not only lead to the formation of propionic acid and malic acid, it also happens at the expense of cell growth. As a result, a low hydrogen partial pressure in the product gas is required to reduce the H₂ consuming reactions and to favor the acidogenesis [Westermann et al., 2007, Mohan and Pandey, 2013, Ghimire et al., 2015].

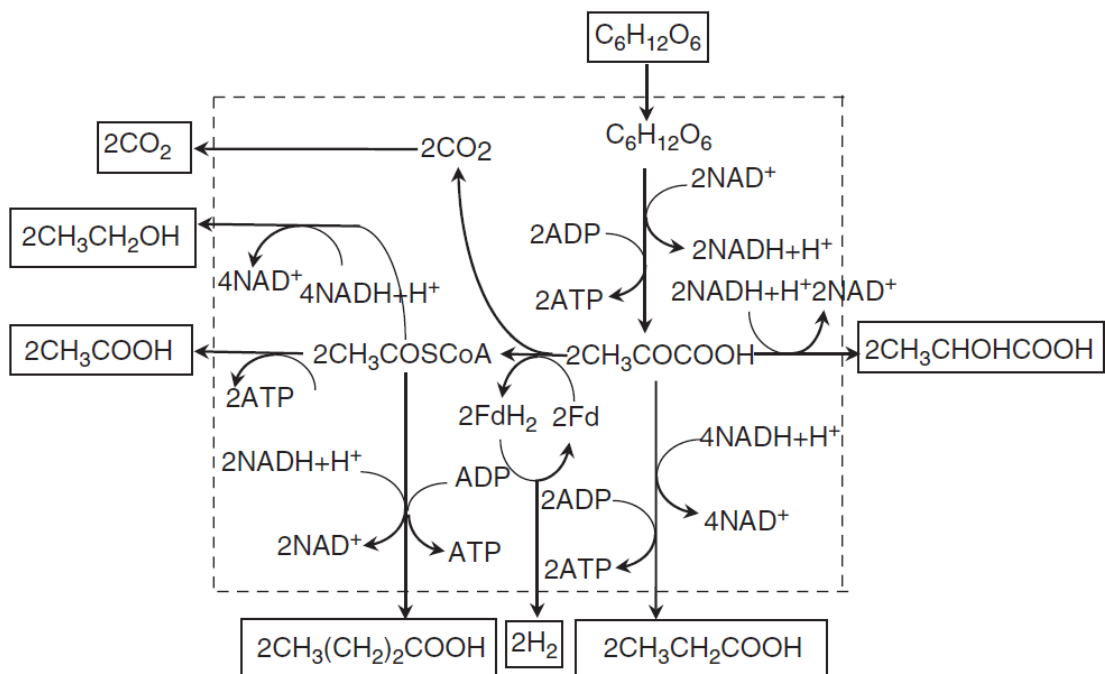


Figure 4.2. Pathways for fermentative hydrogen production; picture taken from [Ren, et al., 2006]

In practical fermentation processes purging with nitrogen is often attempted to lower the partial pressure of hydrogen in the fermenter to circumvent that H₂-consuming reactions get favorable [Westermann et al., 2007].

Utilized bacteria:

Depending on the reactor technology, pure cultures or mixed cultures of either strict anaerobes (e.g. *Clostridium*), facultative (e.g. *Escherchia coli*, *Enterobacter*) anaerobes and aerobes (e.g. *Bacillus*) are used for bio-hydrogenases. The advantage of

mixed cultures is that they are active towards a variety of substrates [Hallenbeck, 2013]. Saxena et al [2009] states that the before mentioned *Enterobacter*, *Bacillus* and *Clostridium* are typical cultures used to produce hydrogen from carbohydrates. Depending on the utilized bacteria there are two metabolic pathways for the anaerobic degradation of the pyruvate according to literature: i.) the pyruvate formate lyase (PFL), which is a special class of [Ni-Fe]-hydrogenase, and ii.) the pyruvate ferredoxin oxidoreductase (PFOR) by the monomeric [FeFe]-hydrogenase [Hallenbeck, 2013]. *Clostridium pasteurianum* is an example for PFOR, and is also known as a high hydrogen producer [Ren et al., 2006, Hallenbeck, 2013]

The type of utilized microorganism is also categorized according to the preferred temperature level, which can be in the mesophilic (35°C), thermophilic (55°C) or extreme thermophilic (>65°C) range [Urbaniec et al., 2010, Ghimire et al., 2015]. Because thermophilic and extreme thermophilic bacteria tend to produce acetic acid as byproduct, their production rates and hydrogen yield is often higher compared to mesophilic bacteria [Urbaniec et al., 2010].

Operational conditions:

The hydrogen production via dark fermentation depends on numerous parameters such as inoculum type, enrichment methods, bioreactor design, as well as operational conditions [Ghimire et al., 2015]. For the latter Lay et al. [2010] denotes that the hydraulic retention time (HRT) and the organic loading rate (OLR) are the main parameters effecting hydrogen production in a continuous hydrogen fermentation process. The pH value can also have a vital impact on the hydrogen production rate, as it influences the metabolic by-products [Ghimire et al., 2015], as well as the hydrogen consuming microbes which grow slowly at a neutral pH [Westermann et al., 2007]. Inhibiting these microbes via pH control enhances the hydrogen producing fermentation pathways. As an example, in a pilot-scale study of biohydrogen production Ren et al. [2006] found the maximum hydrogen production rate with an OLR around 28 kg COD/m³reactor/d (COD: chemical oxygen demand), with a set feed pH in the range of 5 - 6.5, and a HRT of 4.2 hours. A further effect on the biohydrogen production can be due to the operational temperatures, i.e. mesophilic, thermophilic and extreme thermophilic conditions [Ghimire et al., 2015]. The applied temperature mainly affects the activity of the utilized bacteria.

Substrates for dark fermentation:

The hydrogen yield and production rate is highly depended on the carbohydrate content in the substrate, bioavailability and biodegradation rate [Ghimire et al., 2015]. Pure glucose, sucrose and starch mixtures have been used in many studies on dark fermentation [Wang and Wan, 2009]. Molasses, which is commonly used in food

industry, is also a very applicable substrate, because it is easy to degrade under anaerobic conditions [Ren et al., 2006]. All these easily accessible sugar-containing substrates are mainly gained from first generation residues, for example energy crops. The utilization of such first generation residues is often in conflict with other biological pathways and even the food industry. To circumvent this, alternative sources of carbohydrate-rich substrates are of great interest. In this context second generation biomass, such as lignocellulosic residues and wastes, seems to have great potential in this context. Urbaniec and Bakker [2010] name in their review numerous lignocellulosic biomass residues and wastes that are widely available for biohydrogen production. For example, vegetal agricultural wastes such as manure or other wastes from farms, and harvest residues such as wheat straw, corn stover and barley straw etc. are mentioned as a potential source for conversion to biofuels. Other possible sources for dark fermentation are agro-industrial residues and by-products. Examples for the latter are wheat mill feed, wet distiller's grain, beet pulp, or fruit pomace. Since there is a considerable amount of energy accessible coming from biomass-processing [Urbaniec et al., 2010], its utilization would furthermore have a positive effect environmental issues [Ren et al., 2006]. One of the biggest challenges with biomass as feedstock is the pretreatment and saccharification of lignocellulosic materials. This conversion step is necessary to make the sugars in the substrate easily accessible for fermentation. Furthermore, Urbaniec and Bakker [2015] identify the suitability of various kinds of feedstock as widely differentiated and difficult to assess, because the pretreatment methods and fermentation conditions are not standardized. Westermann et al. [2007] identifies a major problem for agricultural and municipal wastes as feedstock in the activity of hydrogen utilizing bacteria and methanogenic archaea present in the substrate, which convert hydrogen to methane and acetate. Another concern regarding this technology is pointed out by Urbaniec and Bakker [2015], as they identify a major technological barrier in its ability to match the supply of cost-competitive hydrogen to meet the current demand. Still, when compared to other biochemical routes of hydrogen production from biomass, for example the photosynthesis process, Saxena et al. [2009] considers dark fermentation to be much more versatile. Unfortunately, as Urbaniec and Bakker [2015] state in their review on possible biomass residues for dark fermentation, the high production costs are still a key factor. But there is room for costs reduction, as the pretreatment process adds a decisive share to the production costs. Development in this department could lead to a significant and immediate decrease.

More detailed information about the fundamentals of hydrogen production from biomass feedstock can be found in [Hallenbeck, 2013].

4.2 Membrane separation for H₂ purification: In general

As previously reported, fermentation gas consists mainly of hydrogen and carbon dioxide. The latter is a contaminant that needs to be removed to make the gas viable for applications in H₂ICEs and fuel cells. Thereto membrane separation, especially gas permeation, is used. One influencing factor that determines a successful separation of H₂ and CO₂ is the membrane material. The membrane can be identified as a barrier that shall allow one component to permeate through it while hindering all other components' transport. The permeation rate differs for various species and strongly depends on the membrane material. Detailed information about the principles of gas permeation and the transport theory is presented in chapter 5.2.1.

The first subchapter provides information about typically used material in gas permeation, focusing especially on the hydrogen and carbon dioxide separation task. A high membrane surface area at a correspondingly low overall dimension is one of the major requirements in industrial applications. The efficiently and economically packaging of membrane material is therefore an important factor in membrane applications, which can be done with different types of membrane modules. These industrially used types are discussed in the second subchapter, particularly modules used for gas purification.

4.2.1. Membrane material

Membrane materials for hydrogen purification can be distinguished in many ways, as they are porous or dense, organic or inorganic, H₂-selective or CO₂-selective. Porous membranes are further divided into mesoporous and microporous, with regard to the pore diameter [Adhikari and Fernando, 2006]. Furthermore, the terms isotropic and anisotropic membranes are often used. Isotropic membranes can be porous or dense and consist of uniform composition and structure. Anisotropic, or asymmetric, membranes consist of numerous layers with different structures including a dense and thin surface layer that performs the separation [Baker, 2012]. According to Li et al. [Li et al., 2015], H₂-selective and CO₂-selective membranes can be divided into the following subcategories:

4.2.1.1. H₂-selective membrane material

Membrane material that shows higher H₂ than CO₂ permeation is identified as H₂-selective. The principle is shown in Figure 4.3, where hydrogen permeates through the membrane wall, whilst carbon dioxide is mostly kept on the retentate side of the membrane.

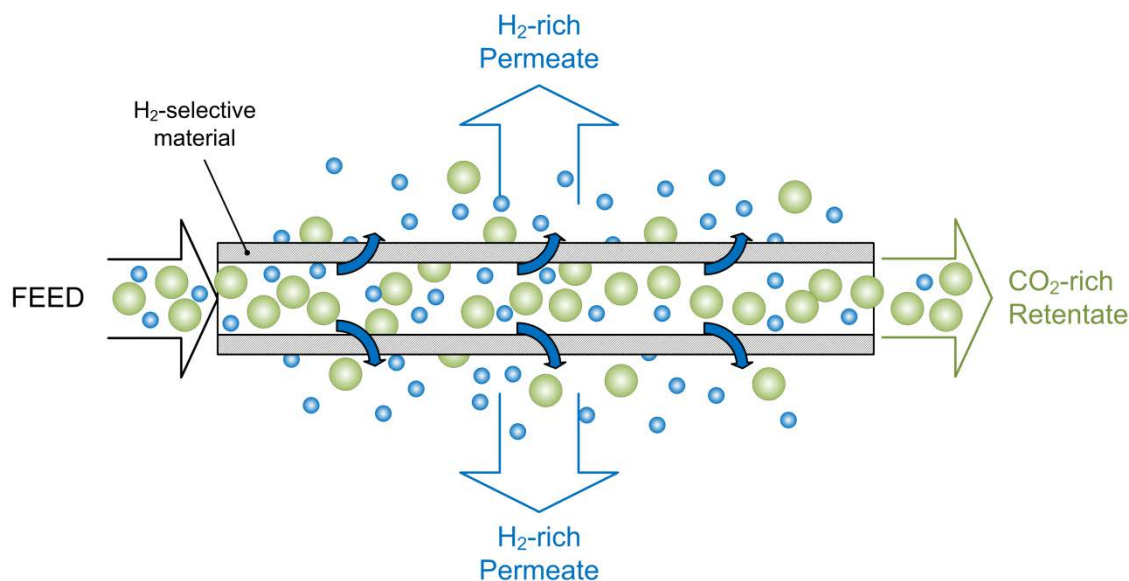


Figure 4.3: Scheme of H₂-selective material

In the subsequent description the H₂-selective membrane material is divided into i.) inorganic, ii.) organic, and iii.) hybrid materials.

Inorganic:

Dense metallic membranes are most common for H₂ purification. Palladium (Pd) and palladium-alloy are typically used, as they are permeable to H₂ with an extremely high selectivity. Metallic membrane can produce hydrogen with 99.99 % purity [Scholes et al., 2010]. This is due to the dissociative chemisorption mechanism, where hydrogen molecules are turned into atomic hydrogen on the surface of the metal, diffuse through the metal lattice and form hydrogen molecules on the surface again. The hydrogen dissociation and recombination reactions can be influenced by contaminants in the feed gas, which is one of the disadvantages of Pd-membranes [Scholes et al., 2010]. The biggest disadvantage of metallic membranes is the low gas permeance. This disadvantage can be counteracted by the combination of a metallic layer on a porous polymeric or inorganic support, as it is realized in composite membranes. Still, these membranes are not suitable for the application of fermenter gas purification due to the high fabrication costs and limited life span.

Microporous inorganic membranes have carefully controlled pore structures [Scholes et al., 2010], they are defined by a pore diameter smaller 2 nm and the separation mechanism is based on the molecular sieving. These membranes generally show better separation at higher temperatures. Typical microporous inorganic membranes are i.) zeolite, ii.) silica, iii.) ceramic, and iv.) carbon-based membranes. Zeolite membranes have excellent mechanical, thermal and chemical stability [Scholes

et al., 2010]. These membranes are the most widely investigated inorganic type, usually supported by porous alumina or stainless steel supports. Silica membranes are typically amorphous, with an ultra-microporous thin layer. These membranes have a superior molecular sieving behavior and show excellent separation especially at high temperatures. Furthermore, hydrophobic silica membranes are associated with low costs [Scholes et al., 2010]. The transport in ceramic membranes is dependent on the membrane structure which can be divided into dense, microporous, or macroporous [Shao et al., 2009]. Most common carbon-based membranes are carbon molecular sieves with amorphous microporous structures, which are either based on porous supports or unsupported. These membranes are widely studied in air separation applications, and show high permeability and high selectivity.

Organic:

Polymeric membranes typically possess rigid structure and narrow free volume distribution. These dense membranes rely on the solution-diffusion mechanism for separation. Typically operating temperatures are less restricted to less than 100 °C. When operating glassy polymers below the glass transition temperature a high H₂/CO₂ selectivity will be provided due to a larger void fraction within the polymeric matrix [Scholes et al., 2010]. Furthermore, a high H₂/CO₂ selectivity can be obtained by increasing the diffusion selectivity and decreasing the solubility selectivity. Common polymeric membranes are i.) polyimide (PI), ii.) polybenzimidazole (PBI) and derivate, and iii.) thermally rearranged polymers. Commercial polyimides are commonly used for pervaporation, nanofiltration, and gas separation applications. Compared to polysulfone and acetate PIs show better separation performance and stability. PIs based on 6FDA are extensively studied and applied materials in gas separation, as they show good permeabilities [Scholes et al., 2010]. PBI is a polymer with an extremely high thermal and mechanical stability, as well as a high H₂/CO₂ selectivity. There are various advanced microporous polymers, such as conjugated microporous polymers, hyper-crosslinked polymers, covalent organic frameworks, thermally rearranged polymers, and polymers of intrinsic micro-porosity. Thermally rearranged polymeric membranes display same permeability and selectivity levels as carbon membranes, while retaining flexibility and malleability [Scholes et al., 2010].

Hybrid – organic-inorganic:

Metal organic framework membranes are a new class of organic-inorganic hybrid porous solid materials. They have geometrically and crystallographically well-defined structures. These structures consist of metal ions or metal ion clusters, which are connected via organic linkers. Variable structure, high porosity, and uniform pore size are among the main advantages of this membrane type. Another group of hybrid

membranes are mixed matrix membranes (MMMs), which are commonly used in gas separation. These membranes consist of organic polymers representing the continuous phase, filled with an inorganic disperse phase. MMMs show great gas separation properties and have good polymer processability.

4.2.1.2. CO₂-selective membrane material

Membrane material with a preferentially higher affinity for CO₂ permeation than for H₂ is referred to as CO₂-selective or as reverse-selective. Figure 4.4 depicts the characteristic of such a reverse-selective membrane material. Compared to H₂-selective material the fabrication of reverse-selective material is more challenging.

There are several types of reverse-selective membranes, such as i.) microporous membranes based on CO₂-preferential sorption, ii.) polymers of intrinsic micro-porosity (PIMs), iii.) CO₂-philic polymeric membranes, iv.) facilitated transport membranes, and v.) mixed matrix membranes.

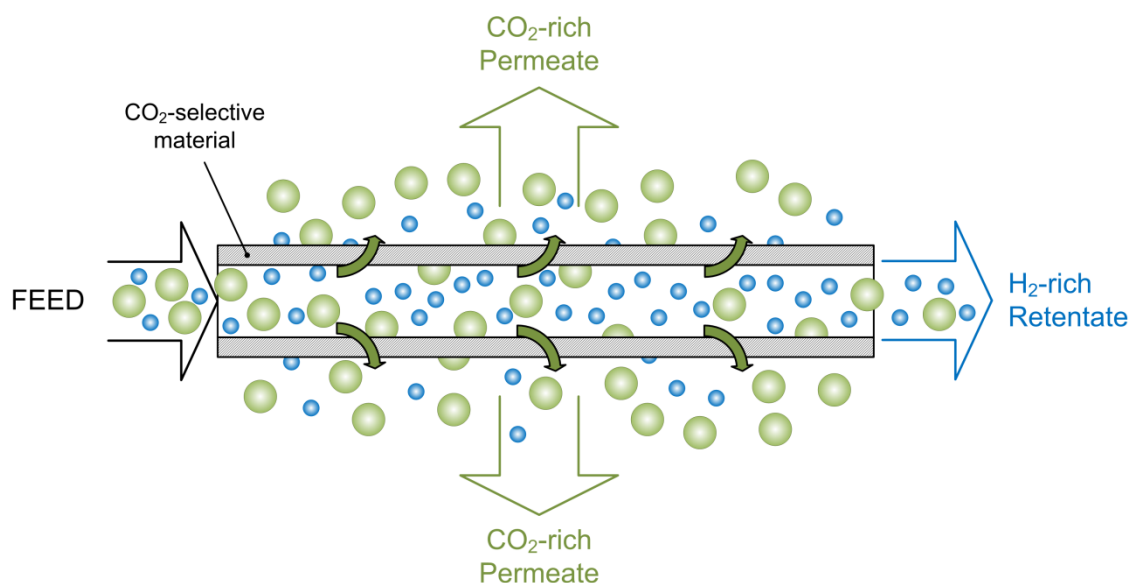


Figure 4.4: Principle of CO₂-selective material

In microporous membranes based on CO₂-preferential sorption the CO₂ transport is generated due to capillary condensation or the surface diffusion mechanism [Scholes et al., 2010]. PIMs possess a ladder-like backbone and a contorted structure that inhibits the freedom of chain rotation to a greater extent. This chain rigidity is closely related to gas transport properties. The aim of CO₂-philic polymers is to get a favorable CO₂/H₂ solubility selectivity compared to the H₂/CO₂ diffusivity selectivity. Poly dimethyl siloxane (PDMS) and poly(amide-b-ethylene oxide) (PEBAX) are such CO₂-selective rubbery polymeric membranes. PDMS and PEBAX show high permeabilities and favor

condensable gases such as CO₂, organic vapors and hydrocarbons. Typical facilitated transport membranes are amino species, polar polymers and ionic liquids. They undergo a reversible complexation reaction with CO₂ within the membrane, dramatically enhancing the solubility [Scholes et al., 2010]. These membranes have a high potential for separation of CO₂ from H₂ at elevated temperature because CO₂ permeability decreases with increasing temperature [Scholes et al., 2010, Shao et al., 2009]. Unfortunately, the long-term stability is a major concern regarding this membrane type. Mixed matrix membranes aim to couple polymer's good processability and inorganic materials' excellent gas separation properties. They are comprised of inorganic particles as the dispersed phase and a polymer matrix serves as the continuous phase. These membranes have a rather complex gas transport mechanism, which basically depends on the type and loading of the inorganic additives and degree of interfacial adhesion between the polymer particles [Shao et al., 2009].

4.2.2. Membrane modules

The membrane material is packed in membrane modules. Depending on the application and the membrane material, different module types are used: i.) plate-and-frame modules, ii.) tubular modules, iii.) spiral-wound modules, and iv.) hollow fiber modules. These types refer to membrane modules in industrial applications. Plate-and-frame modules were one of the earliest types and are used in pervaporation, electrodialysis, reverse osmosis and ultrafiltration applications [Baker, 2012]. Tubular modules are typically applied in ultrafiltration, and spiral-wound modules are commonly used in reverse osmosis and ultrafiltration, as well as gas permeation [Baker, 2012]. The last mentioned type, the hollow fiber membrane module, is used in many applications such as ultrafiltration and pervaporation, but the main application area is gas permeation. Subsequently, more information about hollow fiber modules will be presented, as this type was used in the experimental and simulative part of this work.

There are two basic geometries for hollow fiber membrane modules, shell-side feed and bore-side feed. Three different operational modes can be applied in the respective geometries, namely counter-current, co-current, and cross flow.

Shell-side feed

In this system, the pressure is applied on the shell-side of the hollow fiber membranes. As a result a pressure difference between the hollow fiber outside and inside occurs, which is the driving force for permeation through the fiber walls. The permeate exits the module through the open hollow fiber ends. Figure 4.5 pictures a hollow fiber module with shell-side feed. It can be seen, that the retentate is shell side and exits at the other end of the module. Furthermore, a sweep gas stream can be

applied in this geometry. If the sweep gas is redundant, the basic geometry of the shell-side feed changes to the so called dead end geometry, as shown in Figure 4.6.

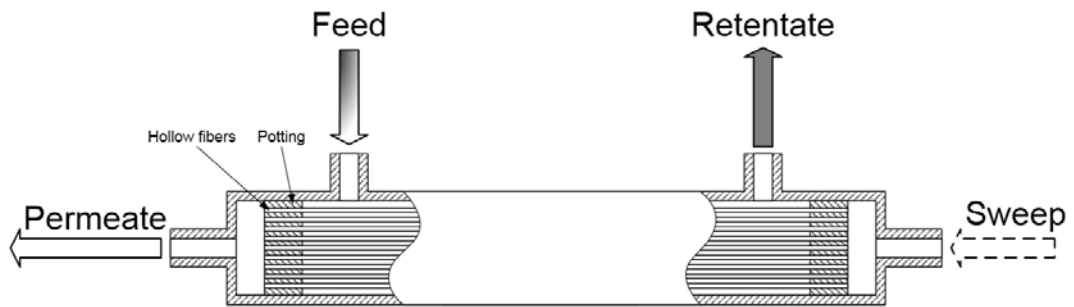


Figure 4.5: Schematic illustration of a hollow fiber module with shell-side feed operational mode and the possibly utilization of a sweep gas

In shell-side feed geometry the fibers usually have small diameters as the fibers must withstand a considerable hydrostatic pressure [Baker, 2012]. An inevitable problem with shell-side feed is the emergence of concentration polarization.

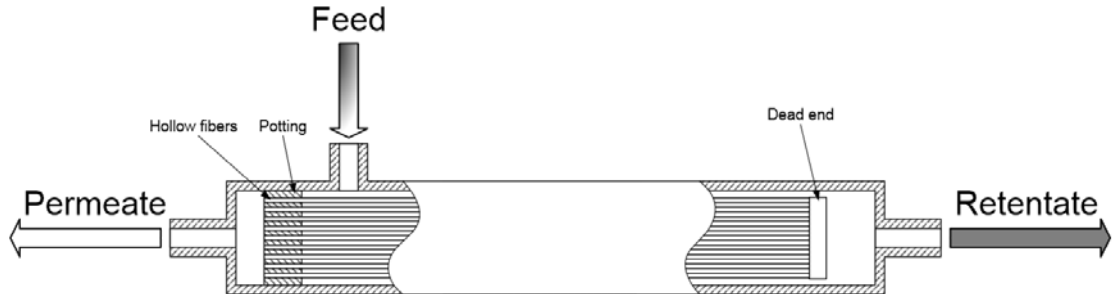


Figure 4.6: Schematic illustration of a hollow fiber module with dead end shell-side feed geometry

Another problem with shell-side feed hollow fiber modules is the pressure drop on the permeate side. Due to the very narrow channel in the fibers a significant pressure drop along the fiber length appears that reduces the pressure difference. The reduction in pressure difference is equivalent to a reduction of the permeation driving force.

Bore-side feed

For bore-side feed geometry, the pressurized gas is fed into the hollow fibers from the bore side. Due to the high pressure inside the hollow fiber and the low pressure on the outside, the gas permeates through the fiber walls from in- to outside. Figure 4.7

shows a schematic illustration of the bore-side feed geometry, including the possibility for a sweep gas.

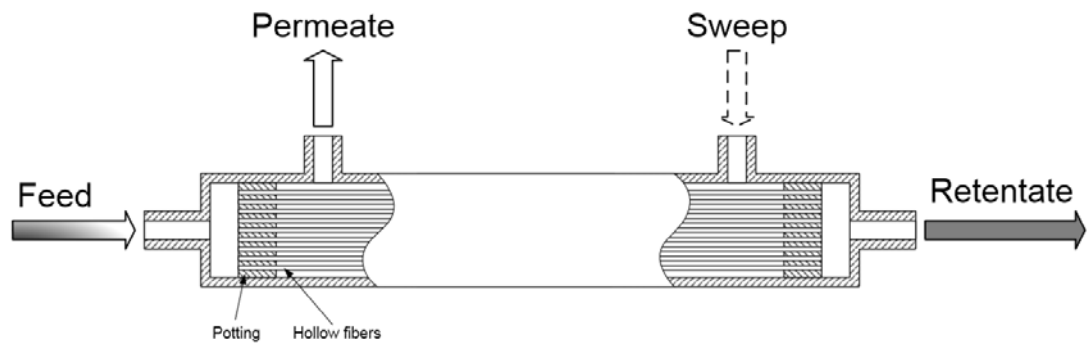


Figure 4.7: Schematic illustration of a hollow fiber module with bore-side feed geometry

Applying sweep gas is not mandatory, but can have a positive effect on the separation. Furthermore, Figure 4.7 shows that the gas flows through the fibers exits as retentate on the other end. It is important for bore-side feed to ensure identical fiber diameters and permeances. One of the advantages is that no stagnant spaces are produced and as a result concentration polarization is well controlled in bore-side feed modules [Baker, 2012].

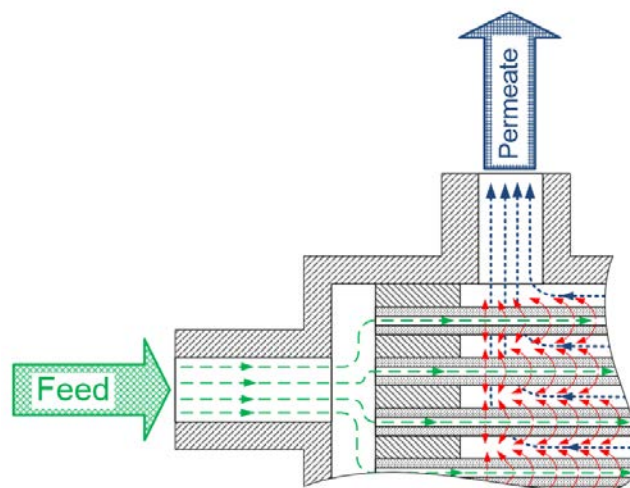


Figure 4.8: Counter-current operational mode in a pore side feed membrane module

As mentioned before, the three different operational modes are regardless of the basic geometry. In counter-current operation the permeate flows in opposite direction of

the feed. Figure 4.8 pictures the basic principle of the counter-current operational mode, with the feed gas entering the fibers on the left side and flowing through it to the right.

The principle of the co-current operation is that feed flow and the permeate flow are in the same direction. Figure 4.9 shows this principle, with the feed gas entering the fibers from the left side and the permeate flowing into the same direction after permeating through the fiber walls. Additionally, a sweep gas stream is shown that enhances the flow of permeate from the left to the right side of the membrane. As mentioned before, the sweep gas stream is not mandatory for separation, but can have a positive effect in certain applications.

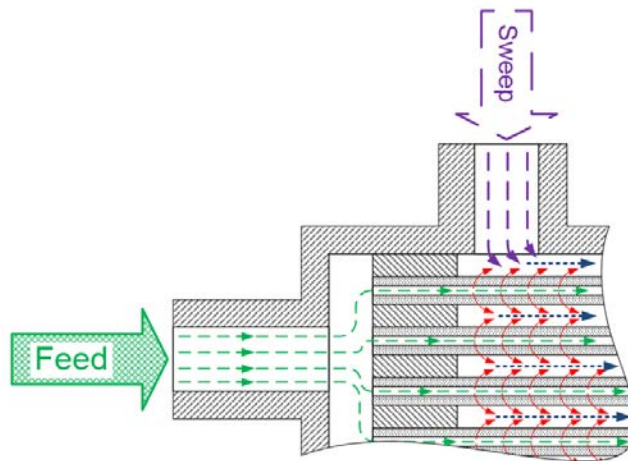


Figure 4.9: Co-current operational mode in a pore side feed membrane module

Another operational mode option is cross-flow, which is not further discussed here as it's neither applied in the experimental nor in the simulative part of this work. Information about it can be found in literature [Baker, 2012].

4.3 Membrane separation for H₂ purification: Selected system

For the purification of the hydrogen-rich fermentation gas, the application of polyimide (PI) fibers in a hollow fiber membrane module was chosen. The main prerequisite for the membrane material was a commercial availability, which is fulfilled by PI. Furthermore, utilizing fibers in a membrane module was a well-based decision, as a large membrane area can be packed into a single module.

4.4 Off gas utilization

A significant part of technically and economically viable operation of a gas processing plant for fermentative hydrogen is the adequate utilization of the separated CO₂-rich off-gas stream. Depending on the membrane material, plant layout and operating conditions a certain hydrogen yield will be achieved, which results in an off-gas stream containing a more or less large proportion of hydrogen. The utilization of the energy content of this stream represents a significant share of an efficient overall concept. Flow rate and hydrogen content are the decisive factors for the selection which approach should be applied on the resulting off-gas. For the given task it was determined that the thermal utilization of the energy content of the combustible gas mixture is of practical importance⁸. In order to assess the analyzed off-gas streams' suitability for energy recovery, it requires the identification of a number of relevant technical combustion parameters. These include the calorific value, the lower heating value, and the flammability limits [Bjerketvedt et al., 1997]. For the given case the flammability limits describe the share of a H₂/CO₂ mixture in admixture with combustion air, which leads to the formation of an ignitable and combustible gas. If it falls below the lower flammability limit (LFL) it results into a lean mixture, whilst exceeding the upper flammability limit (UFL) results into a too rich mixture. Whether lean or too rich, outside these limits a regular combustion cannot be guaranteed. With increasing CO₂ content the lower and higher flammability limits come closer until a certain cut-off grade is reached where an ignitable mixture with combustion air cannot longer be provided [Bjerketvedt et al., 1997]. If the requirements are fulfilled, the generated electricity and heat from combustion of the off-gas can be used for process integration, for example operation of the fermenter and the purification unit.

Other possible applications for the off-gas are in PtG technology, which is described in chapter 2.1.5. In PtG two application scenarios need to be distinguished, as the off-gas can be utilized directly or through the intermediate step of power generation. With regard to the first scenario, depending on the composition of H₂/CO₂ mixture of the off-gas, it could be used in terms as an external CO₂ source for the conversion of H₂ to CH₄. In the second scenario the generated electricity could be subsequently used for electrolysis.

⁸ Report: Vienna University of Technology, 2012. *Overview of lean gas treatment in biogas upgrading systems*. Accessed online: http://bio.methan.at/en/download_leangas

5. Materials & Methods

The subsequent chapters provide information about the applied methods during investigation of the purification process. These methods were of experimental and simulative nature and also interlinked. Findings from experiments served as basis for simulation development as well as for model validation. This chapter is therefore split into three subsections, an experimental part, a simulative part and the validation of the simulation.

5.1 Experimental part

This chapter of the thesis presents the conducted experimental work. First, information about the assembly of several hollow fiber membrane modules with the selected fiber material is presented. This is followed by a description of the procedure how the membrane modules were investigated on a laboratory scale to determine the modules' properties and performances. Furthermore, the design of a small scale pilot plant is shown, which was used for gas purification in connection with a fermenter. Subsequently, information about the applied fermenter setup is presented and followed by a description of the online gas separation examination. The chapter of the experimental part is concluded with details about the applied data reconciliation method, which was used to reconcile the laboratory and field test data.

5.1.1. Assembly of membrane modules

For screening and testing of the membrane material in laboratory, several membrane modules were assembled. The following photo series illustrates selected working steps during assembling of a hollow fiber membrane module. Essential components are i.) the polyimide hollow fibers, ii.) a stainless steel pipe, iii.) Gyrolok[®] TMT tube fittings, and iv.) polyurethane resin UR5562. Furthermore, consumables such as glue, Parafilm[®], cable straps, plastic wrap, and syringes are needed for the potting of the membrane modules. The assembly procedure can be split into two main steps. The first part is the prearrangement of the module and fibers, and the second part is the potting of the end outlets.

5.1.1.1. Prearrangement

The body of the membrane module consists of two Gyrolok[®] TMT tube fittings which are connected via the stainless steel pipe. The fibers are bundled and pulled into the membrane module body. It is important to make sure that the length of the polyimide fibers extends the total length of the module body, which is illustrated in Figure 5.1. This is denoted as the raw structure of the membrane module.

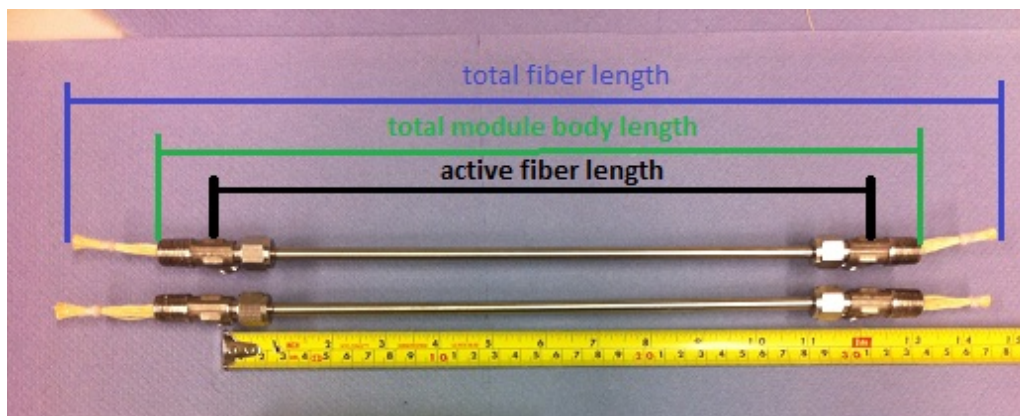


Figure 5.1: Hollow fiber membrane module, with declaration of different length types

Figure 5.1 furthermore shows that the active fiber length is defined as the distance between the center outlets of the two Gyrolok[®] T-pieces. The active fiber length is needed for the calculation of the total membrane area, together with the fiber inner diameter and the number of fibers. The center outlets serve two purposes, as filling spout for the potting during the assembly, and as permeate outlet (or sweep gas inlet) during the practical application of the membrane module.

5.1.1.2. End outlet potting

The potting of the end outlet has the task to seal the volume between the hollow fiber outer surface and the inner surface of the end outlet. Furthermore, the potting needs to withstand pressures up to 20 bar and should be quasi-impermeable to the operated components. A two-part, semi-rigid polyurethane resin was used for the potting, which had met the before mentioned requirements. The fibers were bundled with Parafilm[®] as pictured in Figure 5.2.a. and the respective capillaries subsequently sealed with glue (Figure 5.2.b). Sealing the capillaries was necessary because the resin could get soaked into the fibers by capillary forces due to the resin's low viscosity. The next step was to build a filling bag for the resin. This procedure is pictured in Figure 5.2.c to g, where a piece of plastic wrap was used to generate the filling bag. It was wrapped around the end outlet (Figure 5.2.d), so that a quasi-extension of the end outlet was formed which surrounded the fibers (Figure 5.2.e). Subsequently, the plastic wrap was twisted (Figure 5.2.f) and fixed at the end outlet with a cable strap (Figure 5.2.g). It is important to mention that only one membrane module side a time could be potted. The module was fixed in an upright position as shown in Figure 5.2.h, which made it possible to use the center outlet as filling spout for the resin. Figure 5.2.i pictures the resin pack form, containing resin and hardener.

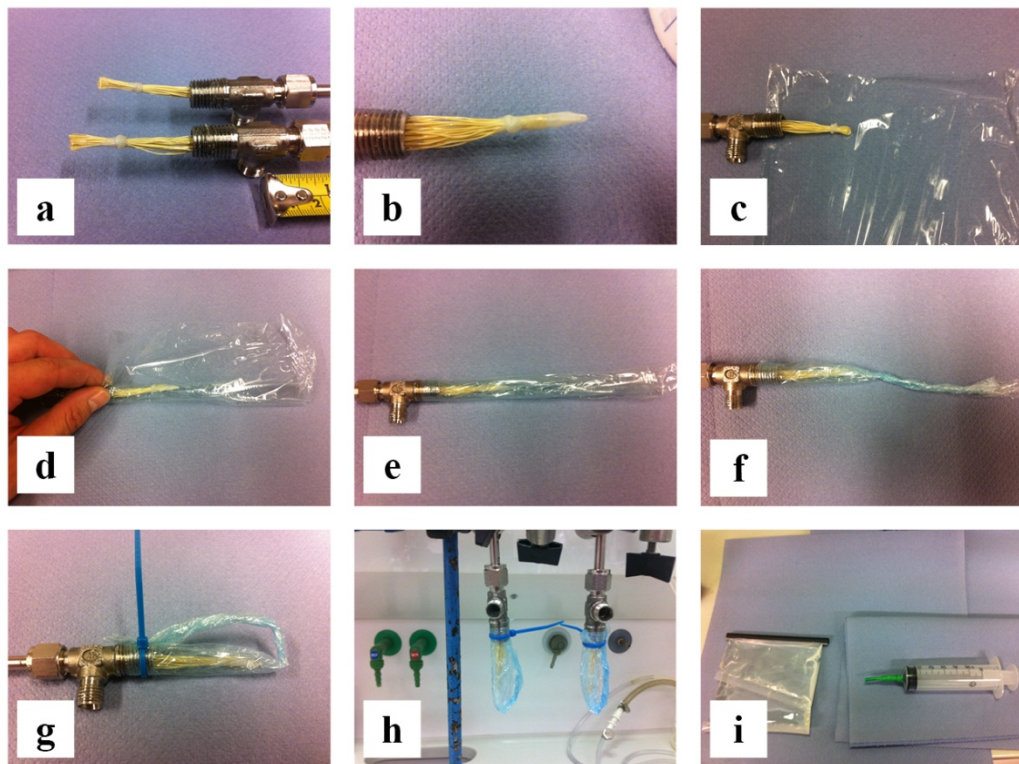


Figure 5.2: Assembly of the membrane modules.

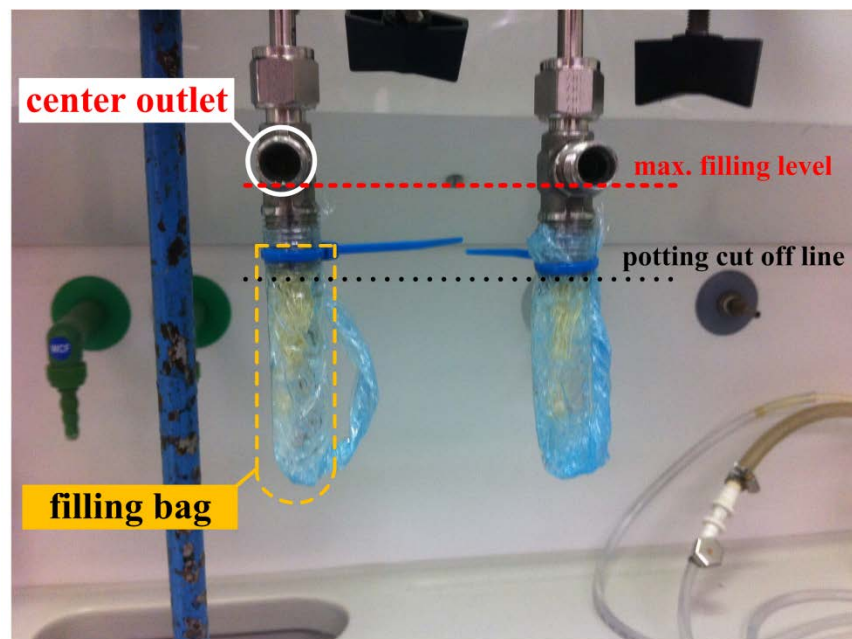


Figure 5.3: Potting of the membrane modules

These two were mixed and by using a syringe the resin was fed into the filling bag until the resin level reached the center outlet. Figure 5.3 shows the filling bag fully filled with resin. After 24 hours the resin was hardened and the potting procedure was repeated on the other side of the membrane module. The last step was to remove the excess potting from the end outlet by cutting it off, exactly at the edge of the end outlet.

The final membrane module needed to undergo a leakage test before it could be further used. This test consisted of i.) visual inspection of the potting, and ii.) shell side pressure testing. In the first part, the potting was inspected for bubbles visually, followed by an inspection of its stiffness. For the pressure test, one of center outlets was locked and nitrogen was applied at slightly elevated pressure via the second center outlet. This test made sure that all fibers were intact. A water film was applied on the fiber pores and if small air bubbles appeared from each fiber pore the module was all right. If this was not the case, the respective fiber pore needed to be sealed with glue.

5.1.1.3. Description of the modules

In total, 4 different modules were built, with the respective properties listed in Table 5.1. The utilized polyimide fibers were provided by the company AXIOM GmbH. Detailed information about the sort of polyimide and polypropylene used in the fibers was not given, as it is part of the commercial and industrial confidentiality.

Table 5.1: Description of the homemade membrane modules with commercial fiber material

ID	Fiber type	Fiber numbers	Active fiber length
M-1	Polyimide (PI)*	35	280 mm
M-2	PI*	35	230 mm
M-3	PI**	35	280 mm
M-4	Polypropylene (PP)***	1	280 mm

* No detailed information about the exact sort of polyimide was provided by the supplier.

** The sort of PI differs from M-1 and M-2.

*** No detailed information about the exact sort of polypropylene was provided.

5.1.2. Material screening and membrane module testing

To determine the membrane module's properties and performance, a laboratory test rig was used. During the test procedure defined operational conditions were applied and the respective transmembrane flow recorded. The membrane module tests were carried out for pure gases and two different gas mixtures. Subsequently, detailed information is presented with respect to the utilized test rig, the pure gas and mixed gas membrane module test procedure.

5.1.2.1. Module testing rig ‘GP2’

The test rig is an adapted version of the experimental setup reported by Makaruk and Harasek [2009]. Figure 5.4 shows a simplified flow sheet of the adapted test rig, namely GP2. The feed gas was adjusted by digital mass flow controllers 5850S provided by Brooks® Instruments. The respective permeate and retentate flows were measured using Definer 220 volume flow meters provided by Bios® International Corporation. Permeate and retentate volume flows were then used to determine the feed stream by indirect measurement as the sum of the two flow rates. The membrane modules were installed in the heating oven Venticell 222R which was supplied by MMM-Group and had the task to provide isothermal conditions. The temperature of the feed gas was measured by a three-wire resistance thermometer purchased from JUMO. The absolute pressure values in permeate and retentate channels were measured using electronic pressure transmitters PTX 1400 from GE Sensing. A proportional valve type 2834, provided by Bürkert, was used to control the retentate pressure. Permeate and retentate gas compositions were recorded using a gas analyzer THERMOR module series GMS800, provided by SICK® AG.

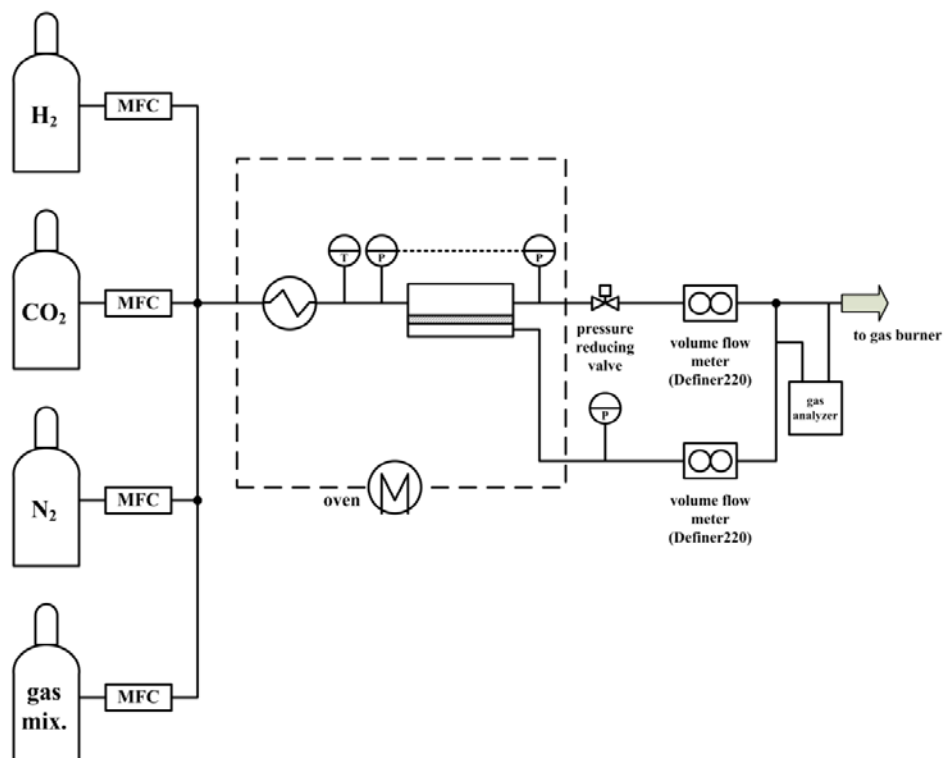


Figure 5.4: Flow sheet of the test rig used for analysis of the membrane modules

Figure 5.5 shows the GP2 membrane test rig, which was controlled via a SPS unit. Mass flow controllers (MFCs), valves, and heater were adjusted on a user interface.

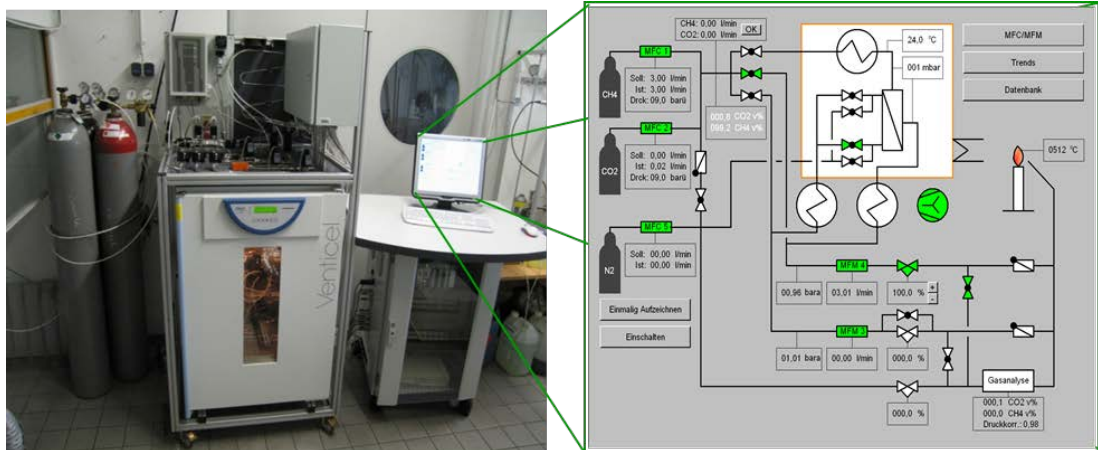


Figure 5.5: Membrane test rig GP2 at the Vienna University of Technology, with a detailed view on the control unit

5.1.2.2. Procedure of pure gas tests

During pure gas tests hydrogen, carbon dioxide, and nitrogen were used under varying conditions. The goal was to determine the permeate flow at different temperature and pressure levels for the respective pure gases H_2 , CO_2 , and N_2 . The permeate pressure for all tests was set as 1.013 bar. Table 5.2 lists the varying parameters for pure gas membrane screening. All pure gas tests were performed in a dead end operational mode to determine the maximum transmembrane flow. The membrane module characteristics derived from the laboratory tests were further used to calculate the ideal selectivity, temperature dependency of the membrane material, and to get information about the optimal operating point. Furthermore, the permeances of the material for the respective pure gases were calculated using the correlation of transmembrane flow, membrane area, and feed to permeate pressure difference in the solution diffusion model (see equation EQ 37 in chapter 5.2.1).

Table 5.2: Parameters for the membrane module pure gas tests

Variation parameters	Unit	Value
Temperature	°C	30
		40
		50
Feed/Permeate pressure difference	bar	2
		3.5
		5
		6.5
		8
		9
		10

At the end of all conducted membrane tests and measurements, including pure and mixed gas laboratory tests as well as field tests, the utilized membrane modules were tested again with pure gases. This had the reason to determine if the utilization under real life conditions for a certain time period had any effect on the membrane module's performance.

5.1.2.3. Procedure of gas mixture tests

The performance of the hollow fiber membrane module was further tested by applying mixed gases. Thereto, a binary and a ternary test gas mixture were provided containing 66 vol% hydrogen, 34 vol% carbon dioxide and 30 vol% hydrogen, 30 vol% carbon dioxide, 40 vol% nitrogen, respectively. Composition and component deviation of the test gases are presented in Table 5.3. The notations 66/34/0 and 30/30/40 refer to the binary and ternary mixtures, with respect to the composition of H₂/CO₂/N₂. These notations are continuously used in the subsequent chapters.

For gas mixture tests membrane modules M-1 and M-2 were chosen and interconnected in a parallel manner to increase the surface area and simultaneously increase the trans-membrane flow. Furthermore, similar conditions as for the pure gas tests were applied. These parameters are listed in Table 5.4. In all mixed gas tests the membrane module was operated in a counter-current mode. The feed flow rate was increased in 30 L_N/h steps from 60 to 180 L_N/h. Furthermore, the pressure difference level was restricted to 8 and 9 bar, as this was seen to be to the optimum operational range. For binary and ternary gases mixtures the transmembrane flow was measured for the given parameters and operational conditions. To determine the gas component specific permeances the obtained data for feed, permeate and retentate volume flows

and compositions were used in the Aspen Plus[®] simulation, which is described in chapter 5.2.3.

Table 5.3: Composition of the test gases applied for membrane testing

Gas mixture	Unit	Value	Deviation
66/34/0			
H ₂	vol%	66.39	0.27
CO ₂		rem.*	-
30/30/40			
H ₂	vol%	30.33	0.21
CO ₂		29.83	0.21
N ₂		rem.*	-

*remaining percentage to 100 vol%

Table 5.4: Parameters for the membrane module mixed gas tests

Variation parameters	Unit	Value
Feed volume flow	L _N /h	60
		90
		120
		150
		180
Temperature	°C	30
		40
		50
Feed/Permeate* pressure difference	bar	8
		9

*permeate pressure is 1.013 bar

If feed gas composition, pressure and ideal selectivity of a binary gas mixture are known, the resulting permeate composition can be calculated according to equation

EQ 6. This approach can be used for a basic mathematical estimation of a separation process based on the solution-diffusion mechanism and steady process conditions.

$$(1 - \alpha_{i,j})x_{P,i}^2 + (\gamma x_{F,i}(\alpha_{i,j} - 1) + \gamma + \alpha_{i,j} - 1)x_{P,i} - \gamma \alpha_{i,j} x_{F,i} = 0 \quad EQ 6$$

In equation *EQ 6*, $\alpha_{i,j}$ is the ideal selectivity of the better permeating component i to the less permeating component j . The character γ is the feed-to-permeate pressure ratio, $x_{F,i}$ is the composition of i in the feed gas stream, and $x_{P,i}$ is the sought permeate gas composition.

A similar approach can be applied for a ternary gas mixture, with the respective components i , j , and h . Provided that the third component h barely permeates through the membrane, the resulting composition in the permeate $x_{P,h}$ can be neglected. To calculate the permeate composition $x_{P,i}$ according to equation *EQ 7* the respective ideal selectivities $\alpha_{i,h}$ and $\alpha_{j,h}$, the feed gas compositions, as well as the feed-to-permeate pressure ratio γ must be given.

$$(\alpha_{j,h} - \alpha_{i,h})x_{P,i}^2 + (\alpha_{i,h}(\gamma x_{F,i} + 1) + \alpha_{j,h}(\gamma x_{F,j} - 1) + \gamma x_{F,h})x_{P,i} - \gamma \alpha_{i,h} x_{F,i} = 0 \quad EQ 7$$

Equations *EQ 6* and *EQ 7* were used for a rough estimation of the purification processes for the binary and ternary gas mixtures.

5.1.3. Small scale pilot plant

To get information about the membranes' applicability they were tested under real-life conditions. Thereto a mobile small scale pilot plant was designed and assembled, which was connected to a fermenter at a later time. The main requirements for the pilot plant were that it was i.) easy to connect to the fermenter, ii.) simple to operate, and iii.) especially designed for the given fermenter size. Table 5.5 lists the presumed composition of the fermentation gas, with a hydrogen content of 66 vol%. Gas composition, gas flow, temperature and pressure values served as basis for the design of the small scale pilot plant.

Table 5.5: Presumed conditions and composition of the fermentation gas for the design of the mobile small scale pilot plant

Fermentation gas	Unit	Value
Volume flow	L _N /h	250 ±50
Pressure	bar	1.013
Temperature	°C	25
Main components		
H ₂	vol%	66 %
CO ₂	vol%	34 %
Trace elements		
Volatile organic components	ppm	none
H ₂ S	ppm	< 600
NH ₃	ppm	< 80

Figure 5.6 pictures the flow sheet of the mobile pilot plant. The design not only includes the necessary membrane module and compressor unit, but also all necessary preliminary purification steps, the process control for the operation of the plant and the ports for gas analysis.

For preliminary purification of the gas, a liquid separator was installed to capture condense water or liquid carryover from fermentation. A gas bag was used as buffer for fluctuations in fermenter gas concentration and flow. For further drying purposes the gas was sent through a first adsorption step with silica gel. A filter was installed to capture particles that could harm the compressor. To compress the fermentation gas to the requested pressure value a double headed two-stage membrane compressor was used. The compressor, supplied by KNF Neuberger GmbH, was designed for a maximum pressure of 12°bara. For security reasons a DWR16 pressure switch and a VNM301 vacuum switch were purchased from Schmachtl GmbH. They were applied to shut down the compressor in case of exceeding or falling below the pressure limits. For further security reasons, a spring-loaded relieve valve type 5 from Niezgodka GmbH was implemented after the compressor. Its purpose was to release pressure and fermentation gas to the atmosphere.

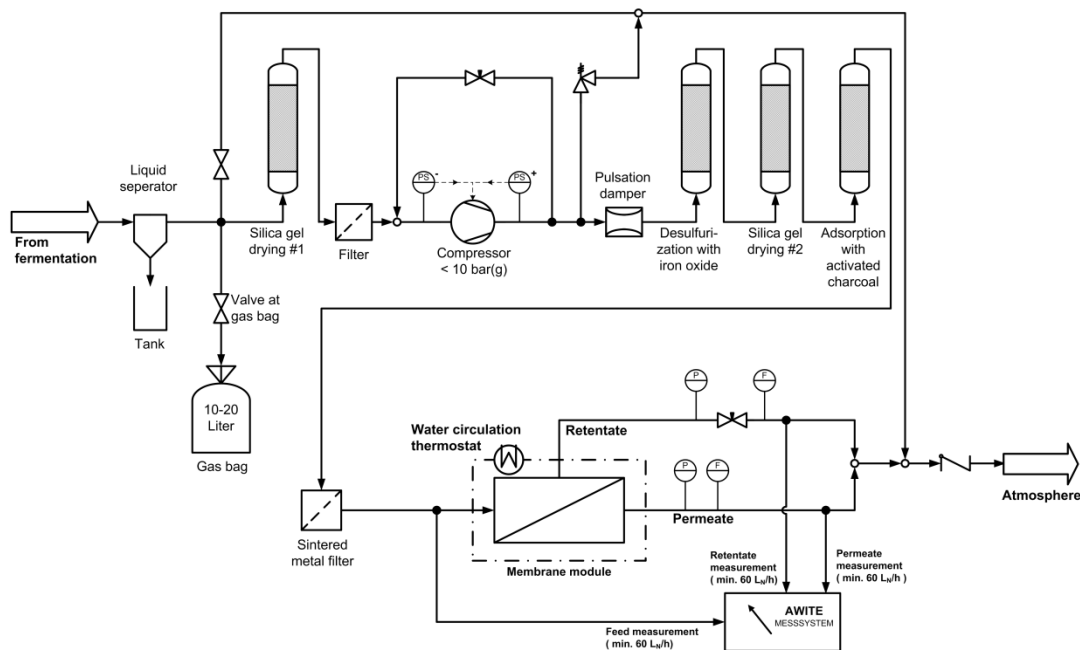


Figure 5.6: Flow sheet of the small scale pilot plant

A pulsation damper was installed to compensate pressure fluctuations from the compressor, before entering the adsorption unit. This unit consisted of three adsorption columns, containing desulfurization with iron oxide, drying with silica gel, and removal of highly volatile organic compounds with activated carbon. The adsorbents were purchased from Merck KGaA. After that, another sintered metal filter was installed to make sure that particles carried away from the adsorption unit don't enter the subsequent hollow fiber membrane module. The membrane model was cooled or heated with a refrigerating circulation chiller supplied by VWR International GmbH, which had an operation range from $-20\text{ }^{\circ}\text{C}$ to $100\text{ }^{\circ}\text{C}$. Volume flow measurements took place for permeate and retentate streams with Definer 220 volume flow meters provided by Bios[®] International Corporation. These volume flow meters are designed to be operated ambient or slightly elevated pressure, which made them unsuitable for feed volume stream measurements. Hence, the feed stream was determined by indirect measurement as the sum of permeate and retentate volume flow. All pressure measurements in the small scale pilot plant were performed with tecsis[®] PEX10 pressure sensors. For temperature recordings tecsis[®] PT-compact sensors were used. Both, pressure and temperature sensors were provided by Schmachtl GmbH.

5.1.4. Fermenter

In the following sub-chapter the applied fermenter system will be described with focus on the design of the fermenter, utilized substrate and bacteria for hydrogen production, as well as the chosen operational conditions. This is followed by a short introduction of the applied gas analysis system.

5.1.4.1. Fermenter design, utilized bacteria and operational conditions

The applied fermenter system was taken from previous work [Foglia et al., 2010a, Foglia et al., 2010b, Foglia et al., 2011] and adapted for the current requirements. Characterized as a 600 L fermenter, this hybrid system with a fluidized bed and trickling filter was designed as a system within a system. The fluidized bed served as a zone mainly for hydrogen production and the trickling filter as a zone where the transition of hydrogen from the liquid to the gas phase was enabled. Based on experience from previous works a saturated product gas containing 65-70 vol% hydrogen, 30-35 vol% carbon dioxide, and traces of acetic acid was expected. Furthermore, thermophilic bacteria were applied to convert the given substrate to hydrogen and carbon dioxide. Molasses was used as substrate, which contains sucrose, glucose and fructose. Table 5.6 presents the respective concentrations in the substrate, which was provided by Agrana Zucker GmbH. Important information about the applied fermentation conditions are listed in Table 5.7.

Table 5.6: Characterization of the utilized substrate

Molasses	Unit	Value
Sucrose	g/L	43.99
Glucose	g/L	6.85
Fructose	g/L	2.09

Table 5.7: Thermophilic fermentation conditions, utilized nutrient salt and inoculum

Conditions	Unit	Value
Substrate concentration	g/L sucrose	10
Temperature	°C	70
pH-value	-	5.5
Nutrient salt	-	K ₂ HPO ₄ , MgCl ₂ , NH ₄ Cl, FeSO ₄
Inoculum		heat-inactivated (105 ° C, 2h) digested sludge of WWTP or of biogas plant

The required nutrient salt solution was presented in an agitated 100 L container, which was freshly prepared in certain intervals. As heat-inactivated inoculum putrefied digested sludge was used, provided by the waste water treatment plant (WWTP) in Asten or by a disposal plant for food waste. Approximately 30 L of inoculum were transferred into the tempered with medium filled fermenter and the fermentation was started in batch mode. Nitrogen was used to inert the system, as wells as in the start-up phase in order to achieve a more rapid stabilization of the system. After an exponential increase in H₂ production, the process was switched to a continuous operational mode. In coordination with the design of the membrane module, the fermentation was planned with a hydrogen production of 165 L/ h and a respective total gas production of 250 L/h. In order to achieve the targeted gas performance a fermentation plan was created, where the organic load was gradually increased. This plan is presented in Table 5.8.

Table 5.8: Plan for the gradually increase of hydraulic retention time during fermentative hydrogen production

HRT	Saccharose	Organic loading Rate (OLR)
in h	in g/L	in g/L/h
20	10	0.50
15	10	0.67
12	10	0.83
10	10	1.00
7.5	10	1.33
5	10	2.00

5.1.4.2. Gas analysis tool AwifLEX®

The AwifLEX gas analysis system, provided by AWITE® Bioenergie GmbH, was used to determine the composition of the fermentation gas (feed), product gas (permeate), and off-gas (retentate). This system was capable of measuring CH₄, CO₂, H₂, and O₂. Methane and carbon dioxide were determined with infrared 2-beam sensors, whilst electrochemical sensors were used for hydrogen and oxygen measurements. The accuracy of infrared and electrochemical sensors was $\pm 2\%$ and $\pm 5\%$ of the measuring range final value, respectively. A measurement cycle consisted of the following main steps, which were repeated for each measuring point: i.) the sample was actively sucked in from the extraction point, ii.) the sample was passed over each sensor in chronological order, iii.) air was passed via the measurement channel to flush the sensors.

5.1.5. Online gas separation with small scale pilot plant

After reaching a stable fermentation, including stable fermentation gas flows and concentrations, the pilot plant was connected to the fermenter for online gas cleaning. By continuously measuring the gas streams and gas composition before and after the gas cleaning system, the cleaning performance of the pilot plant was analyzed under real conditions and thus detailed information on operating data and recoverable gas qualities were obtained. The parameters of hydrogen productivity and hydrogen yield were used to determine the quality of purification. By parameter variation the optimum operating conditions of the gas cleaning system were established, which guaranteed a stable clean product gas stream.

5.1.5.1. Online gas separation field tests

During field tests two membrane modules were selected and inserted into the small scale pilot plant in parallel interconnection to increase the membrane area for the purification task. These membranes were type M-1 and M-2 from chapter 5.1.1.3 with the respective module properties listed in Table 5.1. To determine the purification efficiency a parameter variation was used. Thereto, feed gas flow rate and feed-to-permeate pressure difference were varied. Table 5.9 lists the respective values for the variation parameters. Volume flows of permeate and retentate, as well as concentrations of feed, permeate and retentate were measured for the analysis of the purification system. Additionally to the gas analysis system described in chapter 5.1.4.2, gas chromatography was used as reference measurements. A constant temperature of 30 °C was set for all measurements.

Table 5.9: Parameters for the small scale pilot plant field tests

Variation parameters	Unit	Value
Feed volume flow	L _N /h	60 **
		90 **
		120 **
		150 **
		180 **
Temperature	°C	30
Feed/Permeate* pressure difference	bar	6
		7.5 **
		9 **
		10

* permeate pressure is 1.013 bar

** parameters used for the reference measurements with gas analysis by gas chromatography.

5.1.6. Data Reconciliation with MatLab®

This subsection provides a detailed description of the developed data reconciliation (DR) method, which was used to reconcile all measurements of the membrane gas separation process, including laboratory and field tests. All information presented in the data reconciliation principle section is taken from literature [Narasimhan and Jordache, 1999a, Narasimhan and Jordache, 1999b, Mansour and Ellis, 2008, N.C.S.U and U.O., 2003a, and N.C.S.U and U.O., 2003b].

5.1.6.1. Data reconciliation principle

During the membrane separation measurements, gas flow and composition were simultaneously recorded. For the reconciliation of a system including flow and respective composition, the resulting component mass balances have to be included as constraints. These constraints contain component flow rate terms which are products of the flow rate and composition variables. Since these constraints are nonlinear, it is possible to obtain the solution using a nonlinear DR technique. The following explanations for the DR principle refer to the solution of a steady-state nonlinear DR problem. To handle the nonlinear constraints $f(\hat{\mathbf{y}}, \hat{\mathbf{z}})$ they can be linearized using a first-order Taylor's series. The linearized system of the constraint equations obtained can be written in the form as shown in EQ 8.

$$\mathbf{A}_y \hat{\mathbf{y}} + \mathbf{A}_z \hat{\mathbf{z}} = \mathbf{b} \quad \text{EQ 8}$$

$$\mathbf{A}_y = \left. \frac{\partial f}{\partial \hat{\mathbf{y}}} \right|_{\hat{\mathbf{y}}_i, \hat{\mathbf{z}}_i} = \begin{bmatrix} \frac{\partial f_1}{\partial \hat{y}_1} & \dots & \frac{\partial f_1}{\partial \hat{y}_M} \\ \vdots & \ddots & \vdots \\ \frac{\partial f_C}{\partial \hat{y}_1} & \dots & \frac{\partial f_C}{\partial \hat{y}_M} \end{bmatrix} \text{ at } \hat{\mathbf{y}} = \hat{\mathbf{y}}_i \text{ and } \hat{\mathbf{z}} = \hat{\mathbf{z}}_i \quad \text{EQ 9}$$

$$\mathbf{A}_z = \left. \frac{\partial f}{\partial \hat{\mathbf{z}}} \right|_{\hat{\mathbf{y}}_i, \hat{\mathbf{z}}_i} = \begin{bmatrix} \frac{\partial f_1}{\partial \hat{z}_1} & \dots & \frac{\partial f_1}{\partial \hat{z}_N} \\ \vdots & \ddots & \vdots \\ \frac{\partial f_C}{\partial \hat{z}_1} & \dots & \frac{\partial f_C}{\partial \hat{z}_N} \end{bmatrix} \text{ at } \hat{\mathbf{y}} = \hat{\mathbf{y}}_i \text{ and } \hat{\mathbf{z}} = \hat{\mathbf{z}}_i \quad \text{EQ 10}$$

$$\mathbf{b} = \mathbf{A}_y \hat{\mathbf{y}}_i + \mathbf{A}_z \hat{\mathbf{z}}_i - f(\hat{\mathbf{y}}_i, \hat{\mathbf{z}}_i) \quad \text{EQ 11}$$

The used terms $\hat{\mathbf{y}}, \hat{\mathbf{z}}$ are the vectors of estimates corresponding to measured and unmeasured variables. M is the number of measured variables, N is the number of unmeasured variables, C is the total number of equality constraints, and i is the i^{th} iteration during the successive linearization. The matrices \mathbf{A}_y and \mathbf{A}_z are also known as Jacobian matrices and described in equations EQ 9 and EQ 10. In general, the raw measurements are used as initial estimates for the measured variables in the first iteration. In each iteration step the estimates of the process variables are obtained by minimizing EQ 12, which is subject to EQ 13.

$$\text{Minimizing } J(\hat{\mathbf{y}}, \hat{\mathbf{z}}) = (\mathbf{y} - \hat{\mathbf{y}})^T \mathbf{V}^{-1} (\mathbf{y} - \hat{\mathbf{y}}) \quad \text{EQ 12}$$

$$\text{Subject to } \mathbf{A}_y \hat{\mathbf{y}} + \mathbf{A}_z \hat{\mathbf{z}} = \mathbf{b} \quad \text{EQ 13}$$

In EQ 12 the vector \mathbf{y} is defined as an $M \times 1$ vector of the raw measurements for M process variables. The respective vector $\hat{\mathbf{y}}$ is an $M \times 1$ vector of estimates (reconciled values) for the M process variables, and the vector $\hat{\mathbf{z}}$ is an $N \times 1$ vector of estimates for unmeasured process variables, described as vector \mathbf{z} . In equations EQ 12 and EQ 14 the matrix \mathbf{V} is defined as an $M \times M$ covariance matrix of the measurements.

To solve the linear DR problem, the Q-R factorization of \mathbf{A}_z can be applied to eliminate the unmeasured variables $\hat{\mathbf{z}}$. With $\mathbf{Q}_1, \mathbf{Q}_2, \mathbf{R}_1,$ and \mathbf{R}_2 as the respective submatrices from the Q-R factorization, the problem becomes:

$$\text{Minimizing } J(\hat{\mathbf{y}}, \hat{\mathbf{z}}) = (\mathbf{y} - \hat{\mathbf{y}})^T \mathbf{V}^{-1} (\mathbf{y} - \hat{\mathbf{y}}) \quad \text{EQ 14}$$

$$\text{Subject to } \mathbf{Q}_2^T \mathbf{A}_y \hat{\mathbf{y}} = \mathbf{Q}_2^T \mathbf{b} \quad \text{EQ 15}$$

In equation EQ 15 the matrix \mathbf{Q}_2^T is defined as the projection matrix. The solution for the measured variables in the steady-state reconciliation problem can then be written as given in equation EQ 16.

$$\hat{\mathbf{y}} = \mathbf{y} - \mathbf{V}(\mathbf{Q}_2^T \mathbf{A}_y)^T \left[(\mathbf{Q}_2^T \mathbf{A}_y) \mathbf{V} (\mathbf{Q}_2^T \mathbf{A}_y)^T \right]^{-1} (\mathbf{Q}_2^T \mathbf{A}_y \mathbf{y} - \mathbf{Q}_2^T \mathbf{b}) \quad \text{EQ 16}$$

For the unmeasured variables the solution is given in equation EQ 17.

$$\hat{\mathbf{z}} = \mathbf{R}_1^{-1} \mathbf{Q}_1^T \mathbf{b} - \mathbf{R}_1^{-1} \mathbf{Q}_1^T \mathbf{A}_y \hat{\mathbf{y}} - \mathbf{R}_1^{-1} \mathbf{R}_2 \mathbf{z}_{N-r} \quad \text{EQ 17}$$

These results are the new estimates for measured and unmeasured variables of iteration step 1, and the next iteration step begins. The iteration continues until a certain tolerance criterion \mathbf{K} is satisfied, which is presented in EQ 18.

$$\|\hat{\mathbf{y}}(\mathbf{n}) - \hat{\mathbf{y}}(\mathbf{n} - 1)\| < \mathbf{K} \quad \text{and} \quad \|\hat{\mathbf{z}}(\mathbf{n}) - \hat{\mathbf{z}}(\mathbf{n} - 1)\| < \mathbf{K} \quad \text{EQ 18}$$

5.1.6.2. Data reconciliation for membrane module measurements

The DR system for the reconciliation of the laboratory and field measurements was designed and programmed in MatLab[®] from The MathWorks, Inc. (Version R2013a). It was necessary to reconcile the data to close the overall material balance of the measurements. The utilization of MatLab[®] allowed processing a variety of data sets in a short period of time. Subsequently, the DR principle from chapter 5.1.6.1 is applied for the present case of a membrane gas separation unit, particularly the laboratory measurements with the 40/30/30 test gas mixture. Figure 5.7 pictures a simplified scheme of the measurement setup including measured and unmeasured variables.

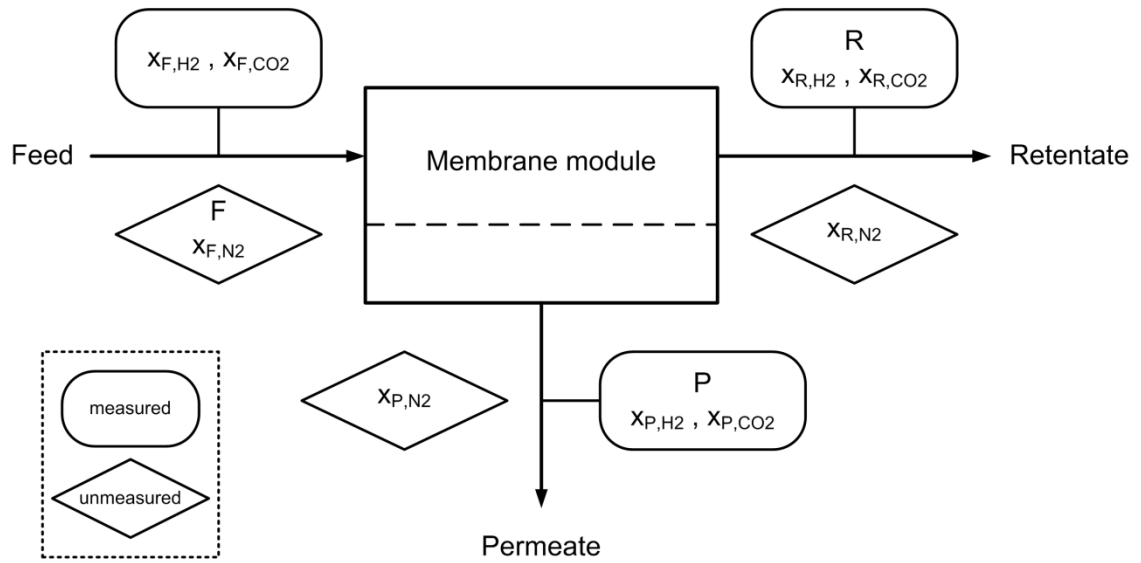


Figure 5.7: Declaration of measured and unmeasured values for DR

The feed volume flow was an unmeasured variable, but was calculated as the sum of permeate and retentate volume flow. Furthermore, the nitrogen composition in feed, permeate and retentate were unmeasured variables, because the gas analytic could not detect them. These values were determined by the difference between the sum of hydrogen and carbon dioxide composition and 100% in the respective stream composition.

Table 5.10: Measured and unmeasured variables for data reconciliation problem of the membrane measurements

Measured variables		Unmeasured variables	
x_{F,H_2}	H ₂ content in Feed	F	Feed flow
x_{F,CO_2}	CO ₂ content in Feed	x_{F,N_2}	H ₂ content in Feed
R	Retentate flow	x_{R,N_2}	N ₂ content in Retentate
x_{R,H_2}	H ₂ content in Retentate	x_{P,N_2}	N ₂ content in Permeate
x_{R,CO_2}	CO ₂ content in Retentate		
P	Permeate flow		
x_{P,H_2}	H ₂ content in Permeate		
x_{P,CO_2}	CO ₂ content in Permeate		

Unmeasured and measured variables are presented in Table 5.10, including their exact designation. These variables were used to form the respective vectors \mathbf{y} and \mathbf{z} from chapter 5.1.6.1, which are presented in equations EQ 19 and EQ 20. These vectors also represent the assigned variables used in the principle as well as in the MatLab[®] code.

$$\mathbf{y} = \begin{bmatrix} y_1 \\ y_2 \\ y_3 \\ y_4 \\ y_5 \\ y_6 \\ y_7 \\ y_8 \end{bmatrix} = \begin{bmatrix} P \\ R \\ x_{F,H2} \\ x_{F,CO2} \\ x_{P,H2} \\ x_{P,CO2} \\ x_{R,H2} \\ x_{R,CO2} \end{bmatrix} \quad \text{EQ 19}$$

$$\mathbf{z} = \begin{bmatrix} z_1 \\ z_2 \\ z_3 \\ z_4 \end{bmatrix} = \begin{bmatrix} F \\ x_{F,N2} \\ x_{P,N2} \\ x_{R,N2} \end{bmatrix} \quad \text{EQ 20}$$

Furthermore, the absolute deviations of the utilized measurement equipment are listed in Table 5.11. The deviations were needed to form the co-variance matrix \mathbf{V} which is shown in EQ 21 and also appears in equations EQ 12, EQ 14, and EQ 16.

$$\mathbf{V} = \text{diag} [(y_1 * 0.01)^2, (y_2 * 0.01)^2, (y_3 * 0.00407)^2, \\ (y_4 * 0.00803)^2, (y_5 * 0.01)^2, (y_6 * 0.01)^2, \\ (y_7 * 0.01)^2, (y_8 * 0.01)^2] \quad \text{EQ 21}$$

For the presented reconciliation task a test gas cylinder provided the feed gas, whilst the SICK gas analysis tool was used to determine the respective gas compositions of permeate and retentate. Table 5.11 inter alia lists the test gas cylinder composition with respective deviations.

Table 5.11: Deviations given for the utilized measuring equipment

Apparatus		Rel. deviation
Definer 220	Volume flow	1 %
SICK	Volume fraction	
CO ₂	0 – 100 vol%	1 %
H ₂	0 – 100 vol%	1 %
AWITE	Volume fraction	
CO ₂	0 – 100 vol%	0.2 % ^{1.)}
H ₂	3 – 15 vol%	0.2 % ^{1.)}
	15 – 100 vol%	0.7 % ^{1.)}
Test gas	Volume fraction	
CO ₂	30.33 vol%	0.407 %
H ₂	29.83 vol%	0.803 %

^{1.)} relative value of actual reading.

For the solution of the DR minimization problem the non-linear constraints were determined. Thereto, component balances and normalization equations were established. Component balances for hydrogen, carbon dioxide and nitrogen are presented in equations EQ 22 to EQ 27. For both, component balances and normalization equations, the upper row shows the respective equation based on measurement terms, whilst the lower row presents the equation using the assigned variables in the principle and in the MatLab[®] code.

$$\text{H}_2: \quad F * x_{F,H2} - P * x_{P,H2} - R * x_{R,H2} = 0 \quad \text{EQ 22}$$

$$z_1 * y_3 - y_1 * y_5 - y_2 * y_7 = 0 \quad \text{EQ 23}$$

$$\text{CO}_2: \quad F * x_{F,CO2} - P * x_{P,CO2} - R * x_{R,CO2} = 0 \quad \text{EQ 24}$$

$$z_1 * y_4 - y_1 * y_6 - y_2 * y_8 = 0 \quad \text{EQ 25}$$

$$\text{N}_2: \quad F * x_{F,N2} - P * x_{P,N2} - R * x_{R,N2} = 0 \quad \text{EQ 26}$$

$$z_1 * z_2 - y_1 * z_3 - y_2 * z_4 = 0 \quad \text{EQ 27}$$

$$\text{Feed:} \quad x_{F,H2} + x_{F,CO2} + x_{F,N2} - 1 = 0 \quad \text{EQ 28}$$

$$y_3 + y_4 + z_2 - 1 = 0 \quad \text{EQ 29}$$

$$\text{Permeate:} \quad x_{P,H2} + x_{P,CO2} + x_{P,N2} - 1 = 0 \quad \text{EQ 30}$$

$$y_5 + y_6 + z_3 - 1 = 0 \quad EQ 31$$

Retentate:

$$x_{R,H2} + x_{R,CO2} + x_{R,N2} - 1 = 0 \quad EQ 32$$

$$y_7 + y_8 + z_4 - 1 = 0 \quad EQ 33$$

These non-linear constraints are defined as $f(\hat{y}_i, \hat{z}_i)$ and were used to identify the corresponding Jacobian matrices \mathbf{A}_y and \mathbf{A}_z . Equations EQ 34 and EQ 35 show the respective matrices.

$$\mathbf{A}_y = \left. \frac{\partial f}{\partial \hat{y}} \right|_{\hat{y}_i, \hat{z}_i} = \begin{bmatrix} -y_5 & -y_7 & z_1 & 0 & -y_1 & 0 & -y_2 & 0 \\ -y_6 & -y_8 & 0 & z_1 & 0 & -y_1 & 0 & -y_2 \\ -z_3 & -z_4 & 0 & 0 & 0 & 0 & 0 & 0 \\ 0 & 0 & 1 & 1 & 0 & 0 & 0 & 0 \\ 0 & 0 & 0 & 0 & 1 & 1 & 0 & 0 \\ 0 & 0 & 0 & 0 & 0 & 0 & 1 & 1 \end{bmatrix} \quad EQ 34$$

$$\mathbf{A}_z = \left. \frac{\partial f}{\partial \hat{z}} \right|_{\hat{y}_i, \hat{z}_i} = \begin{bmatrix} y_3 & 0 & 0 & 0 \\ y_4 & 0 & 0 & 0 \\ z_2 & z_1 & y_1 & y_2 \\ 0 & 1 & 0 & 0 \\ 0 & 0 & 1 & 0 \\ 0 & 0 & 0 & 1 \end{bmatrix} \quad EQ 35$$

Term \mathbf{b} from the linearized system in EQ 8 was determined by using the Jacobian matrices and the constraints $f(\hat{y}_i, \hat{z}_i)$ in that exact equation. The next step was the Q-R factorization of \mathbf{A}_z , which was accomplished with the MatLab[®] command $[Q,R] = \text{qr}(A_z)$. As a result all required terms are available to solve equations EQ 16 and EQ 17 to calculate the new estimates for measured and unmeasured variables. The iteration continued until the tolerance criterion \mathbf{K} reached a value lower 1×10^{-10} .

5.2 Simulative part

For the simulative investigation of the gas purification process a single-stage unit operation was designed with the simulation software Aspen Custom Modeler[®]. This model simulates the occurring separation mechanism in the membrane, also known as gas permeation. For better understanding of the gas separation process the principles of gas permeation are discussed, focusing on the transport through dense membranes. Subsequently, information about the utilized simulation software is presented followed by a detailed explanation of the single-stage module's design. The chapter is concluded with a description of the investigated multi-stage process setups and the applied membrane area variation.

5.2.1. Principles of Gas Permeation

As the gas transport mechanism of a dense membrane can be described by the solution-diffusion model, the following section will simply focus on this mechanism. Information about different transport theorems can be found in literature [Baker, 2012].

5.2.1.1. Gas transport in dense membranes

The mathematical basis of the solution-diffusion model is outlined by the qualitative description of permeation using phenomenological equations, particularly Fick's law [Baker, 2012]. The model derives from the work of Wijmans and Baker [1995] and was first postulated by Graham [1863]. Generally, the mechanism can be divided into three main steps. These are sorption of the penetrants at the feed side, diffusion across the membrane, and desorption at the permeate side [Shao et al., 2009]. For the transport through a dense membrane the mechanism can be expressed by equation EQ 36 [Baker, 2012]:

$$J_i = -D_i \frac{dc_i}{dx} \quad \text{EQ 36}$$

For the separation of gaseous mixtures, it has to be considered that a higher pressure $p_{i,0}$ is applied at the feed side of the membrane, and a lower pressure $p_{i,l}$ at permeate side. There is an interaction between a compressible fluid and an incompressible medium at the gas/membrane interface. This leads to the definition of the (Henry's Law) gas phase sorption coefficient K_i for every component i of the gas mixture, which is a parameter for the number of molecules in the membrane material. It also depicts the relationship between partial pressure p_i and concentration c_i . The pressure difference between the feed side and the permeate side generates a chemical potential gradient, which is the driving force for separation.

For solution-diffusion the mass-transport through a membrane can be described as:

$$J_i = \frac{D_i K_i (p_{i,0} - p_{i,l})}{l} \quad EQ 37$$

with D_i as the diffusion coefficient, which describes the mobility of the molecules in the membrane material and l as the thickness of the selective layer. The product $D_i K_i$ is known as the permeability coefficient P_i , a parameter that describes the membrane's ability to permeate gas [Baker, 2012]. Dividing the permeability coefficient through the selective layer thickness ($\frac{P_i}{l}$), results in the permeance Π_i . The permeance is often given in a unit entited as gpu ($1 \text{ gpu} = 1 \times 10^6 \text{ cm}^3_{(\text{STP})} \cdot \text{cm}^{-2} \cdot \text{s}^{-1} \cdot \text{cmHg}^{-1}$). Additionally to gpu the unit $\text{m}^3_{(\text{STP})} \cdot \text{m}^{-2} \cdot \text{s}^{-1} \cdot \text{bar}^{-1}$ ($1 \text{ m}^3_{(\text{STP})} \cdot \text{m}^{-2} \cdot \text{s}^{-1} \cdot \text{bar}^{-1} = 1.333 \times 10^6 \text{ gpu}$) is used in this work. The membrane flux J_i is a mass flux, but can easily be transformed into a molar or volume based form, as Wijmans and Baker [1995] show.

Another parameter for characterizing a membrane material is the ideal membrane selectivity α_{ij} . This parameter reflects the membrane's ability to separate two gases, with i and j referring to the better, respectively less permeating component.

$$\alpha_{i,j} = \left[\frac{D_i}{D_j} \right] \left[\frac{K_i}{K_j} \right] = \frac{\Pi_i}{\Pi_j} \quad EQ 38$$

The ratio D_i/D_j is denoted as the mobility selectivity, and K_i/K_j as the solubility selectivity. The former reflects the different sizes of the two molecules and the latter the relative condensability of the two components. The ideal selectivity can also be described by the ratio of pure-gas permeances or permeabilities, as shown in equation EQ 38. The permeability of a membrane material is generally expressed in a unit called Barrer ($1 \text{ Barrer} = 10^{-10} \text{ cm}^3(\text{STP}) \cdot \text{cm} \cdot \text{cm}^{-2} \cdot \text{s}^{-1} \cdot \text{cmHg}^{-1}$).

Transmembrane flow and selectivity are two factors commonly used to describe the performance of a membrane gas separation system. Another factor is the membrane stage cut θ , defined as the quotient of permeate flow and feed flow.

$$\theta = \frac{\dot{n}_{\text{Permeate}}}{\dot{n}_{\text{Feed}}} \quad EQ 39$$

5.2.1.2. Temperature dependency

The operating temperature can have a severe influence on the permeability or permeance. Usually, this type of dependency is described via the Arrhenius equation, which is seen as an empirical relationship and stated in equation EQ 40.

$$P_i = P_{i,0} e^{-\frac{E_p}{RT}} \quad \text{EQ 40}$$

In this equation $P_{i,0}$ is a pre-exponential factor that describes the permeability at infinite temperature, R is the universal gas constant and T is the temperature. The term E_p is the activation energy of permeation which is defined as the sum of activation energy of diffusion E_D and partial molar enthalpy of sorption ΔH_K . This shows that the temperature's influence on permeability is a combination of the thermal effects on diffusion and solubility. For both parameters the temperature dependency can be described via an Arrhenius type expression, when associated with solubility better known as the van't Hoff relationship [Duthie et al., 2007]. In glassy polymers E_D is always positive whilst ΔH_K is negative and as a result, when the temperature is increased the diffusion coefficient increases and the solubility coefficient decreases [David et al., 2011].

A linear regression of the Arrhenius equation can be used to calculate the specific parameters $P_{i,0}$ and E_p . Hence, it has to be taken into account that its application is only valid in a temperature range where no significant thermal transition in the polymer is caused. This upper bond is also known as the glass transition temperature, at which the penetrant concentration in the polymer is reached that induces glass transition in the polymer.

5.2.1.3. Concentration polarization and plasticization

Concentration polarization refers to a concentration gradient arising in a boundary layer adjacent to the membrane wall which occurs due to depletion of a more permeable component and a resulting accumulation of less permeable components [Wang et al., 2002]. This effect can be strengthened due to low mixing capacities and low gas velocities at the membrane surface as a result of the velocity boundary layer. According to Lüdtkke et al. [1998] it is usually assumed that the effects of concentration polarization can be neglected in gas permeation. But this assumption may only be applied for membranes with low permeation rates and respective gas permeances under 100 gpu (equals $7.5 \times 10^{-5} \text{ m}^3_{(\text{STP})} \cdot \text{m}^{-2} \cdot \text{s}^{-1} \cdot \text{bar}^{-1}$) [He et al., 1999, Mourgues and Sanchez, 2005]. At higher gas permeances a negative influence of concentration polarization on the separation process is clearly evident and needs to be taken into account. He et al.

[1999] found that the permeation rate is the dominating factor, but increasing feed gas velocity results in a decrease in concentration polarization. Therefore, applying higher feed flow rates is a typically used method to reduce the effect of concentration polarization. In contrary, when lowering the feed flow rate the stage-cut increases and consequentially the effect of concentration polarization becomes more severe [Ramírez-Morales et al., 2013]. With respect to the operational conditions, the effects of concentration polarization can have a severe influence on an accurate estimation of the membrane performance and therefore need to be considered. Additional effects such as temperature polarization, solubility coupling and plasticization may worsen the separation performance and enhance the concentration polarization. A fast and exact prediction of all actually arising effects is not possible, because an accurate simulation of the occurring concentration and flow rate gradients requires the solution of a set of complicated differential mass and heat transfer equations. But several simplified models have been published, either based on a multi-resistances model where various boundary layers are described by different resistances or based on the ‘dual-mode sorption partial immobilization’ theory [Lüdtke et al., 1998, He et al., 1999, Mourgues and Sanchez, 2005, Zhang et al., 2006, David et al., 2011]. Figure 5.8 pictures the basic principle of a multi-resistance model for a hollow fiber membrane, with respect to the change of concentration gradient across the membrane.

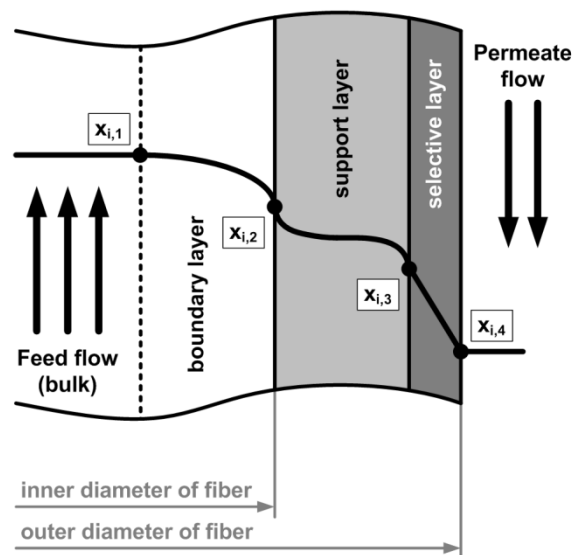


Figure 5.8: Sample scheme for the multi-resistance model considering a hollow fiber membrane

Due to concentration polarization an enrichment of the less permeable components in the boundary layer occurs. As a result the concentration of the better

permeable component is reduced from bulk concentration $x_{i,1}$ to a certain value $x_{i,2}$ at the membrane inner wall. It is apparent that the actual driving force for the trans-membrane flow is reduced because the concentration $x_{i,2}$ is the decisive value that needs to be used for the calculation of the concentration difference to $x_{i,4}$, not concentration $x_{i,1}$ as generally assumed. Depending on the structure of the hollow fiber membrane the separation layer may consist of two different phases, a support layer and a selective layer. The sample scheme in Figure 5.8 pictures this concept, where different transport resistances in the different layers take place. The overall transfer from the inside of the separation layer to the outside is based on the solution-diffusion mechanism, but swelling of the structure, solubility coupling, and free volume theory of diffusion can have a severe effects on it. The swelling relates to plasticization which, according to David et al. [2011], is a result of some certain penetrants that sorb into the polymer to such an extent that chain mobility and chain spacing in the polymer increase. The higher mobility in polymer chains is often interpreted as more void space [Duthie et al., 2007]. This increase in chain mobility can be observed by a minimum in the course of the glass-transition temperature of the polymer-penetrant mixture [Bos et al., 1999]. A typical penetrant that causes plasticization in polymer membranes is carbon dioxide. When a certain CO_2 concentration in the polymer is reached it causes the before mentioned increase in free volume and segmental mobility [Bos et al., 1999]. For the task of H_2/CO_2 separation, this means a loss in selectivity because not only the CO_2 permeability increases due to plasticization but also the permeability of all other gases [Scholes et al., 2010]. In general, the concentration dependence of solubility in glassy polymers can be described via the dual mode sorption model [Robeson, 1991, Duthie et al., 2007, Kanehashi et al., 2007]. In this model, the concentration of a gas in the polymeric membrane is described as presented in equation EQ 41.

$$c_M = k_D p + \frac{c'_H b p}{1 + b p} \quad \text{EQ 41}$$

Here, k_D is the Henry's constant, p is the pressure at the membrane, and c'_H is the Langmuir capacity constant which represents the concentration of molecules in micro voids at saturation conditions. The variable b is the Langmuir affinity constant which characterizes the tendency of a given penetrant to sorb according to the Langmuir approach. In the dual mode sorption model, the glassy polymer is seen to have two sites where sorption takes place, Henry and Langmuir sites respectively [David et al., 2011]. The first part in equation EQ 41 relates to the Henry's law dissolution, where the gas dissolves into the free volume between adjacent polymer chains. The second part refers to the Langmuir site and corresponds to the dissolved population in the excess free volume of the polymer [David et al., 2011]. According to the measurement data collected by Bos et al. [1999], the permeability decreases with increasing pressure until

a certain point where this trend is then reversed. The applied pressure at this turning point in permeability is referred to as plasticization pressure [Duthie et al., 2007]. Although the plasticization pressure differs for various polymers, it appears to correlate with a constant concentration of CO₂ in it [Bos et al., 1999, Wind et al., 2003]. Furthermore, effects and degree of plasticization are known to dependent on the polymer thickness [Duthie et al., 2007]. The extent of plasticization relates to the cohesiveness of the membrane structure and for can be reduced by cross-linking of the membrane chains and/or thermal annealing [Wind et al., 2003]. It is proven that covalent cross-linking tends to concurrently increase selectivity but reduce permeability [Scholes et al., 2010].

As the permeances in this work are below 100 gpu, the extent of the concentration polarization effect is seen to be negligible and is therefore not implemented into the simulation model in chapter 5.2.3.

5.2.1.4. Pressure drop in hollow fiber membranes

Depending on operational mode of a hollow fiber membrane module a pressure drop can occur either on the permeate side for shell-side feed or on the retentate side for poor-side feed. The Hagen-Poiseuille law was used because it is an eligible equation to determine the pressure drop in a long cylindrical pipe with constant cross-section, such as present in a hollow fiber [Tessendorf et al., 1999, Wang et al., 2002, Shao and Huang, 2006, Murad Chowdhury et al., 2005]. The applied Hagen-Poiseuille equation for a fluid in a hollow fiber [Wang et al., 2002] is presented in equation EQ 42.

$$\frac{dp}{dl} = \frac{128 \mu R T \dot{v}_{Fiber}}{\pi N p_{Fiber} d_i^4} \quad EQ 42$$

In equation EQ 42, μ is the dynamic viscosity of the gas, R is the gas constant, T is the operating temperature, \dot{n}_p is the volume flow in the fiber, N is the number of fibers, p is the pressure in the fiber, and d_i is the fiber inner diameter. The presented equation is a good first approach to determine the progress in pressure drop along a hollow fiber, even though it is only true for an incompressible fluid.

5.2.2. Simulation software (ACM, Aspen Plus)

For the development of gas permeation simulation unit, the modeling tool Aspen Custom Modeler[®] (ACM, V7.3, Aspen Technology, Inc., Burlington, USA, 2011) is utilized. The ACM uses an object-oriented modelling language and can be customized for different approaches. For a successful development of a model in ACM, equations, variables, integer, and real parameters are implemented. If the system of equations and

variables converges, the model can be already used directly for calculations. Another possibility is to export it into the Aspen Plus[®] Model Library and use it as a unit operation in a process flow sheet. The simulation program Aspen Plus[®] (V7.3.2, Aspen Technology, Inc., Burlington, USA, 2013) solves the mass and energy balances, with components and physical properties obtained from the Aspen Plus component database.

5.2.3. Single-stage module

The single stage module is designed in to different manners, i) a base case, and ii) a detailed case. In the detailed case, specific information about the membrane module like fiber number, length and diameter need to be provided. Compared to that, the base case only requires the total surface area. For both module designs, simulations with a counter-current and a co-current operational mode were developed. Figure 5.9 shows the underlying model routine, valid for all ACM models.

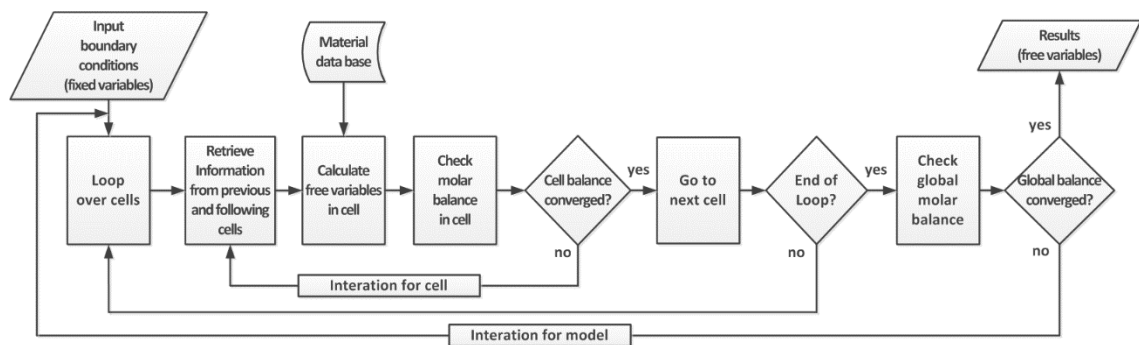


Figure 5.9: Scheme of the model routine for the ACM models

In the subsequent chapters the counter-current designs for base and detailed case are described in detail, followed by information about differences in the develop co-current unit operations.

5.2.3.1. ACM base case model: Counter-current operational mode

The ACM gas permeation model utilized in this project was based on the work from Rodrigues [2009], Rom et al. [2014], and Makaruk and Harasek [2009]. Same as for the underlying work, the transport theorem considered the solution-diffusion mechanism, as it is described in the theoretical background section. The model represents a hollow fiber membrane module with bore side feed, operated in a counter-current arrangement. It was assumed, that the effects from temperature gradients and membrane's geometry were negligible. Furthermore, temperature as well as total pressure on the feed and permeate side was constant. The latter means that the pressure drop from feed inlet to retentate outlet due to pipe flow was neglected.

Table 5.12. Input parameters for the ACM models

Name	Unit	Parameter
Membrane Area	m ²	Area
Number of Cells	-	N _{Cells}
Temperature	°C	T
Feed flow	kmol/h	n _{Feed}
Feed composition	kmol/kmol	y _{Feed}
Feed pressure	bar	p _{Feed}
Permeate pressure	bar	p _{Permeate}
Permeance of each component	Nm ³ /(m ² .s.bar)	Π _{i,vol}

Also, each component's permeance was constant and considered as independent of different partial pressures. As Figure 5.10 shows, the membrane area was divided into k cells (Parameter NCells) of equal size. The respective input parameters are listed in Table 5.12.

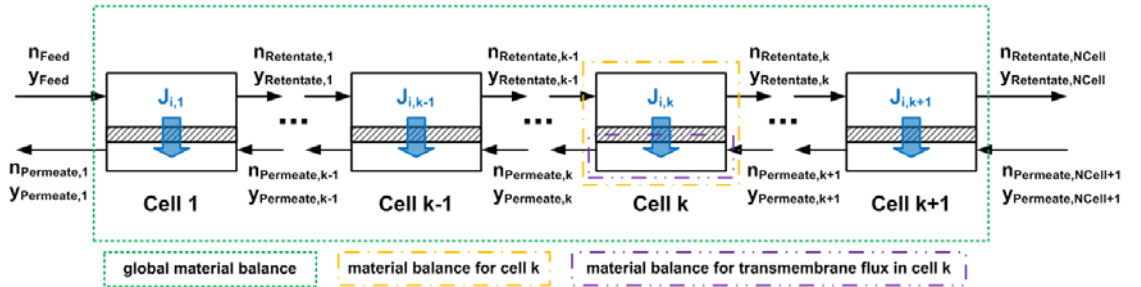


Figure 5.10. Example graph of the countercurrent model

The main balance equations for global molar mass balance (EQ 43), cell molar mass balance (EQ 44) and area specific transmembrane flux for component i in each cell (EQ 45, EQ 46) are as following:

$$\dot{n}_{Permeate,0} + \dot{n}_{Retentate,N_{Cells}} = \dot{n}_{Feed,0} + \dot{n}_{Permeate,N_{Cells}+1} \quad EQ 43$$

$$\dot{n}_{Permeate,k+1} + \dot{n}_{Retentate,k-1} = \dot{n}_{Permeate,k} + \dot{n}_{Retentate,k} \quad EQ 44$$

$$J_{i,k}^{A,mol} = \Pi_{i,k}(p_{i,Retentate,k} - p_{i,Permeate,k}) \quad EQ 45$$

$$J_{i,k}^{A,mol} = \frac{\dot{n}_{Permeate,k} y_{Permeate,k} - \dot{n}_{Permeate,k+1} y_{Permeate,k+1}}{A_{Cell}} \quad EQ 46$$

In equations *EQ 45* and *EQ 46*, the trans-membrane flux $J_{i,k}^{A,mol}$ was defined as an area-specific flux, which was on a molar basis. The respective area was specified as the membrane area of a single cell A_{Cell} , which was the ratio of total membrane area and number of cells. The variable $\Pi_{i,k}$ in equation *EQ 45* was defined as the permeance of component i in cell k . Furthermore, the partial pressure of component i for retentate and permeate flows were used as the driving force for the transmembrane flow in cell k .

5.2.3.2. ACM base case model: Co-current operational mode

The input parameters and assumptions of the co-current operational mode were similar to the ones used in counter-current simulation. Figure 5.11 shows the principle of the co-current operational mode.

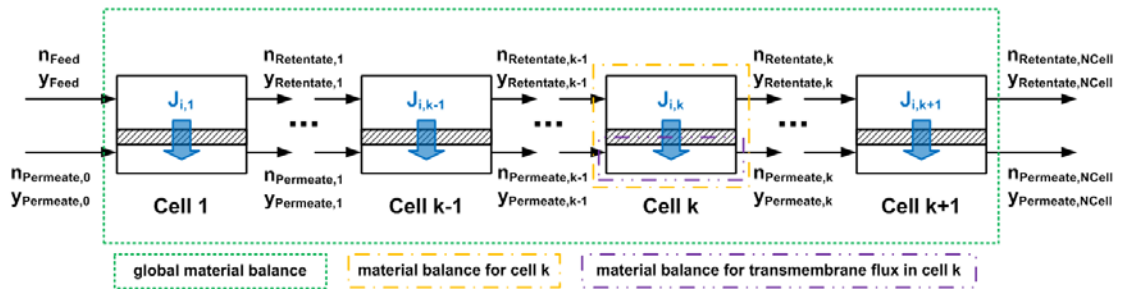


Figure 5.11: Example graph of the co-current model

Equations *EQ 47* and *EQ 48* present the global material balance and the material balance for cell k , respectively. In equation *EQ 49* the relation between transmembrane flow, permeance and pressure difference is shown. Equation *EQ 50* displays the material balance on the permeate side of the membrane for calculation of the transmembrane flux.

$$\dot{n}_{Permeate,N_{Cells}} + \dot{n}_{Retentate,N_{Cells}} = \dot{n}_{Feed,0} + \dot{n}_{Permeate,0} \quad EQ 47$$

$$\dot{n}_{Permeate,k} + \dot{n}_{Retentate,k} = \dot{n}_{Permeate,k-1} + \dot{n}_{Retentate,k-1} \quad EQ 48$$

$$J_{i,k}^{A,mol} = \Pi_{i,k} \left(\frac{(p_{i,Retentate,k-1} + p_{i,Retentate,k})}{2} - \frac{(p_{i,Permeate,k-1} + p_{i,Permeate,k})}{2} \right) \quad EQ\ 49$$

$$J_{i,k}^{A,mol} = \frac{\dot{n}_{Permeate,k} Y_{Permeate,k} - \dot{n}_{Permeate,k-1} Y_{Permeate,k-1}}{A_{Cell}} \quad EQ\ 50$$

5.2.3.3. Comparison of the counter-current and co-current operational mode

To determine the better fitting operational mode a sensitivity analysis was conducted in Aspen Plus® with varying feed flow. Both feed gas mixtures, binary (66/34/0) and ternary (30/30/40), were used for analysis and comparison. Table 5.13 lists the variables and assumptions taken for sensitivity analysis.

Table 5.13: Variables and assumptions for comparison of counter-current and co-current operational mode using the Aspen Plus® sensitivity analysis tool

	Unit	Values	
Membrane Area	m ²	100	
Permeance		binary	ternary
H ₂	Nm ³ /(m ² .s.bar)	6.10E-05	5.78E-05
CO ₂	Nm ³ /(m ² .s.bar)	2.75E-05	2.37E-05
N ₂	Nm ³ /(m ² .s.bar)	-	1.35E-06
Feed Composition		binary	ternary
H ₂	mol/mol	0.6639	0.2983
CO ₂	mol/mol	0.3361	0.3033
N ₂	mol/mol		0.3984
Feed pressure	bar	10	
Permeate pressure	bar	1	
Temperature	°C	30	
Variables for sensitivity analysis			
Feed flow variation		binary	ternary
Start value	kmol/h	8	80
End value	kmol/h	1	40
Increase	kmol/h	1	1

Permeances and feed compositions in binary and ternary mixtures were taken from the laboratory tests (chapter 5.1.2.3). The membrane area was defined as 100 m² in all simulations. Furthermore, temperature, feed and permeate pressure were assumed as constant. Start and end values used for the sensitivity analysis in Aspen Plus® are also

listed in Table 5.13. With varying feed flow the respective permeate and retentate molar flows and concentrations were recorded.

5.2.3.4. ACM detailed model: Counter-current operational mode

Additionally to the base case model, a detailed model was developed where the pressure drop along the membrane module was considered. Thereto, additional information about the module was needed, such as fiber inner diameter, active fiber length, and number of fibers. The total membrane area was calculated according to equation EQ 51.

$$A_{Cell} = \frac{N_{Fiber} d_{i,Fiber} \pi l_{Fiber}}{N_{Cells}} \quad EQ 51$$

The Hagen-Poiseuille law was implemented into the simulation of the membrane unit operation to determine the pressure drop in each cell over the active fiber length of the module. Equation EQ 52 presents the applied Hagen-Poiseuille equation for cell k of a total number of cells N_{Cells} .

$$dp_k = \frac{128 R T \mu_k l_{Fiber} \dot{n}_{Retentate,k-1}}{\pi N_{Fiber} p_{Retentate,k-1} d_{i,Fiber}^4 N_{Cells}} \quad EQ 52$$

In equation EQ 52, μ is the dynamic viscosity of the gas, l_{Fiber} is the active fiber length, R is the gas constant, T is the operating temperature, $\dot{n}_{Retentate,k-1}$ is the volume flow in the fiber coming from cell $k-1$, N_{Fiber} is the number of fibers in the module, $p_{Retentate,k-1}$ is the pressure in the fiber at cell $k-1$, and $d_{i,Fiber}$ is the fiber inner diameter. For each cell the concentration, temperature and pressure dependent properties, such as density, enthalpy, and viscosity, were generated using the ‘call’ command in ACM. The ‘call’ command utilized the given information of the pertinent conditions to call the respective properties from the Aspen Properties data base. The viscosity in each cell could be determined and was used in equation EQ 52 to calculate the respective cell pressure drop dp_k . This pressure drop was subtracted from the retentate pressure $p_{Retentate,k-1}$ of the previous cell to obtain the retentate pressure in the present cell k . As a result, the retentate pressure decrease from cell to cell could be determined.

5.2.3.5. Implementation into Aspen Plus®

The counter-current and co-current models were exported from Aspen Custom Modeler® as installation files. After running the installation file, the respective membrane model was available as unit operation in the Aspen Plus® *custom models* database.

5.2.3.6. Determination of multi-component permeances with Aspen Plus® model

As permeances for multi-component gas mixtures differ from permeances for pure gases, the designed base case unit operation in Aspen Plus® was used to determine the actual values. Thereto a selection of results was taken from the 66/34/0 and 30/30/40 gas mixture measurements which are explained in chapter 5.1.2.3. With the measured gas compositions and volume flows of feed, permeate and retentate, the *Design Specification* function of the *Flowsheeting Options* in Aspen Plus® was used to determine the required permeances while fulfilling the volume flow balance at the applied conditions. The permeate flows were defined as *flow sheet variables*, with the respective measured values as *Specification target* and a defined *Tolerance*. For variation, the component permeances were used as *Manipulated variables* at defined *lower* and *upper limits*. The simulation varied the respective permeances until the permeance flows reached the defined target. As a certain permeance value for each component needed to be specified for the implementation into the multi-stage process, the arithmetic mean of the calculated permeances was the value of choice.

5.2.4. Multi-stage processes in Aspen Plus® based on counter-current modules

The ACM base case model with counter-current operational mode was chosen for the investigation of a multi-stage membrane separation process. Thereto, three different 2-stage configurations and one three-stage configuration were designed, namely setup 1, setup 2, setup 3, and setup 4. In the first two as well in the last configuration H₂-selective material was utilized, whilst CO₂-selective membranes were considered in setup 3. For all multi stage simulations the 66/34/0 feed gas mixture with 66 vol% H₂ and 34 vol% CO₂ was defined. The detailed feed gas stream conditions were specified as listed in Table 5.14, in which the reference pressure level is defined as 1 bar at an operational temperature of 30 °C. A feed gas volume flow of 1020 m³_N/h was chosen, because the final hydrogen-rich product gas stream should have an energy content of approximately 2 MW_{th}. The permeances for H₂-selective membrane material were defined according to the findings from practical investigation on mixed gases. Characteristics for the applied CO₂-selective material were taken from literature [Car et al., 2008]. These and further assumptions taken for the multi-stage processes in Aspen Plus® are listed in Table 5.15.

Table 5.14: Feed gas conditions defined for the Aspen Plus® two-stage simulation: source: [Lassmann et al., 2015]

Feed conditions	Unit	Value
Volume flow	Nm ³ /h	1020
Composition		
H ₂	vol%	66%
CO ₂	vol%	34%
N ₂	vol%	0%
Pressure	bar	1
Temperature	°C	30

Table 5.15: Assumptions for the multi-stage Aspen Plus® simulation; source: [Lassmann et al., 2015]

Assumptions for Simulation	Unit	Value
Membrane Module		
Permeance of H ₂ -selective material ^{a.)}		
Π _{H₂}	gpu [*]	81.3
Π _{CO₂}	gpu	36.7
Permeance of CO ₂ -selective material ^{b.)}		
Π _{H₂}	gpu	12
Π _{CO₂}	gpu	100
Operational temperature	°C	30
Compressor		
Compressor Model		isentropic
Number of compression stages		2
Compression stage 1	bar	1 - 4
Compression stage 2	bar	4 - 10
Isentropic efficiency	-	0.75
Mechanic efficiency	-	0.95

* 1 gpu = 1 x 10⁶ cm³(STP).cm⁻².s⁻¹.cmHg⁻¹

^{a.)} based on the findings from practical investigation on mixed gases

^{b.)} taken from literature [Car, et al. et al., 2008]

In the following subchapters the different process setups as well as the applied membrane area sensitivity analysis methods are described.

5.2.4.1. Two-stage process in Aspen Plus[®]: Setup 1

Setup 1 contains two compressors, where the first one is used to compress the feed gas to 10 bar before it is mixed with the recycle stream. This recycle stream is defined as the retentate from the second stage. The mixed stream is sent into the first membrane where the retentate is defined as the CO₂-rich off gas. The resulting permeate from the first membrane module needs to be compressed again to 10 bar before it is fed into the second membrane. The permeate from the second stage is defined as the H₂-rich product gas, whilst the retentate is used as the before mentioned recycle stream to the first stage. Figure 5.12 pictures the simplified flow sheet of setup 1.

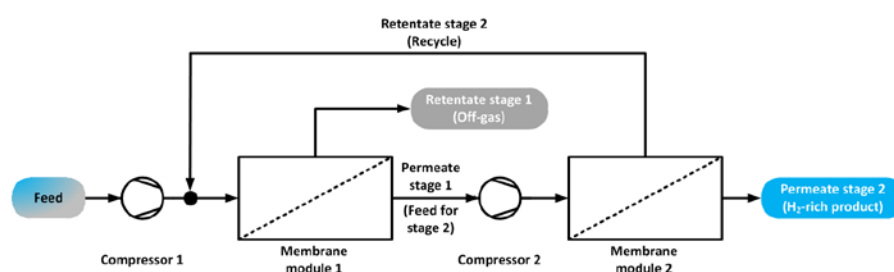


Figure 5.12: Setup 1, with two-stage configuration and H₂-selective membranes

5.2.4.2. Two-stage process in Aspen Plus[®]: Setup 2

As pictured in Figure 5.13 one of the main characteristic features of setup 2 is the need of only one compression stage. This is due to the fact that the pressure-prone retentate from the first stage is fed into the second membrane. In this configuration the second stage is used to recover the hydrogen from first stage's retentate. The permeate from the second membrane is sent back as recycle to be mixed with the feed stream in order to increase the overall recovery. The mixture of feed gas and recycle is compressed to 10 bar and fed into the first stage. The resulting first stage permeate is defined as the H₂-rich product gas and the resulting second stage retentate is the CO₂-rich off gas.

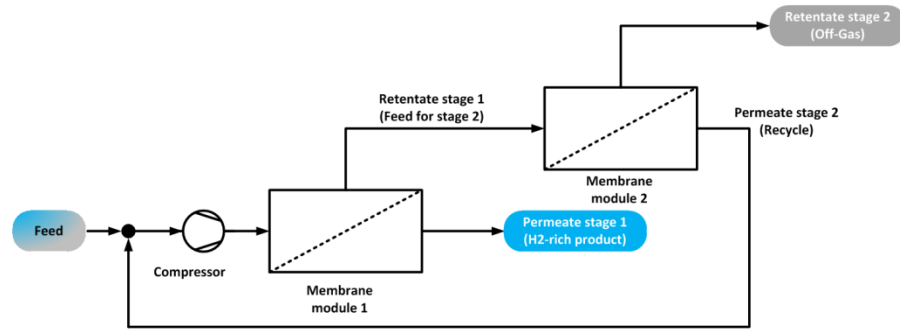


Figure 5.13: Setup 2, with two-stage configuration and H₂-selective membranes

5.2.4.3. Two-stage process in Aspen Plus[®]: Setup 3

Figure 5.14 shows that setup 3 consists of a similar arrangement as used in setup 2. The main difference is the assumption of revers-selective membrane material in both membrane modules. This results into a totally different purification approach, as the H₂-rich gas stream remains in both membrane modules on the pressure-bearing retentate side. The permeate from the second membrane is used as recycle stream to increase the hydrogen recovery. Gas permeating through the first membrane module is released as CO₂-rich off gas whilst the H₂-rich product is generated from the second stage retentate.

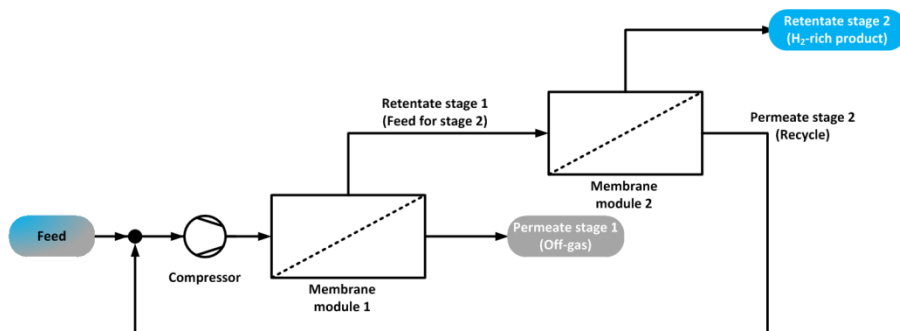


Figure 5.14: Setup 3, with two-stage configuration and CO₂-selective membranes

5.2.4.4. Three-stage process in Aspen Plus[®]: Setup 4

To investigate the influence of an additional membrane stage, a three-stage configuration was designed as pictured in Figure 5.15. The configuration is based in the principle of setup 1, with the permeate from the second membrane designated as the H₂-rich product. Same as for setup 1 two compressors are needed in setup 3. The pressure-prone retentate streams from stage 1 and 2 are mixed and sent into stage 3 for hydrogen

recovery purpose. As a result a CO₂-rich off gas is generated in the retentate from membrane module 3, whilst the respective permeate is used as recycle stream which is mixed with the feed gas before its compressed and fed into the first stage.

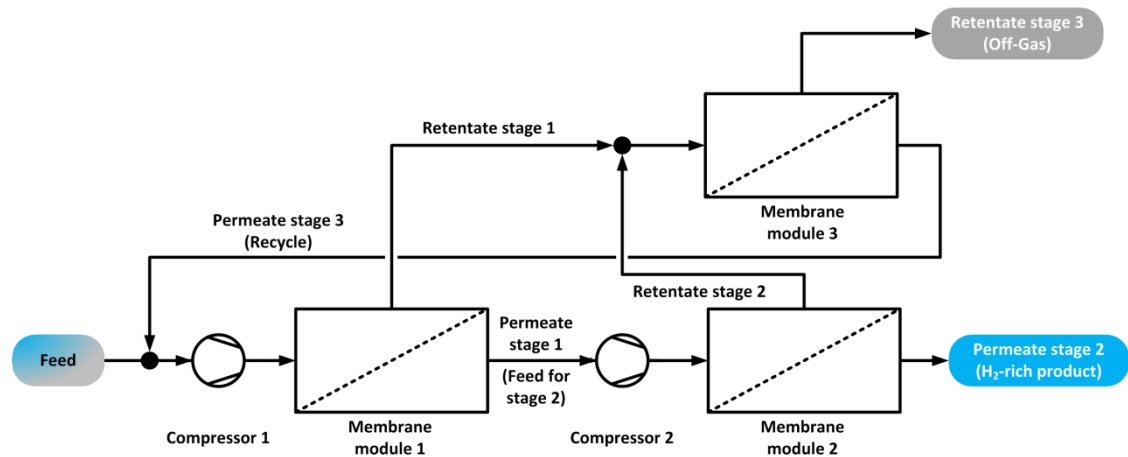


Figure 5.15: Setup 4, with three-stage configuration and H₂-selective material

5.2.4.5. Membrane area variation for two-stage processes

The previously described Aspen Plus[®] two-stage setups were used to determine the ideal setup that reaches the required hydrogen purity at acceptable hydrogen recovery. Thereto *sensitivity analysis* was applied, which is one of the *model analysis tools* available in Aspen Plus[®]. To perform the analysis *manipulated variables* and *flowsheet variables* were specified. In all setups the membrane areas of modules 1 and 2 served as *manipulated variables* which were varied within a *lower* and *upper bound* a certain *step size*. In Table 5.16 the respective data is presented. The *flowsheet variables* were defined as the flows and compositions of feed, permeate and retentate streams. All variables were chosen to be *tabulated variables*. During the sensitivity analysis the feed gas was set to the previously described conditions. It can be seen in Table 5.16 that the membrane area ranges differed for various setups. This was due to the diverse structures in the setups and the integration of the recycle streams. Additionally to the *sensitivity analysis* Aspen Plus[®] provides an *optimization tool*, which was used to find the membrane area configuration where the maximum product purity is reached while providing a minimum hydrogen recovery of 80% and a recycle to feed ratio below 0.4. This value was chosen due to feasibility reasons.

Table 5.16: Sensitivity analysis of membrane area variation for 2-stage processes

Variable	Unit	Setup 1	Setup 2	Setup 3
Membrane area A_1	m ²	600 - 800	100 - 400	100 - 300
Step size M_1	m ²	25	100	50
Membrane area A_2	m ²	200 - 450	200 - 400	200 - 800
Step size M_2	m ²	25	100	100

There to, the H₂-content in the product was defined as *flowsheet variable*, which shall be *maximized*. Hydrogen recovery and recycle to feed ratio were selected as *constraints* for the optimization. The variables in Table 5.16 were again applied as *manipulated variables* with the respective *limits* and *step size*.

5.2.4.6. Membrane area variation for three-stage processes

For the membrane area variation of the three-stage setup the same approach as for the two-stage analysis was chosen. Again, the *sensitivity* analysis in Aspen Plus[®] was used to find the ideal combination of the three membrane areas. The only difference was that the membrane area 3 was defined as an additional *manipulated variable*. Furthermore, the *optimization* tool was applied to determine the maximum product purity possible at a minimum H₂-recovery of 80%, with a maximum recycle-to-feed ratio of 0.4. Respective data for the *manipulated variables* during *sensitivity* analysis and *optimization* are given in Table 5.17.

Table 5.17: Sensitivity analysis of membrane area variation for 3-stage processes

Variable	Unit	Setup 4
Membrane area 1	m ²	250 - 400
Step size M1	m ²	25
Membrane area 2	m ²	300 - 500
Step size M2	m ²	25
Membrane area 3	m ²	25 - 125
Step size M3	m ²	25

5.3 Validation of the single-stage module

Ensuring the accuracy of the ACM base case model was done by validating the model by two different pathways, which were comparison with i.) measurements, and ii.) an existing model. Furthermore, CFD modeling results were used to verify the ACM

detailed model. These approaches are described in the subsequent chapters. The first two validation methods refer to the developed base case model with counter-current operational mode. For the verification with CFD modeling results, the ACM detailed model in counter-current operational mode was used.

5.3.1. Validation via measurements

The single-stage counter-current ACM gas permeation model was validated by comparing it with the results from laboratory measurements as reported in chapter 5.1.2.3. This was done for both, the 66-34-0 and 30-30-40 gas mixtures. The separation performance at constant temperature, different pressure levels, and varying feed gas streams was simulated with Aspen Plus[®]. Table 5.18 lists the assumptions that were taken for the validation. By variation of the feed gas flow, different stage-cut scenarios were simulated.

Table 5.18: Parameters for the validation of the ACM simulation model by comparison with measurements

Assumptions for Validation	Unit	Value
Membrane Module		
Membrane area	m ²	0.022431
Operational temperature	°C	30
Permeance of H ₂ -selective material		
for 66-33-0 mixture ^{a.)}		
Π_{H_2}	gpu [*]	81.3
Π_{CO_2}	gpu	36.7
for 30-30-40 mixture ^{b.)}		
Π_{H_2}	gpu [*]	77.0
Π_{CO_2}	gpu	31.7
Π_{N_2}	gpu	1.8
Feed gas stream		
Molar flow	mol/h	1.4 - 10
Pressure	bar	9 and 10

* 1 gpu = 1 x 10⁶ cm³(STP).cm⁻².s⁻¹.cmHg⁻¹

^{a.)} chosen values based on the findings from experimental work using the 66-34-0 gas mixture.

^{b.)} chosen values based on the findings from experimental work using the 30-30-40 gas mixture.

The simulation was compared with the results from measurements by means of hydrogen purity and recovery in the permeate stream.

5.3.2. Validation due to comparison with Makaruk&Harasek model

For further validation of the ACM simulation it was compared with an already existing algorithm developed by Makaruk and Harasek [2009], hereinafter referred to as Makaruk&Harasek model. This algorithm was suitable for comparison because it had been previously evaluated and validated against experimental and literature results. Furthermore, the algorithm had been successfully used in previous hydrogen purification simulations [Makaruk et al., 2011, Makaruk et al., 2012]. Eleven test cases for H₂/CO₂-separation were defined with varying parameters such as H₂-content in the feed, feed pressure, stage cut, and ideal selectivity. As Table 5.19 shows, the number of cells, feed flow, temperature, and permeate pressure were set as constant in all cases. Furthermore, the pressure drop along the fiber was neglected.

Table 5.19: Parameters varied for validation of the ACM simulation by comparison with Makaruk&Harasek model

Parameters	Unit	Variation
Number of Cells	-	100
Feed volume flow	Nm ³ /s	1
Temperature	°C	25
Permeate pressure*	bar	1
		0.2
Feed H ₂ fraction	vol/vol	0.5
		0.8
		3
Feed pressure*	bar	4
		7
		10
		0.2
Stage cut	vol/vol	0.5
		0.8
		3
		10
Ideal selectivity	-	25
		100

* Permeate and feed pressure are absolute pressures

5.3.3. Verification of the ACM detailed model by comparison with CFD simulation

To compare the ACM detailed model with CFD calculations a single fiber model was designed, both in ACM and OpenFoam[®]. The CFD calculations were performed by Schretter, P. [pers. Comm., 2015]. Figure 5.16 pictures the geometry of the single fiber. OpenFoam[®] is open source software, with the possibility to modify the available solvers according to user needs. As there were no solvers available that could handle mass transfer between two regions, Haddadi et al. [2016] developed a new solver, namely membraneFoam. This membraneFoam solver was capable of solving heat and mass transfer for each of the regions and furthermore simulating the mass and energy transfer from one region to the other region [Haddadi et al., 2015]. The considered fiber had an inner diameter of 0.4 mm and a length of 280 mm. It was assumed that the membrane was operated at 30 °C and 10 bar with a respective permeate pressure of 1 bar.

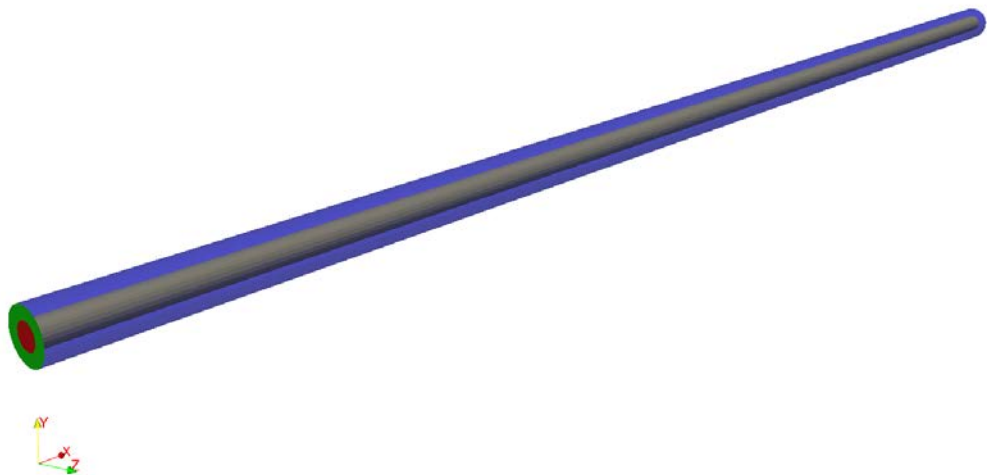


Figure 5.16: Design of a single fiber for CFD simulation in OpenFoam[®], designed by Schretter, P. [2015]

Five test cases were defined with constant composition and varying feed flow from 1.7 to 5 L/h. The composition was according to the 30-30-40 gas mixture used during experimental work, containing 30 vol% H₂, 30 vol% CO₂, and 40 vol% N₂. Table 5.20 lists the assumptions taken for the validation by comparison with CFD modeling based on a single fiber. Detailed information about the settings for CFD simulation can be found in Haddadi et al. [2016].

Table 5.20: Parameters varied and assumptions taken for validation of the ACM simulation by comparison with CFD simulation

Parameters	Unit	Variation
Fiber geometry		
Inner diameter	mm	0.4
Length	mm	280
Operational conditions		
Feed pressure*	bar	10
Permeate pressure*	bar	1
Temperature	°C	30
		1.714
		2.573
Feed volume flow	L_N/h	3.429
		4.286
		5.143

* Permeate and feed pressures are absolute pressures

By comparing the ACM detailed model with CFD simulation the accuracy regarding separation performance was determined. In this regard the retentate and permeate flows and compositions were chosen as comparative values. Furthermore, the considered pressure drop effect along the longitudinal axis on the inside of the membrane was determined in both simulations.

6. Results & Discussion

The subsequently presented results are divided into two main sections, experimental and simulative results. Findings of the experimental work include pure gas and gas mixture separation performance from laboratory measurements, as well as field test results. Parts of these experimental findings were then further used in the simulations. In the simulative section the results from the developed ACM gas permeation models are presented, including single-stage and multi-stage processes. Furthermore, the validation results of the ACM model are shown, as well as possible utilization scenarios for the purification off-gas.

6.1 Experimental part

During experimental work various hollow fiber membrane materials were examined, membrane modules were built and tested with pure gases as well as two different gas mixtures in the laboratory. The respective results are presented in the subsequent chapters. Moreover, measurements from the field tests, where the small scale pilot plant was connected to a fermenter, are presented. These include fermentation progression over time and the purification performance of the pilot plant under real conditions. All experimental results presented in the following chapters are based on reconciled values. After field tests, the utilized membrane modules were tested again with pure gases and the respective result are also presented. At the end of the experimental part, the effect of data reconciliation is shown based on a representative example.

6.1.1. Pure gases

In Figure 6.1 results for membrane module M-1 are presented and it can be seen that the trans-membrane flow for hydrogen, as well as for carbon dioxide, strongly depended on the applied pressure difference between feed and permeate. With higher pressure difference the respective permeate flow rose. This effect was stronger for hydrogen than for carbon dioxide. It can be further seen, that there was a linear correlation between the respective trans-membrane flows and the applied pressure difference. An additional transmembrane flow increase was generated when higher operational temperatures were applied. At a pressure difference of 9 bar, the transmembrane flow increased by 60%, when operated at 50 °C instead of 30 °C. According to the solution diffusion model, these trends were expected.

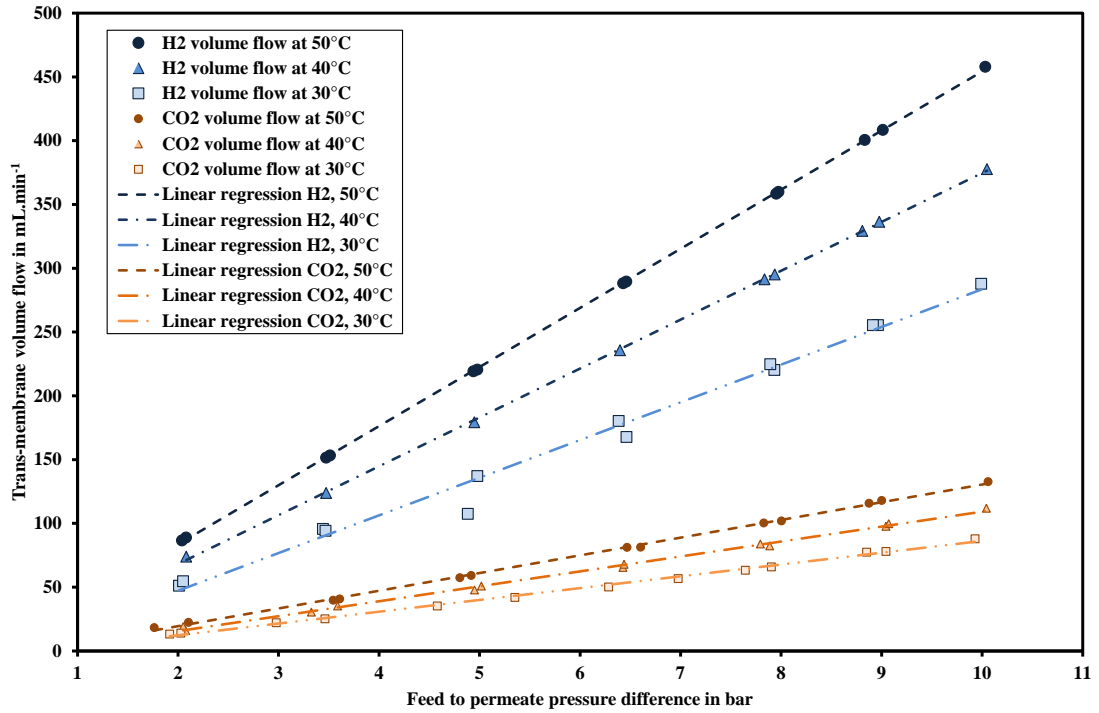


Figure 6.1: Membrane module M-1 - Influence of temperature and pressure difference on trans-membrane flow of H₂ and CO₂

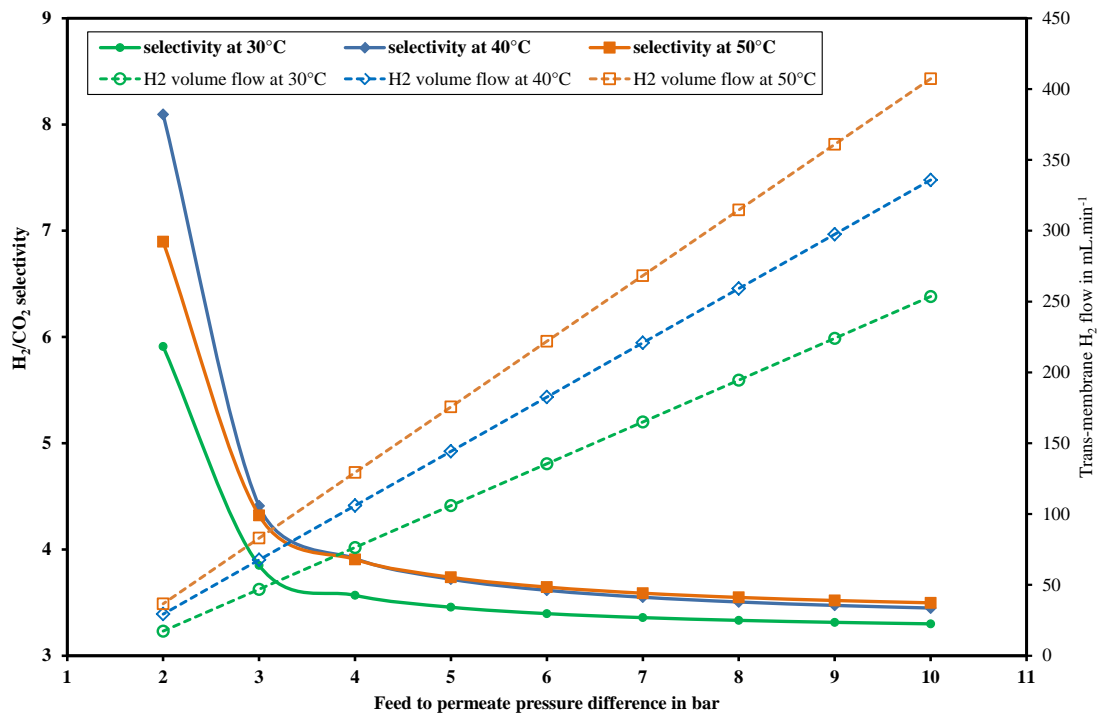


Figure 6.2: Membrane module M-1 - H₂/CO₂ selectivity and H₂ volume flow against the pressure difference at three different temperature levels (30°C, 40°C, 50°C)

It is clearly visible that the temperature increase had a stronger effect on the H₂ trans-membrane flow compared to the CO₂ trans-membrane flow. Hence, it might be assumed that a temperature increase results into a better separation of H₂ and CO₂. To be able to confirm this assumption, the ideal H₂/CO₂-selectivity was determined, which is an indicator for separation efficiency.

Table 6.1: Pure gas measurement results for membrane module M-1

Experimental conditions		Ideal selectivity			Permeance in Nm ³ /(m ² .s.bar) *10 ⁻⁶		
T in °C	Δp in bar	H ₂ /CO ₂	H ₂ /N ₂	CO ₂ /N ₂	H ₂	CO ₂	N ₂
30	2	3.80	n.d.	n.d.	35.3	9.3	n.d.
30	3.5	3.75	n.d.	n.d.	37.2	9.9	n.d.
30	5	3.40	n.d.	n.d.	35.7	10.5	n.d.
30	6.5	3.37	30.16	8.96	36.7	10.9	1.2
30	8	3.39	31.44	9.29	38.1	11.2	1.2
30	9	3.29	29.83	9.07	38.7	11.8	1.3
30	10	3.32	n.d.	n.d.	38.4	11.6	n.d.
<i>average (30 °C)</i>		<i>3.45</i>	<i>29.67</i>	<i>8.60</i>	<i>36.8</i>	<i>10.7</i>	<i>1.24</i>
40	2	4.14	n.d.	n.d.	47.4	11.4	n.d.
40	3.5	3.76	n.d.	n.d.	48.2	12.8	n.d.
40	5	3.66	n.d.	n.d.	48.9	13.4	n.d.
40	6.5	3.54	31.79	8.98	49.7	14.	1.6
40	8	3.51	31.66	9.03	50.3	14.4	1.6
40	9	3.43	32.83	9.56	50.7	14.8	1.5
40	10	3.40	n.d.	n.d.	51	15	n.d.
<i>average (40 °C)</i>		<i>3.62</i>	<i>31.60</i>	<i>8.74</i>	<i>49.4</i>	<i>13.7</i>	<i>1.6</i>
50	2	4.06	n.d.	n.d.	57.64	14.2	n.d.
50	3.5	3.87	n.d.	n.d.	59.00	15.2	n.d.
50	5	3.70	n.d.	n.d.	59.99	16.2	n.d.
50	6.5	3.61	32.02	8.88	60.66	16.8	1.9
50	8	3.53	31.85	9.01	61.04	17.3	1.9
50	9	3.47	33.58	9.68	61.36	17.7	1.8
50	10	3.46	n.d.	n.d.	61.37	17.7	n.d.
<i>average (50 °C)</i>		<i>3.66</i>	<i>32.01</i>	<i>8.76</i>	<i>60.2</i>	<i>16.5</i>	<i>1.9</i>

n.d.: not detected, because the volume flow rate was too low.

In Figure 6.2 the trans-membrane hydrogen flow is shown again, together with the respective ideal H₂/CO₂ selectivity and its dependency on feed to permeate pressure difference, as well as on the applied temperature. Figure 6.2 shows that the ideal H₂/CO₂ selectivity changed with increasing pressure difference. However, it was a declining selectivity gradient, which approached a threshold value, depending on the applied temperature. The highest selectivity was obtained at a low pressure difference, but the respective trans-membrane flow was extremely low and hence not feasible. This can be seen as a trade-off between selectivity and trans-membrane flow. An optimal operation point was set with an absolute pressure of 10 bar at 50 °C. With respect to the measurements when connected to a fermenter, the optimal temperature was changed to 30 °C. The ideal H₂/CO₂-selectivity at 10°bar and 50 °C accounted for 3.5 with a respective H₂ volume flow of 453 mL/min. When operating the membrane at a reduced temperature of 30°C the ideal H₂/CO₂-selectivity and the transmembrane flow decreased to 3.3 and 255 mL/min, respectively. The given transmembrane flow values refer to an estimated membrane area in the module of 1.232x10⁻² m². Table 6.1 lists the measurement results for ideal selectivities and permeances of membrane module M-1. Besides the H₂ permeances, the respective values for CO₂ and N₂ are also presented. At various conditions it was not possible to detect the trans-membrane flow for N₂ and as a result the respective values for N₂ permeance, H₂/N₂ and CO₂/N₂ are not given.

6.1.1.1. Comparison of membrane modules

Additionally to the before presented results, further membrane modules were tested with pure gases. From Figure 6.3 to Figure 6.5 the respective results for membranes M-2, M-3, and M-4 are pictured. The trans-membrane flows in M-2 were in a similar range as in M-1, which had been expected because the same type of fibers was used in the membrane modules. In membrane module M-3 a different type of PI fibers was built-in. The respective hydrogen and carbon dioxide trans-membrane flows were three times higher than for modules M-1 and M-2. When using PP fibers, as done in module M-4, the trans-membrane flows increased by more than tenfold. Again, a temperature dependency for the trans-membrane flow was detected. Despite a major difference in trans-membrane flow compared to PI membranes, the utilization of PP material showed no other superior characteristics. Table 6.2 lists the results of ideal selectivity, H₂ and CO₂ permeances depending on temperature for membrane modules M-1, M-2, M-3, and M-4. For ease of comparison the listed results are presented as average values over a feed pressure range from 2 to 11 bar.

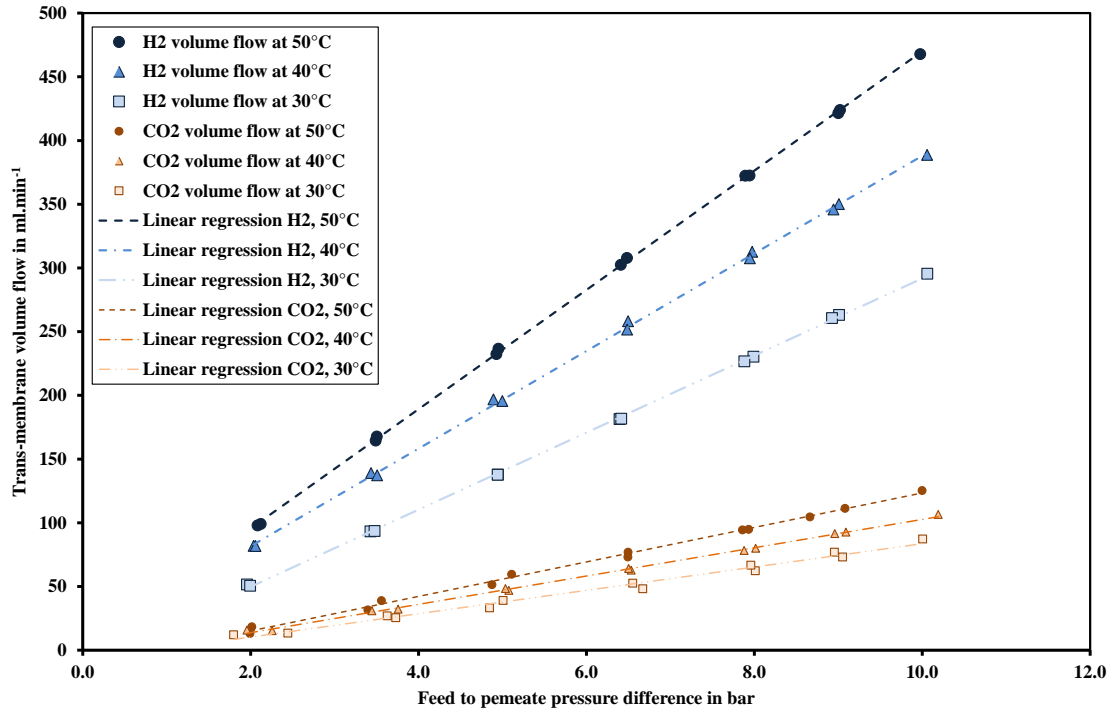


Figure 6.3: Membrane module M-2 - Influence of temperature and pressure difference on trans-membrane flow of H₂ and CO₂

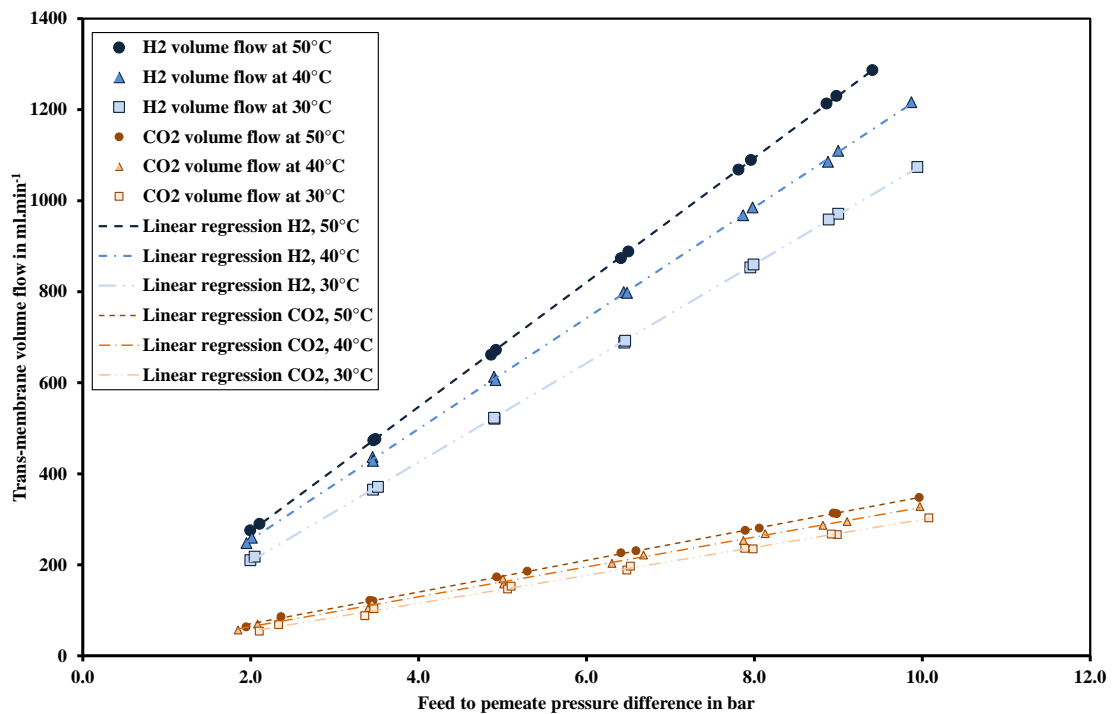


Figure 6.4: Membrane module M-3 - Influence of temperature and pressure difference on trans-membrane flow of H₂ and CO₂

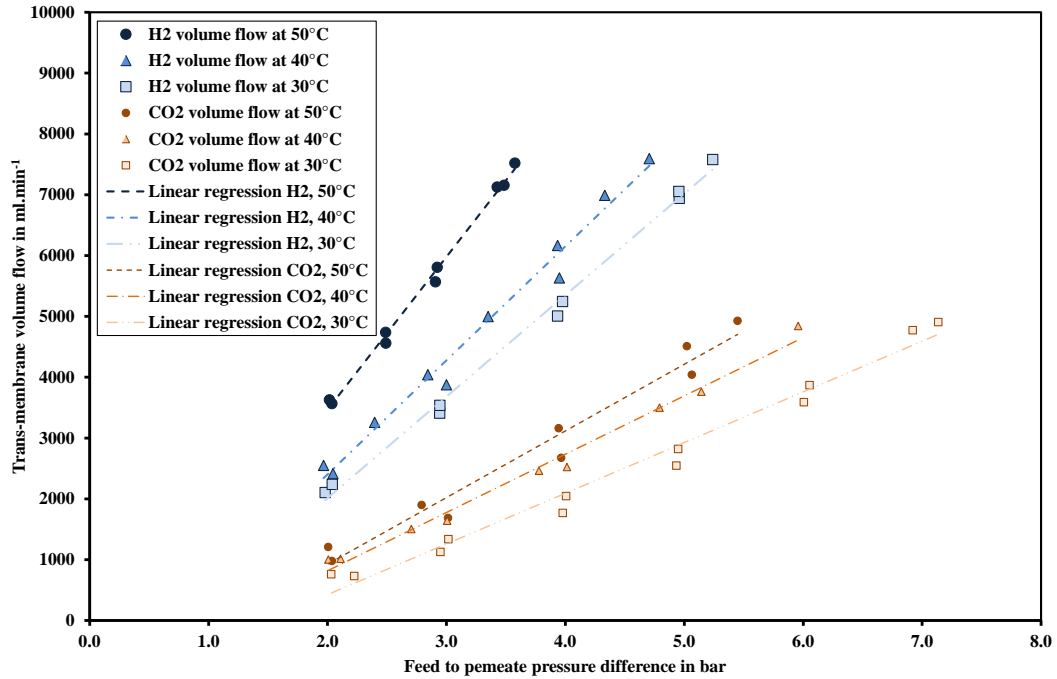


Figure 6.5: Membrane module M-4 - Influence of temperature and pressure difference on trans-membrane flow of H₂ and CO₂

Table 6.2: Comparison of membrane modules M-1, M-2, M-3, and M-4 regarding ideal selectivity and permeance

Membrane notation	Applied temperature	Ideal selectivity	Permeance in Nm ³ /(m ² .s.bar) *10 ⁻⁶	
	T in °C		H ₂ *	CO ₂ *
M-1	30	3.45	36.8	10.7
	40	3.62	49.4	13.7
	50	3.66	60.2	16.5
M-2	30	3.70	46.2	12.5
	40	4.17	64.7	15.5
	50	4.26	77.5	18.2
M-3	30	3.67	144.4	39.4
	40	3.83	168.3	44
	50	3.91	185.2	47.4
M-4	30	2.55	65140	25552
	40	2.20	66934	30431
	50	2.71	91679	33774

*all average values over pressure range

With an ideal H₂/CO₂ selectivity smaller 3, the PP material in membrane module M-4 appeared to be unsuitable for the purification task. The different permeances for module M-1 and M-2 were unexpected, as the same membrane material was used. One possible explanation could be that there was a deviation in the assumed membrane area. Even though the H₂ permeances in membrane module M-3 were threefold higher compared to M-1 and M-2, it had no substantial impact on the selectivity because the same effect was detected for the CO₂ permeances. As a result the ideal H₂/CO₂ selectivities were in the same range and did not show any further superior properties despite the before mentioned higher trans-membrane flows.

6.1.1.2. Temperature dependency of the permeances

In order to determine the temperature dependency of H₂ and CO₂ permeances in the different membranes, the results from pure gas measurements were correlated with the Arrhenius equation (see chapter 5.2.1.2). The respective results for the polyimide-based membrane modules M-1, M-2, and M-3 are presented in Figure 6.6 and for the PP-based module M-4 in Figure 6.7. Both figures show that there was a distinct linear correlation between the logarithmic permeance and the inverse temperature. The application of an Arrhenius-type temperature dependency was therefore seen as valid.

The activation energies calculated from the Arrhenius relationship for the respective membrane modules M-1 and M-2 were 20.0 and 21.1 kJ/mol for hydrogen, as well as 15.3 and 17.6 kJ/mol for carbon dioxide. The calculated values for module M-3 were 10.1 and 7.5 kJ/mol for H₂ and CO₂ respectively. The linear regression of the PP-membrane data resulted in respective H₂ and CO₂ activation energy values of 13.8 and 11.4 kJ/mol. These results are also listed in Table 6.3, followed by estimated pure gas parameters for operation at an elevated temperature of 80°C. The calculated parameters from the Arrhenius relationship were used to determine the H₂ and CO₂ permeances and respective ideal selectivities at 80°C. This would give information about a possible improvement of performance at higher temperatures. The estimation results listed in Table 6.3 show, that the H₂ permeances of M-1 and M-2 were more than tripled compared to the values at 30 °C, whilst the CO₂ permeances were only increased by a factor of 2.5. Consequentially the ideal H₂/CO₂ selectivities of M-1 and M-2 were also elevated. This trend appeared for all four membrane modules, in some stronger and in some weaker. What immediately caught attention was the discrepancy between M-1 and M-2 at 80°C, with the former suggesting an ideal selectivity of 3.95 compared to a 5.21 value for the latter.

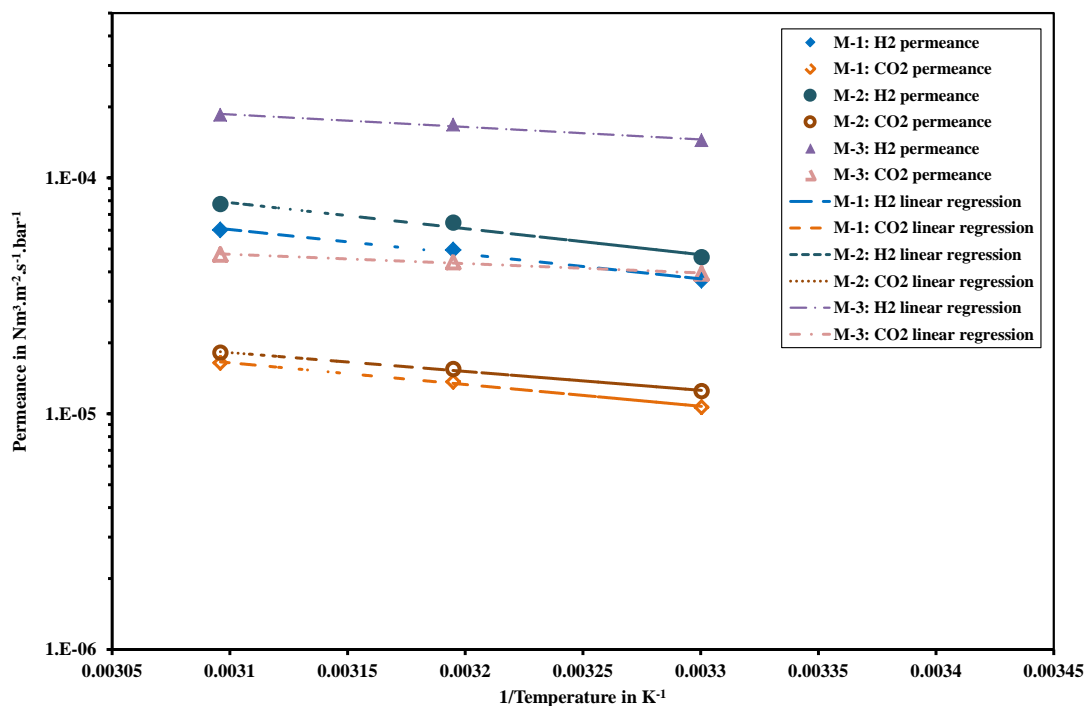


Figure 6.6: Temperature dependency of permeance for PI membranes M-1, M-2, M-3 with linear regression for Arrhenius equation

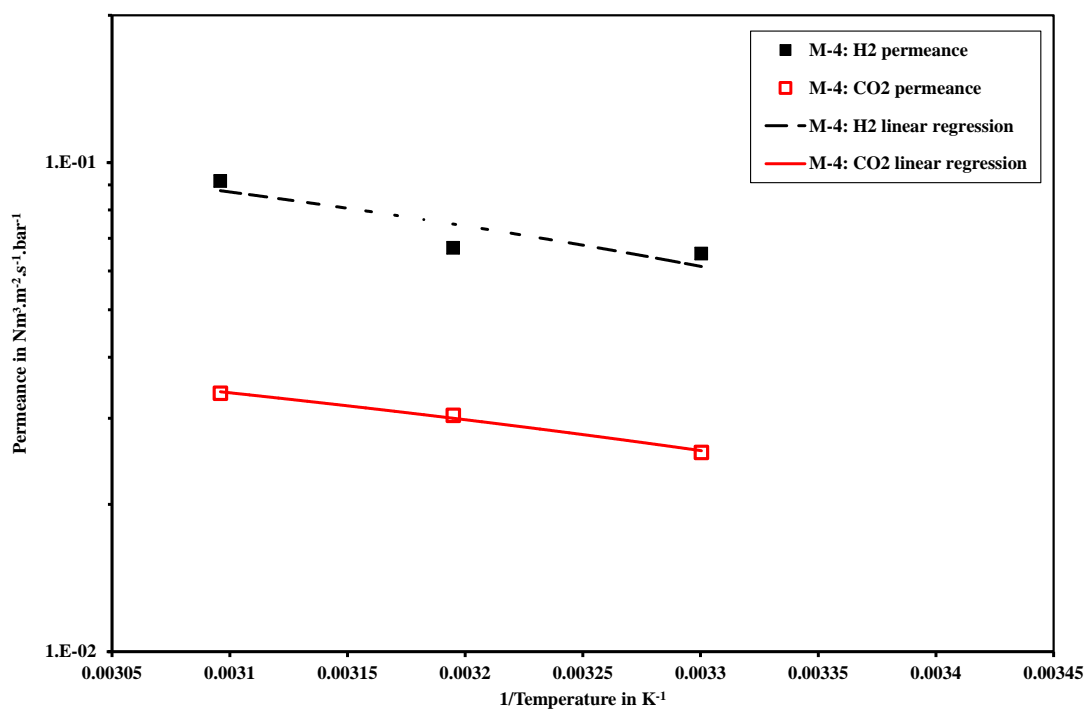


Figure 6.7: Temperature dependency of permeance for PP membrane M-4 with linear regression for Arrhenius equation

Table 6.3: Arrhenius parameters and estimation of purification parameters at elevated temperature

Arrhenius parameters	Gas		Membrane notation
	H ₂	CO ₂	
Activation Energy E_p in kJ/mol	20.00	17.65	M-1
	21.12	15.32	M-2
	10.16	7.57	M-3
	13.78	11.37	M-4
Pre-exponential factor P_{i,0} in Nm ³ /(m ² *s*bar)	0.1049	0.0119	M-1
	0.2063	0.0055	M-2
	0.0082	0.0008	M-3
	14.71	2.36	M-4
Estimation of purification parameters at 80°C based on Arrhenius equation			
Permeance P_i at T_{operation} = 80°C in Nm ³ /(m ² *s*bar)*10 ⁻⁶	115.00	29.08	M-1
	154.72	29.71	M-2
	257.27	60.73	M-3
	134608	48967	M-4
Ideal H₂/CO₂ selectivity at T_{operation} = 80°C		3.95	M-1
		5.21	M-2
		4.24	M-3
		2.75	M-4

This was due to the fact that the calculated activation energies and pre-exponential factors differed, even though the same material had been used. An explanation for this matter could be traced back to the deviation in assumed membrane area which might have led to higher permeances for module M-2. Turning the focus on the PP membrane module M-4 the estimation showed that even at 80°C an ideal H₂/CO₂ selectivity higher 3 could not be achieved. With this, a further investigation of PP-membrane material for the purification task became irrelevant.

6.1.2. Gas mixtures

For the investigation of gas mixtures membrane modules M-1 and M-2 were chosen and arranged in parallel. From here on, this arrangement will be termed as module M-P. In the subsequent chapters the results for two different feed gas mixtures are presented. The first subchapter shows the results using a binary mixture containing mainly hydrogen and carbon dioxide. The second subchapter addresses the findings for

a ternary mixture which contained nitrogen additionally to the two before mentioned components. Finally, a comparison of pure and mixed gas results is presented.

6.1.2.1. Feed gas mixture: 66/34/0

The investigation of the membrane module M-P with a gas mixture containing 66 vol% of hydrogen, 34 vol% of carbon dioxide and 0 vol% of nitrogen showed a cutback in H_2/CO_2 selectivity compared to the pure gas results, but this will be assessed particularly in chapter 6.1.2.3. In this chapter information about the membrane's performance in terms of hydrogen recovery and product purity is presented. As pictured in Figure 6.8, there was a trade-off between H_2 -purity and H_2 -recovery in the permeate stream. For the applied H_2 -selective membrane material, the H_2 -recovery increased with increasing stage cut – whilst the H_2 -purity in the permeate decreased. By decreasing the stage cut θ (see also *EQ 39*), which is equivalent to a reduction of transmembrane flow, the H_2 -recovery is reduced. This means that a large portion of the hydrogen would be lost into the retentate. The analysis also showed, that the trend of the permeate H_2 -purity for a single stage process approached a certain maximum, with decreasing stage cut. For the given 66-34-0 mixture in the feed stream the maximal H_2 -purity was reached at 82 vol%. It is apparent that a 16% increase of H_2 -purity in the permeate (product) with a simultaneous loss of more than 20 vol% of hydrogen to the retentate, is not a desirable performance for the gas upgrading process.

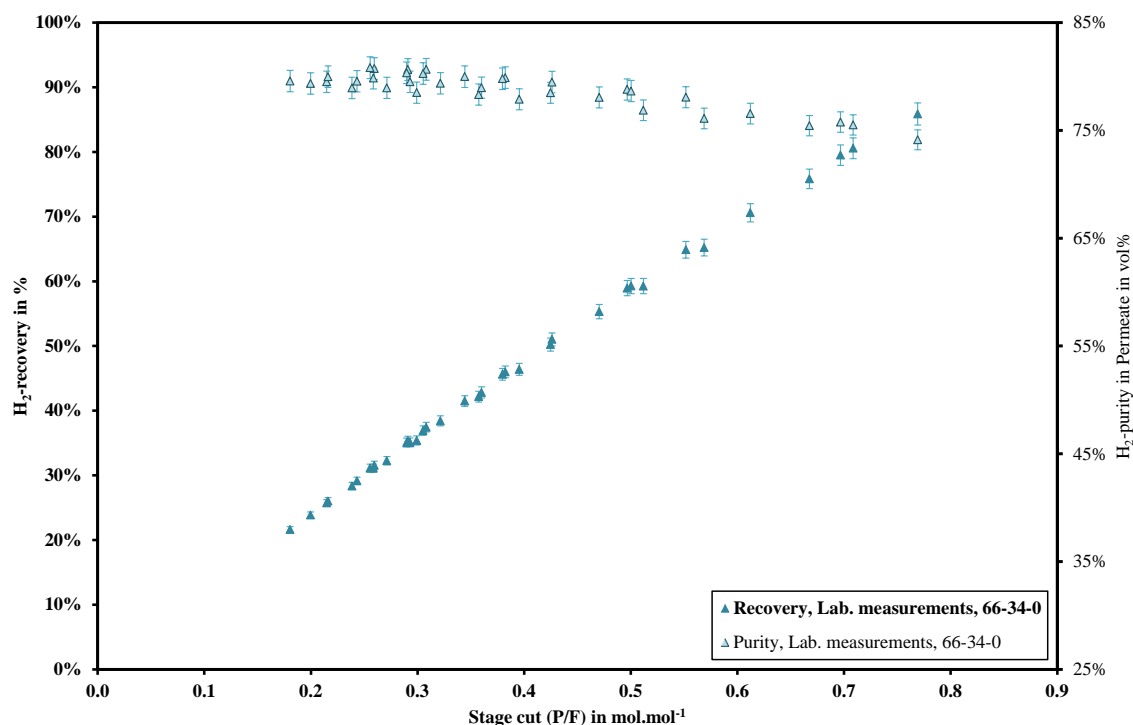


Figure 6.8: H₂-recovery and H₂-purity in a single-stage for the 66-34-0 feed gas mixture depending on the stage cut; all data is taken from laboratory results

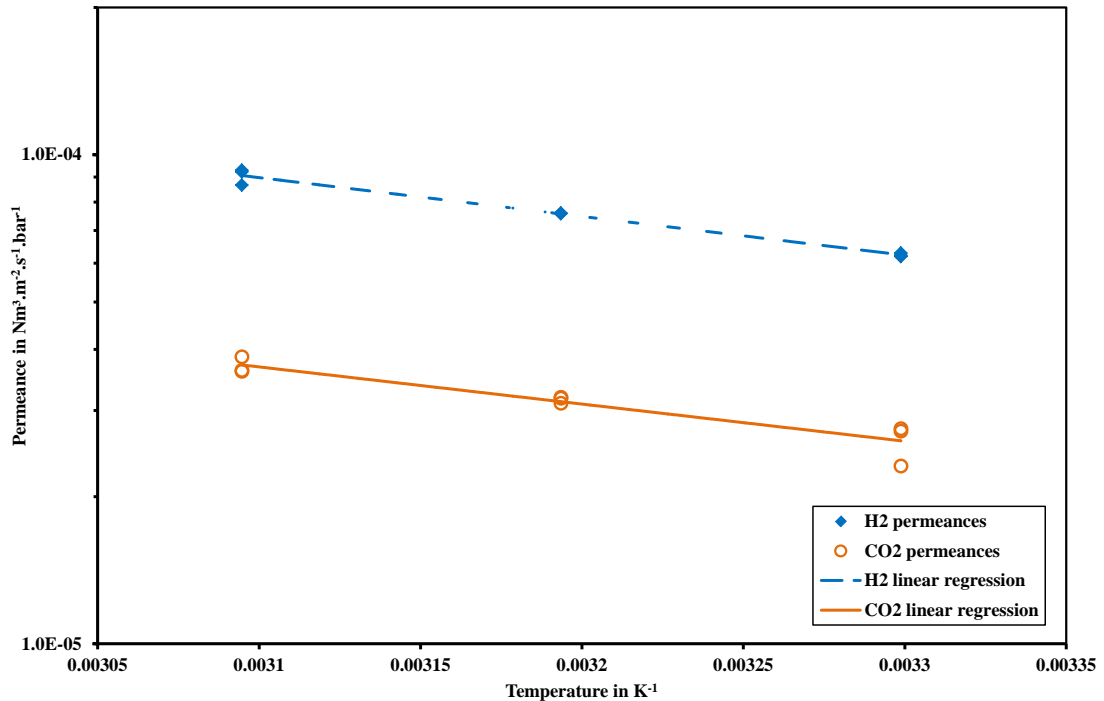


Figure 6.9: H₂ and CO₂ permeances depending on temperature, Arrhenius equation for 66-34-0 mixture

Figure 6.9 shows the Arrhenius plot for the binary gas mixture. Again, a linear trend was found which confirmed the assumption of an Arrhenius type temperature dependency. The same approach as for the pure gas measurements was applied to determine the activation energy and pre-exponential factor of both components. For H₂ and CO₂ the activation energy resulted in 15.2 and 14.5 kJ/mol, with respective pre-exponential factors of 0.0259 and 0.0083 Nm³/(m².s.bar). With these values, the estimated component permeances at 80 °C were calculated. For H₂ and CO₂ the permeances accounted for 145.9 × 10⁻⁶ and 58.5 × 10⁻⁶ Nm³/(m².s.bar).

6.1.2.2. Feed gas mixture: 30/30/40

As stated in the previous chapter, a cutback in H₂/CO₂ selectivity compared to pure gas results was also observed for measurements using a feed gas mixture containing 30 vol% hydrogen, 30 vol% carbon dioxide and 40 vol% nitrogen. But, that specific matter will be discussed in the next chapter in detail. Figure 6.10 shows the H₂-recovery and H₂-purity in the permeate over the stage cut, based on the measurement results for all applied temperatures and feed flow rates. The same trade-off as for the

binary mixture was observed, as the H₂-recovery increased with increasing stage cut whereas the H₂-purity in the permeate declined. For the hydrogen purity trend a maximum of 67 vol% would be reached at the lowest stage cut and minimum recovery. The decline of H₂-purity with increasing stage cut is more pronounced compared to the binary feed gas stream. This is attributed to the lower hydrogen content in the ternary feed gas mixture as well as to the presence of the low permeating nitrogen. It is important to notice that the investigated stage cut range for the 30-30-40 mixture was limited to a maximum of 0.32, due to the chosen laboratory setup. The presence of nitrogen clearly limited the purification performance, with respect to the highest achievable product purity and hydrogen recovery. Again, an Arrhenius type temperature dependency was detected for all three components, as it is shown in Figure 6.11. The respective H₂, CO₂ and N₂ activation energy accounted for 16.2, 11.4 and 10.7 kJ/mol, with related pre-exponential factors of 0.0346, 0.0021 and 9×10^{-5} Nm³/(m².s.bar). With these values, the permeance at an elevated temperature of 80 °C was determined, by using the Arrhenius equation. The resulting H₂, CO₂ and N₂ permeances were 139.6×10^{-6} , 43.1×10^{-6} and 2.4×10^{-6} Nm³/(m².s.bar).

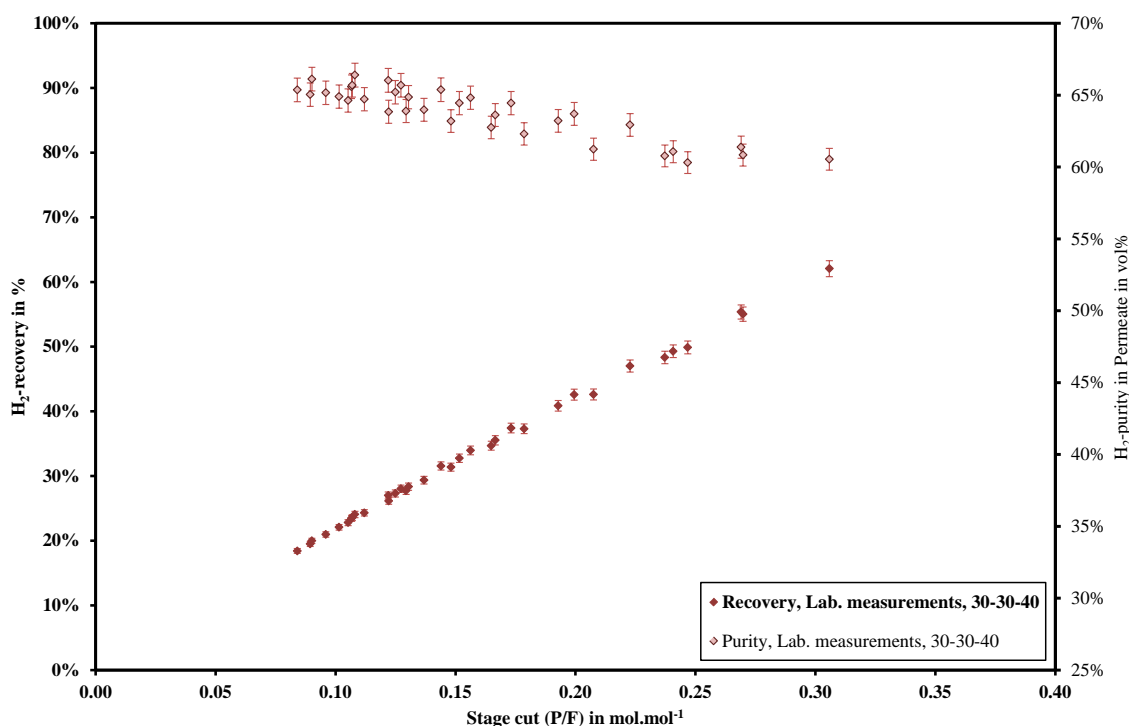


Figure 6.10: H₂-recovery and H₂-purity in a single-stage for the 30-30-40 feed gas mixture depending on the stage cut; all data are taken from laboratory results

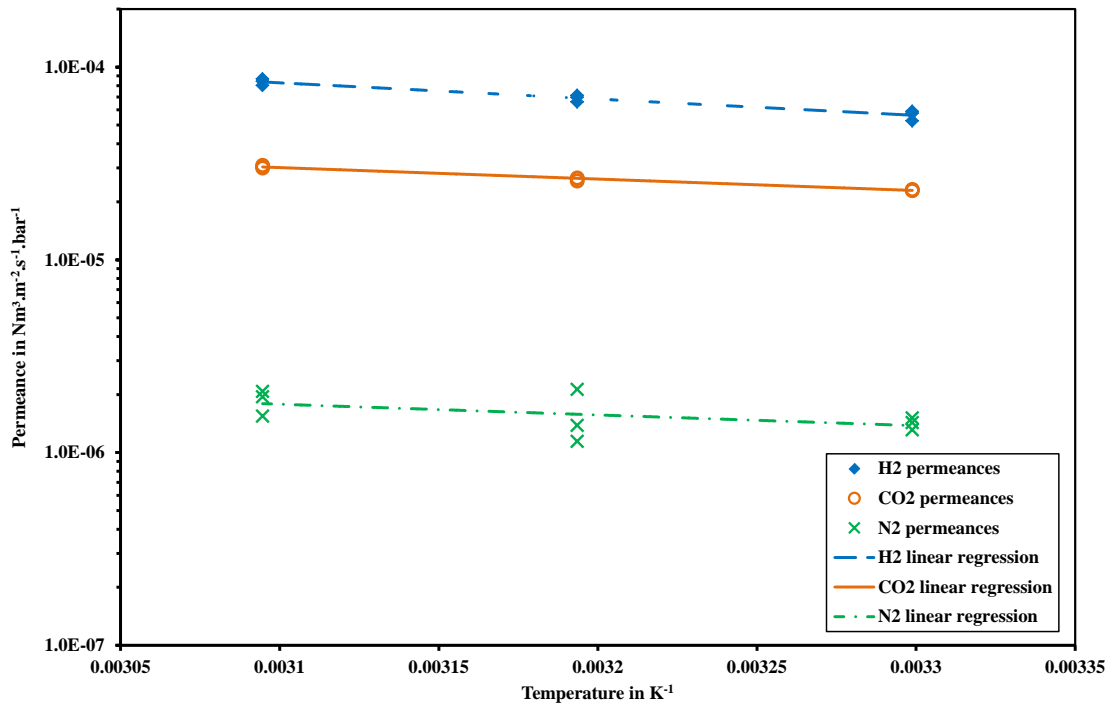


Figure 6.11: H₂, CO₂ and N₂ permeances depending on temperature, Arrhenius equation for 30-30-40 mixture

6.1.2.3. Comparison of pure gases and gas mixtures

It is a well-known fact that pure gas membrane specifications often differ from mixed gas results and therefore are not the best option to predict purification performances. In order to confirm this statement, the measurement results from pure and mixed gas tests were compared with each other in terms of permeances and selectivity. The respective results are presented in Table 6.4. A first thing immediately to recognize is that the H₂ and CO₂ permeances for mixed gases extend the values of pure gas measurements. This effect was slightly stronger for the binary than for the ternary mixture and more severe with decreasing temperature. The values for mixed gas H₂ permeances were between 1.4 and 1.7 times higher compared to the pure gas results and the mixed gas CO₂ permeances had 1.9 to 2.6 higher values than their pure gas counterparts. Based on these trends the respective selectivities of H₂/N₂ and CO₂/N₂ also increased, but the crucial selectivity of H₂/CO₂ decreased by the factor 0.7. In the pure gas results, the H₂/CO₂ selectivities were above 3, but for the mixed gas measurements this value dropped below 3. Table 6.4 further shows a H₂/CO₂ selectivity increase with increasing temperature. Based on the Arrhenius type temperature dependency this trend reaches values of 3.3 and 2.5 at 80 °C for the respective ternary and binary gas mixtures.

Table 6.4: Comparison of permeances and selectivities of gas mixtures and pure gases

Temp. in °C	Ternary gas mixture*			Binary gas mixture*			Pure gases**		
	30	40	50	30	40	50	30	40	50
Permeance in Nm ³ /(m ² *s*bar) *10 ⁻⁶									
H ₂	57.69	70.81	84.34	62.67	75.16	90.63	36.82	49.44	60.15
CO ₂	23.74	27.28	31.08	27.37	32.51	36.34	10.67	13.67	16.45
N ₂	1.34	1.67	2.05	-	-	-	1.24	1.56	1.88
Selectivity***									
H ₂ /N ₂	44.72	43.11	41.55	-	-	-	29.69	31.69	31.99
CO ₂ /N ₂	18.35	16.58	15.30	-	-	-	8.60	8.76	8.75
H ₂ /CO ₂	2.43	2.60	2.71	2.29	2.31	2.49	3.45	3.62	3.66

* mean value over feed volume flow at 10 bar feed pressure

** mean value over pressure range

*** ideal selectivity for pure gases

In Table 6.5 and Table 6.6 the measurement results for H₂ composition in the permeate stream are presented compared to theoretical values based on either pure gas permeances or mixed gas permeances. These theoretical values were calculated according to the respective equations *EQ 6* and *EQ 7* for binary and ternary gas mixtures, as described in chapter 5.1.2.3. Table 6.5 lists the results for the binary 66-34-0 feed stream mixture and in Table 6.6 the results regarding to the ternary 30-30-40 mixture are shown. These Tables shall give an insight into the accuracy of simplified algebraic predictions regarding permeate composition. For the binary feed gas mixture, using pure gas permeances resulted in a deviation up to 16.7% from the measured permeate composition. This was detected at the highest temperature (50 °C) and the lowest feed flow rate (60.5 NL/h). For both theoretical approaches, pure and mixed gas permeances, the following behavior was identified: With increasing temperature the deviation increased, and for a constant temperature the deviation increased with decreasing feed volume flow. With the mixed gas permeances the highest deviation was reduced to 10%.

Table 6.5: Comparison of theoretical and measured H₂ composition in permeate for a 66-34-0 feed gas mixture

Mixed gas measurement 66-34-0			H ₂ composition in Permeate		
Feed conditions			Measurement	Theoretical calculation ^{1.)} based on	
T	Average vol. flow	p		Pure gas permeances	Mixed gas permeances
in °C	in NL/h	in bar	in mol/mol	in mol/mol	in mol/mol
30	60.6	10.05	0.761		0.801
30	118.3	10.02	0.785	0.859	0.817
30	178.0	10.01	0.794		0.806
40	60.5	10.02	0.754		0.813
40	119.1	10.02	0.790	0.864	0.812
40	177.8	10.01	0.796		0.804
50	60.5	10.09	0.741		0.815
50	119.5	10.01	0.795	0.865	0.821
50	178.1	10	0.806		0.824

^{1.)} Calculation method is described in chapter 5.1.2.3, equations EQ 6.

The results of the ternary feed gas mixture showed the same behavior as the binary ones with the highest deviation at the highest temperature and smallest feed volume flow. However, the maximum deviation when using the pure gas permeances for the calculation of the H₂ permeate composition according to equation EQ 7 (see chapter 5.1.2.3) was 12.6%, which is 4.1% less than the maximum deviation for the binary feed gas. For the utilization of mixed gas permeances the same trend was expected. But, the results showed that the maximum deviation was 11.1%, which accounts for an unexpected increase of 1.1%. When using mixed gas permeances for calculation, almost all permeate composition values showed higher deviation than the respective calculations for binary mixture.

Table 6.6: Comparison of theoretical and measured H₂ composition in permeate for a 30-30-40 feed gas mixture

Mixed gas measurem. 30-30-40			H ₂ composition in Permeate		
Feed conditions			Measurement	Theoretical calculation ^{1.)} based on	
T	Average vol. flow	p		Pure gas permeances	Mixed gas permeances
in °C	in NL/h	in bar	in mol/mol	in mol/mol	in mol/mol
30	59.4	10.03	0.608		0.651
30	120.1	10.03	0.639	0.659	0.662
30	179.3	10.03	0.650		0.666
40	60.4	10.01	0.608		0.664
40	121.1	10.07	0.644	0.674	0.672
40	178.2	10.04	0.657		0.676
50	60.3	10.04	0.605		0.672
50	121.7	10.01	0.644	0.682	0.678
50	181.9	10.02	0.660		0.683

^{1.)} Calculation method is described in chapter 5.1.2.3, equations EQ 7.

Summarizing the comparison of pure and mixed gas tests it can be stated that for operational conditions of 30°C and a feed pressure of 10 bar, the H₂/CO₂-selectivity decreased from 3.5 to 2.3 for a binary mixture and to 2.4 for a ternary mixture. However, this value reflected the findings for polyimide membrane material from literature [(Car, et al., 2008)], [(Shao, et al., 2009)]. The slight selectivity difference could be explained by the CO₂-induced plasticization effect going along with the difference in the CO₂ partial pressure of the feed stream. This phenomenon may have been related to the competitive sorption between H₂ and CO₂ for the free volume sorption sites in the polymer. Due to the slightly higher content of CO₂ in the binary gas mixture more sorption sites in the polymer are preferentially occupied with it and less are available for H₂.

6.1.3. Integrated gas separation

During online measurements the small scale pilot plant, using membrane module M-P, was connected to a hydrogen fermenter. The findings obtained during online gas separation are discussed in this chapter. These contain information about the fermentation itself, including the course of fermenter performance over time, followed by results from the actual purification process under the present conditions. The chapter is concluded with a comparison of the membrane module's pure gas results before and after the online gas separation.

6.1.3.1. Fermentation

A key factor for the design of the small scale pilot plant was the potential amount and composition of fermenter gas. Based on the knowledge from previous work, the 600 L fermenter was supposed to produce 250 L_N/h of hydrogen-rich gas, containing 66 vol% H₂ and 34 vol% of CO₂. Unfortunately, these values were hardly achieved over the time span of the field measurements and it was necessary adding nitrogen to obtain the required volume flow rate for successful operation. Figure 6.12 shows the fermenter gas composition over that time span. It is clearly visible that the expected fermenter gas composition was only reached towards the end of the measurements.

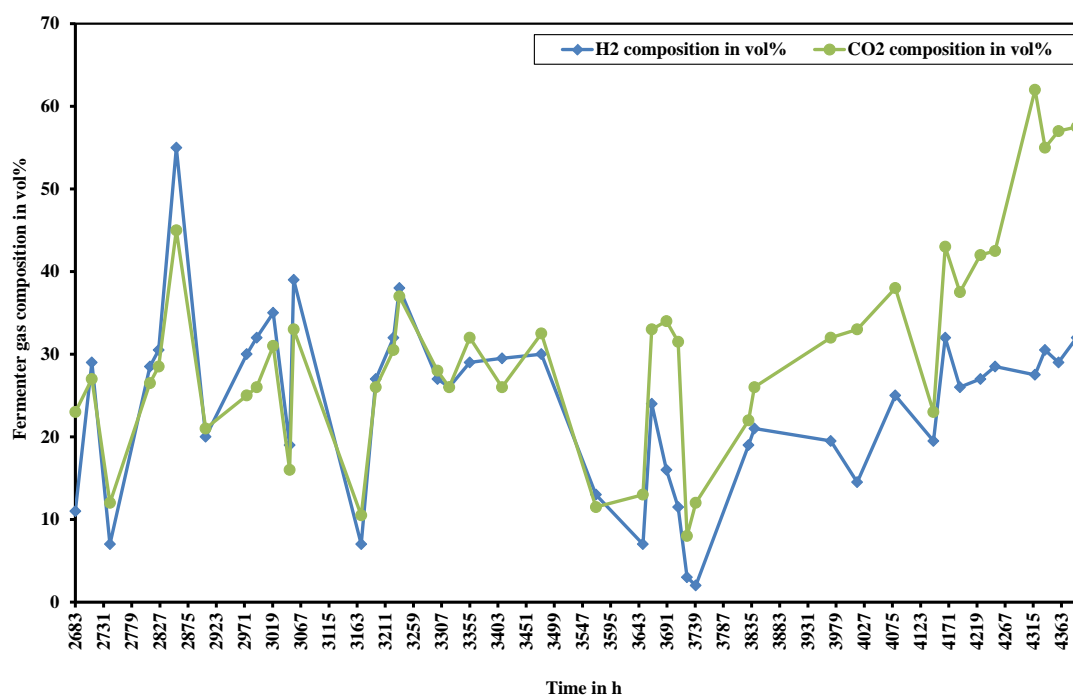


Figure 6.12: Fermenter gas composition over time during online gas separation

The main reason for the discrepancy between expected and actual fermenter performance is that several technical problems occurred over the course of fermenter operation. These are particularly discussed in Appendix A. During measurements it was detected that the feed gas composition varied continuously, even though a large gas bag was inserted to compensate slight variations. Figure 6.13 pictures the variation of the fermenter gas composition on the example of 18 selected measurements.

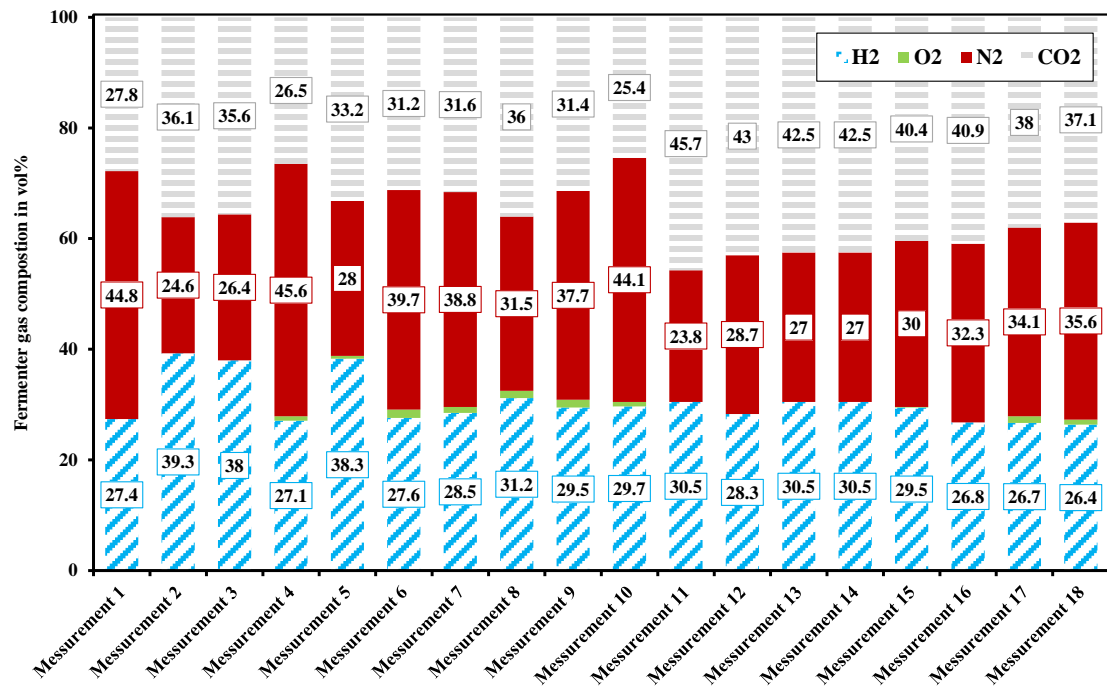


Figure 6.13: Fermenter gas composition for different measurements

Over the presented span of 18 measurements the hydrogen content varied between 26.4 and 39.3 vol%, the carbon dioxide content between 25.4 and 45.7 vol%, and the nitrogen content from 23.8 to 44.8 vol%. The effect on the purification performance due to varying feed gas composition will be discussed in the next chapter.

6.1.3.2. Purification with small-scale pilot plant

As discussed in the previous chapter, the fermenter gas composition varied from expected values. This influenced the online gas purification performance of the small scale pilot plant. Figure 6.14 pictures the H₂-purity and H₂-recovery over a stage cut range from 0.03 to 0.23. The H₂-recovery showed a linear trend similar to the mixed gas measurements, where the H₂-recovery increased with increasing stage cut. In this graph the corresponding H₂-purity is also presented which did not indicate a clear trend. This can be attributed to the varying feed gas composition, because based on the solution-diffusion mechanism a possible H₂-purity in the permeate strongly depends on the H₂-concentration in the feed stream. Even though the H₂-purity results didn't show the desired trend, the online gas purification was considered successful. Based on the acquired data it was possible to demonstrate that PI membranes can be used to purify fermentatively produced hydrogen.

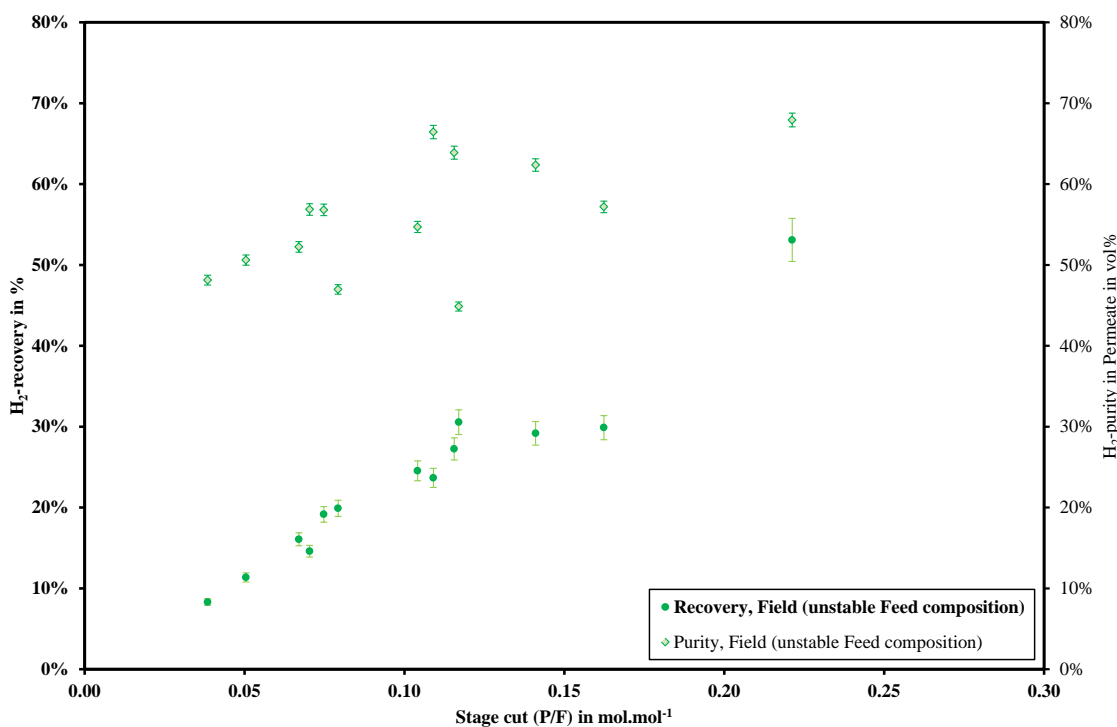


Figure 6.14: H₂-recovery and H₂-purity during online gas separation measurements depending on the stage cut

6.1.3.3. Comparison of the utilized membrane modules before and after field tests

During the field tests the membrane modules M-1 and M-2 were combined in a parallel arrangement for the purification of the fermenter gas. After the online gas purification, these membrane modules were once more separately examined with pure gases in the laboratory. Table 6.7 lists a comparison of the H₂, CO₂, and N₂ permeances for membrane module M-1 before and after the online gas measurements. In Table 6.8 the respective ideal selectivities are presented. Apparently, the utilization of the membrane modules had an effect on the permeances because an increase was detected for all three components. Especially for hydrogen and carbon dioxide the values were elevated to a significant extend. An explanation for this increase could be due to the carbon dioxide induced membrane swelling, also known as plasticization. As the polyimide is continuously exposed to a carbon dioxide rich environment over a long period of time, the void space in the polymer is steadily stretched which may affect its relaxation time. The relaxation time describes the timeframe the polymer needs to restore its initial state. These possible long term effects on the substance's permeance did have a positive effect on the respective selectivities. Table 6.8 shows that the H₂/N₂ and CO₂/N₂ selectivities were increased twofold, based on their average values. For H₂/CO₂ selectivities the effect was only slightly detectable.

Table 6.7: Comparison of pure gas permeances before and after the field tests for membrane module M-1

Pressure difference	Permeance					
	N ₂		CO ₂		H ₂	
	before	after	before	after	before	after
in bar	in Nm ³ /(m ² .s.bar) *10E-6		in Nm ³ /(m ² .s.bar) *10E-6		in Nm ³ /(m ² .s.bar) *10E-6	
1	0.929	6.925	3.97	25.98	23.49	91.84
2	1.096	3.628	8.24	29.26	31.73	104.34
3	1.152	2.529	9.66	30.35	34.47	108.51
4	1.179	1.980	10.37	30.90	35.84	110.59
5	1.196	1.650	10.80	31.22	36.67	111.84
6	1.207	1.431	11.08	31.44	37.22	112.67
7	1.215	1.274	11.29	31.60	37.61	113.27
8	1.221	1.156	11.44	31.72	37.90	113.71
9	1.226	1.064	11.56	31.81	38.13	114.06
10	1.229	1.331	11.65	31.88	38.31	114.34

Table 6.8: Comparison of ideal selectivities before and after the field tests for membrane module M-1

Pressure difference	Selectivity					
	H ₂ /N ₂		CO ₂ /N ₂		H ₂ /CO ₂	
	before	after	before	after	before	after
in bar	-	-	-	-	-	-
1	25.27	13.26	4.28	3.75	5.91	3.54
2	28.95	28.76	7.52	8.06	3.85	3.57
3	29.93	42.90	8.39	12.00	3.57	3.58
4	30.39	55.85	8.79	15.60	3.46	3.58
5	30.66	67.77	9.03	18.92	3.40	3.58
6	30.83	78.76	9.18	21.98	3.36	3.58
7	30.95	88.93	9.29	24.81	3.33	3.58
8	31.04	98.38	9.37	27.44	3.31	3.59
9	31.11	107.17	9.43	29.88	3.30	3.59
10	31.17	85.88	9.48	23.95	3.29	3.59

The respective tables for membrane module M-2 are presented in Appendix B.1.

6.1.4. Application of data reconciliation

All data acquired during laboratory and field measurements had to undergo data reconciliation to ensure that material balances were closed. The effect of the applied data reconciliation is presented in this chapter using five example measurements (Ex 1 to Ex 5). These examples were taken from laboratory measurements using the ternary feed gas mixture. Each of the 5 examples represents one particular feed gas volume flow, from 60 L/h to 180 L/h. Table 6.9 lists the raw measurement data and in Table 6.10 the corresponding reconciled measurements are presented. The measurement parameters were divided into two variable groups, measured and unmeasured. Permeate flow, retentate flow, and their respective H₂ and CO₂ compositions were declared as measured variables. As unmeasured variables defined were feed flow, as well as the N₂ content in feed, permeate and retentate. The residual values, H₂ and CO₂ content in the feed, were assumed to be constant because a test gas cylinder with consistent gas composition was used.

Table 6.9: Measurement data before DR

	Unit	Raw measurement				
		Ex 1	Ex 2	Ex 3	Ex 4	Ex 5
Measured variables						
Permeate flow	mL/min	253.7	272.3	278.6	284.1	289.1
Permeate composition						
H ₂	mL/mL	0.614	0.630	0.645	0.651	0.655
CO ₂	mL/mL	0.362	0.340	0.336	0.329	0.327
Retentate flow	mL/min	759.5	1238.0	1742.4	2238.8	2710.9
Retentate composition						
H ₂	mL/mL	0.202	0.232	0.249	0.259	0.266
CO ₂	mL/mL	0.289	0.298	0.301	0.302	0.302
Unmeasured variables						
Feed flow	mL/min	1013.2	1510.3	2021.0	2522.9	3000.0
Composition						
N ₂ Feed	mL/mL	0.398	0.398	0.398	0.398	0.398
N ₂ Permeate	mL/mL	0.024	0.030	0.019	0.020	0.018
N ₂ Retentate	mL/mL	0.509	0.470	0.450	0.439	0.432

From comparison of the raw example data with the reconciled measurements it can be seen that with increasing feed flow the relative correction (RC) decreased. The relative correction was defined as the absolute difference between raw measurement and

reconciled value referred to the reconciled value. The before mentioned trend was also detected for the RC of the permeate and retentate volume flows. Concerning volume flows, the highest necessary RC occurred for the permeate flow of example measurement Ex 1 with 1%. For the compositions of the measured values, the value of the retentate H₂ content needed to be reconciled with an RC of 2%. For the RC of H₂ and CO₂ compositions of permeate as well as the CO₂ content in the retentate the same trend was noticed. Due to the arithmetic dependency of the N₂ content to the respective measured variables and the particular low concentration on the permeate side, the most significant RCs were detected for the unmeasured variables of N₂ composition in permeate and retentate.

Table 6.10: Measurement data after DR

	Unit	Reconciled measurement				
		Ex 1	Ex 2	Ex 3	Ex 4	Ex 5
Measured variables						
Permeate flow	mL/min	251.1	270.6	277.3	283.2	288.3
Permeate composition						
H ₂	mL/mL	0.603	0.623	0.640	0.647	0.652
CO ₂	mL/mL	0.360	0.339	0.335	0.329	0.327
Retentate flow	mL/min	766.4	1244.7	1749.2	2245.0	2717.4
Retentate composition						
H ₂	mL/mL	0.198	0.228	0.244	0.254	0.261
CO ₂	mL/mL	0.285	0.295	0.298	0.300	0.301
Unmeasured variables						
Feed flow	mL/min	1017.5	1515.4	2026.6	2528.2	3005.7
Composition						
N ₂ Feed	mL/mL	0.398	0.398	0.398	0.398	0.398
N ₂ Permeate	mL/mL	0.037	0.038	0.025	0.024	0.022
N ₂ Retentate	mL/mL	0.517	0.477	0.458	0.446	0.438

In summary it can be said that the designed data reconciliation was a successful tool to even out the mass balances from field and laboratory measurements. In cases where no reconciliation was possible the respective data set was removed and declared as disqualified.

6.2 Simulative part

During the course of the simulative work, a single stage unit operation was developed using the process simulation tool Aspen Custom Modeler[®]. The data obtained during practical work was implemented into the single stage models, including the base case model and the detailed model. The base case model was further used to design and investigate numerous multi-stage setups. The subsequent chapters present the results and findings regarding operational parameters of the base case single stage unit, its validation and the verification results of the detailed model. Furthermore, findings of the investigated multi-stage processes are presented, followed by calculation results of the off-gas utilization scenarios.

6.2.1. Single stage

The presented subchapters contain the main findings of the investigation regarding the different single-stage membrane modules. These include the effects of number of cells and the sensitivity analysis results for the comparison of operational modes.

6.2.1.1. Influence of number of cells

The designed base case unit operation with counter-current operational mode was used to determine the influence of total number of cells N_{Cells} on its accuracy. Figure 6.15 shows the mole fraction of the respective gas streams depending on the length of the membrane. To be able to compare the different configurations for number of cells a relative cell number was used. This means that the value “0” represents cell number 0 in the simulation and value “1” depicts cell number N_{Cells} .

It can be seen in Figure 6.15 that from 0 to 1 the CO_2 content in the permeate decreased, whilst the H_2 content increased. Simultaneously, the H_2 and CO_2 concentrations on the retentate side decreased respectively increased. As expected, the same concentration trends for the three different numbers of cells occurred. It is clearly visible that with increasing number of cells, the trends approached a certain maximum respectively minimum. Furthermore, the difference between 100 Cells and 500 Cells was barely detected. To further investigate the number of cells' influence on the simulation performance, its effects on the H_2 partial pressure were also determined. Figure 6.16 shows the trends of the simulated H_2 partial pressures on the retentate side of the membrane module based on different number of cells. With increasing number of cells the steps due to pressure difference from cell to cell got smaller, until they reached an almost smooth transition.

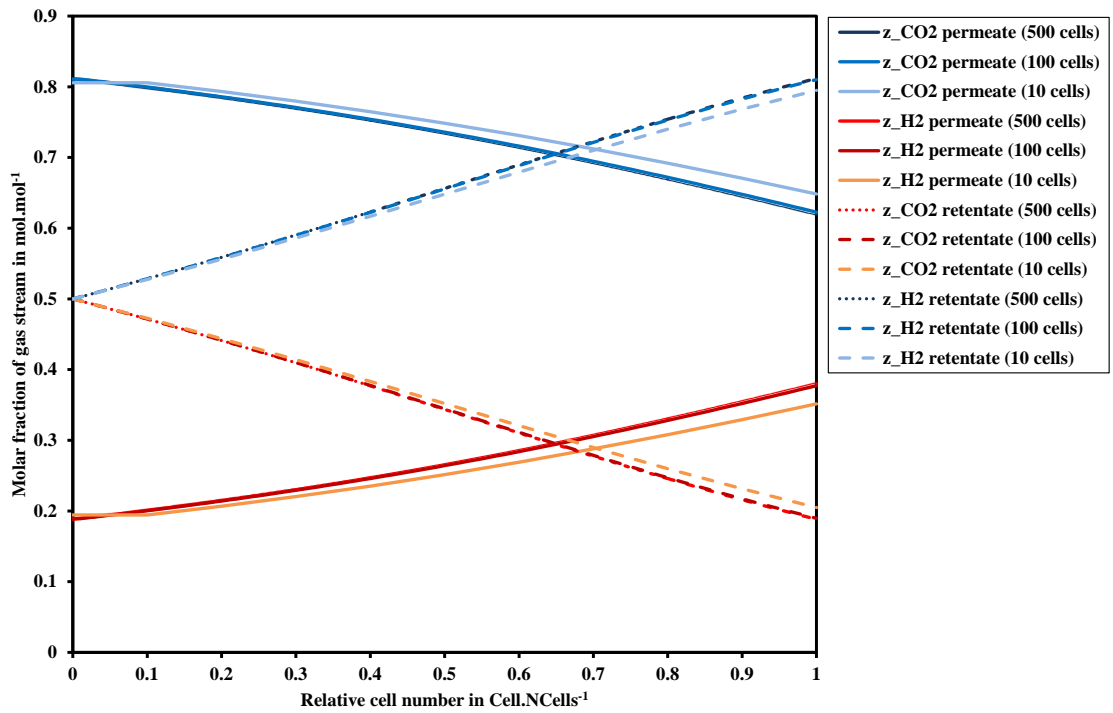


Figure 6.15: ACM calculation of H₂ and CO₂ content in the permeate and retentate flow for three different number of cells; base case model with counter-current operational mode

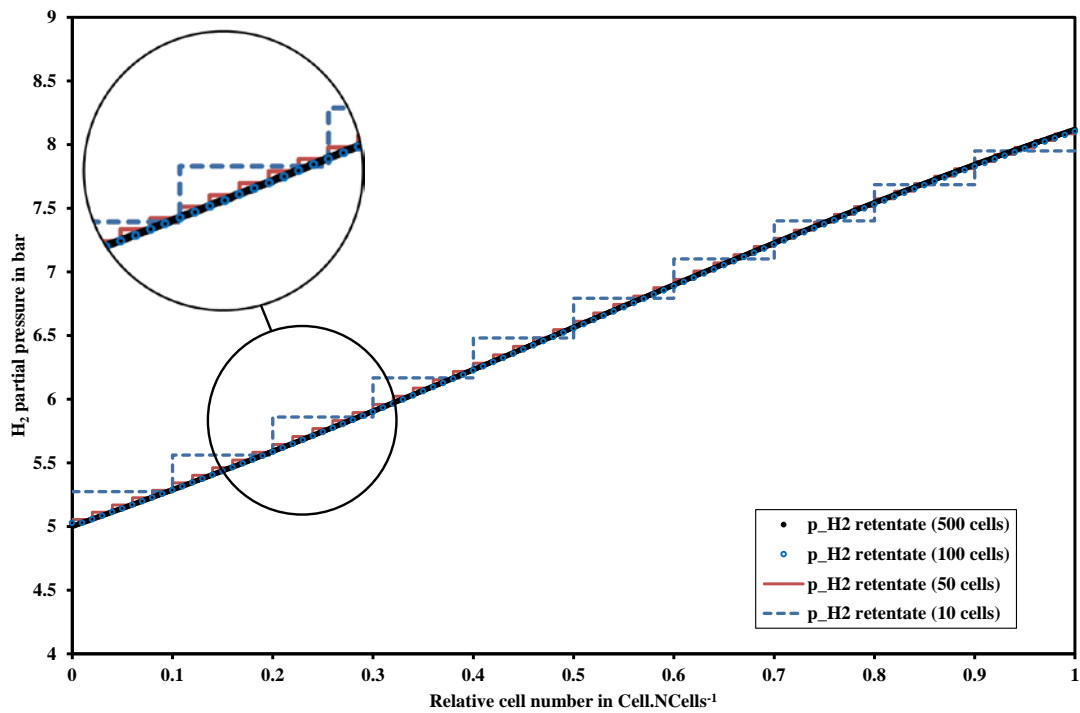


Figure 6.16: ACM calculation of the hydrogen partial pressure in the retentate for three different numbers of cells; base case model with counter-current operational mode

For the 50 cell simulation small steps were clearly apparent, but the difference between 100 cells and 500 cells was hardly visible. The same comparison was done for the partial pressure of hydrogen on the permeate side. These results are presented in Figure 6.17.

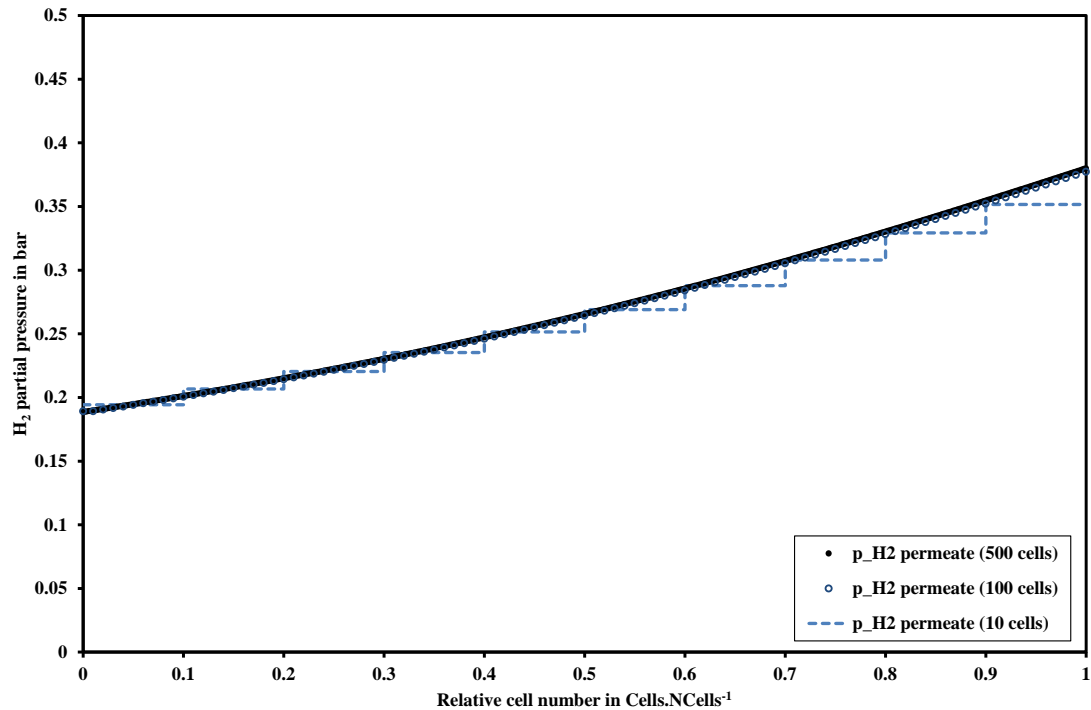


Figure 6.17: ACM calculation of the hydrogen partial pressure in the permeate for three different numbers of cells; base case model with counter-current operational mode

From investigation regarding the effect of different number of cells on the membrane unit operation it can be concluded that an increase in number of cells is conterminous with an improvement of computational accuracy. Even though the computational time of the membrane model in ACM was slightly enhanced with increasing number of cells, it still was below one second. A higher number of cells made discretization of the system more complex and harder to solve. This could also have a disadvantageous effect on the convergence of the system.

For further utilization and investigation the 100 cell system was chosen, because it had an upside in terms of convergence and the accuracy increase from 100 to 500 cells was seen as insignificant.

6.2.1.2. Comparison of counter-current and co-current operational mode

The ACM base case model was designed in two different operational modes, which were counter-current and co-current. A sensitivity analysis was performed to compare the two different approaches and to determine the better fitting mode for utilization in a multi-stage system. Figure 6.18 shows a comparison of both operational modes. This graph presents the H₂-recovery and H₂-purity results depending on the stage cut, for the respective binary and ternary feed gas mixture.

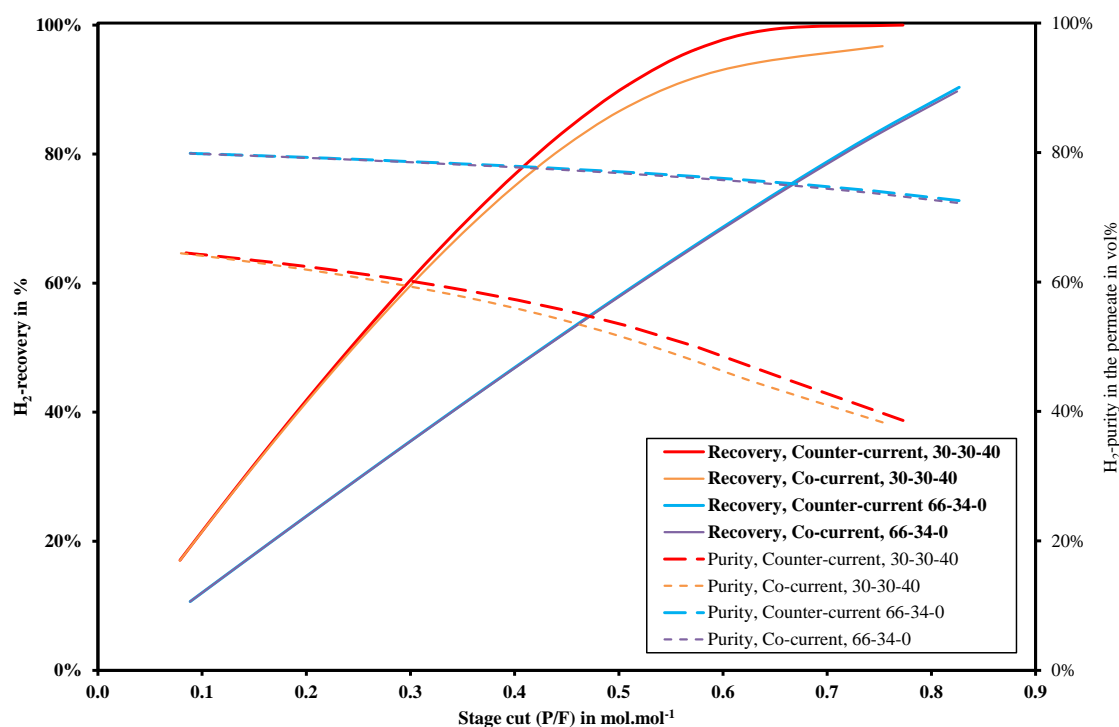


Figure 6.18: Simulation results of H₂-recovery and H₂-purity depending on the stage cut for binary and ternary feed gas mixtures; Comparison of counter-current and co-current operational mode

All four trends indicate that the utilization of a counter-current operational mode should result in a better performance of the membrane module. For the binary feed gas mixture the differences in purity, as well as in recovery, were marginally. Apparently, for the ternary feed gas mixture, with lower hydrogen content and containing a slow permeating component, the utilization of a counter-current operational mode was favorable. Figure 6.18 shows slightly higher H₂-purity and H₂-recovery for the counter-current setup compared to the co-current setup. The graph further shows, that with decreasing stage cut the difference between counter-current and co-current results also decreased.

Figure 6.19 presents permeate's H₂-purity with respect to the H₂-recovery. As mentioned before, the bigger difference between counter- and co-current was found for the ternary mixture. With regard to the ternary feed-gas mixture, it was detected that the gap between co- and counter-current results increased with increasing H₂-recovery. Concerning the binary gas mixture, a similar trend was found but the difference was by far not that severe.

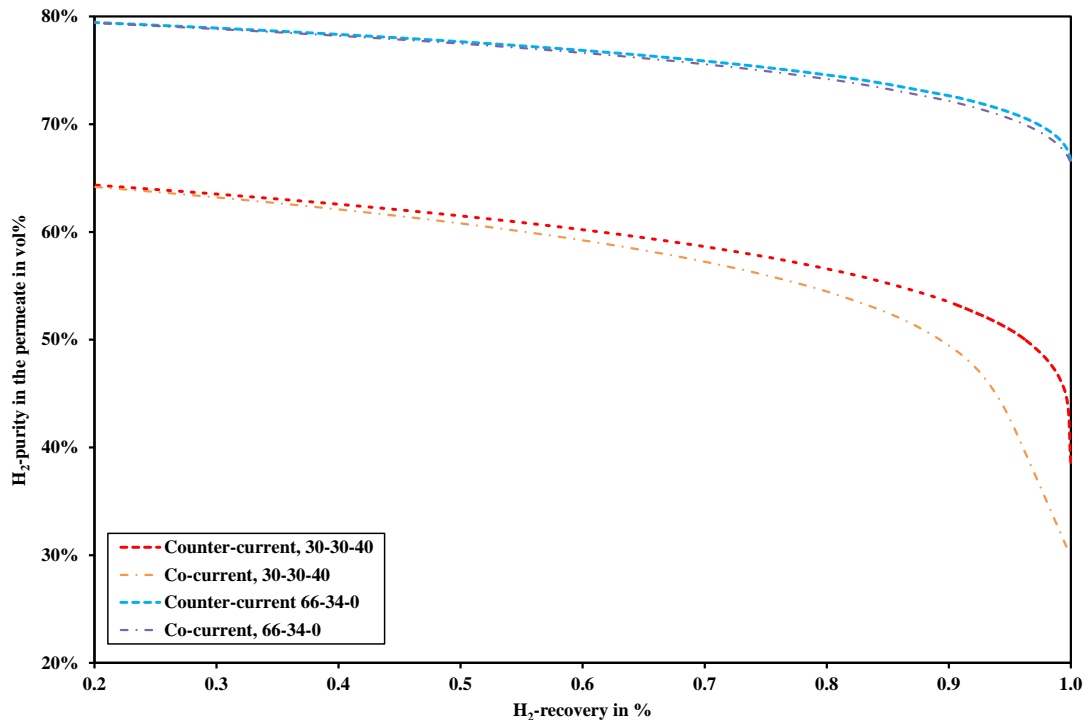


Figure 6.19: Simulation results for the correlation between H₂-purity in the permeate and H₂-recovery for binary and ternary feed gas mixtures; Comparison of counter-current and co-current operational mode

The graphs in Figure 6.19 further depict the trade-off between product purity and hydrogen recovery. The simulation results confirmed the expected trend of purity decline with increasing recovery. Considering the sensitivity results, for both gas mixtures the utilization of a counter-current operational mode was seen as favorable. This mode of operation was therefore chosen for the design and investigation of the multi-stage processes.

6.2.2. Validation of the ACM base case model

The designed ACM base case model was validated in two ways, first via measurement results and second by comparison with the Makaruk&Harasek[®] model, which is a numerical algorithm developed for calculation of permeation systems. In the

three subchapters the validation results are presented, followed by the verification of the ACM detailed model. The verification describes a comparison of the ACM detailed model with CFD modeling results for a specified separation task.

6.2.2.1. Validation via experimental data

To validate the ACM base case model, it was compared with experimental data. This data was taken from laboratory measurements of binary and ternary feed gas mixtures. Figure 6.20 presents the data selected for validation and the corresponding simulation results. This graph shows the H₂-recovery and H₂-purity in the permeate for variable the stage cuts. The values of H₂-recovery predicted by the Aspen model fit very well into the experimental data, within the error limits. The same was found for the prediction of H₂-purity, where the Aspen model reflects the experimental data despite some minor discrepancies from error limits.

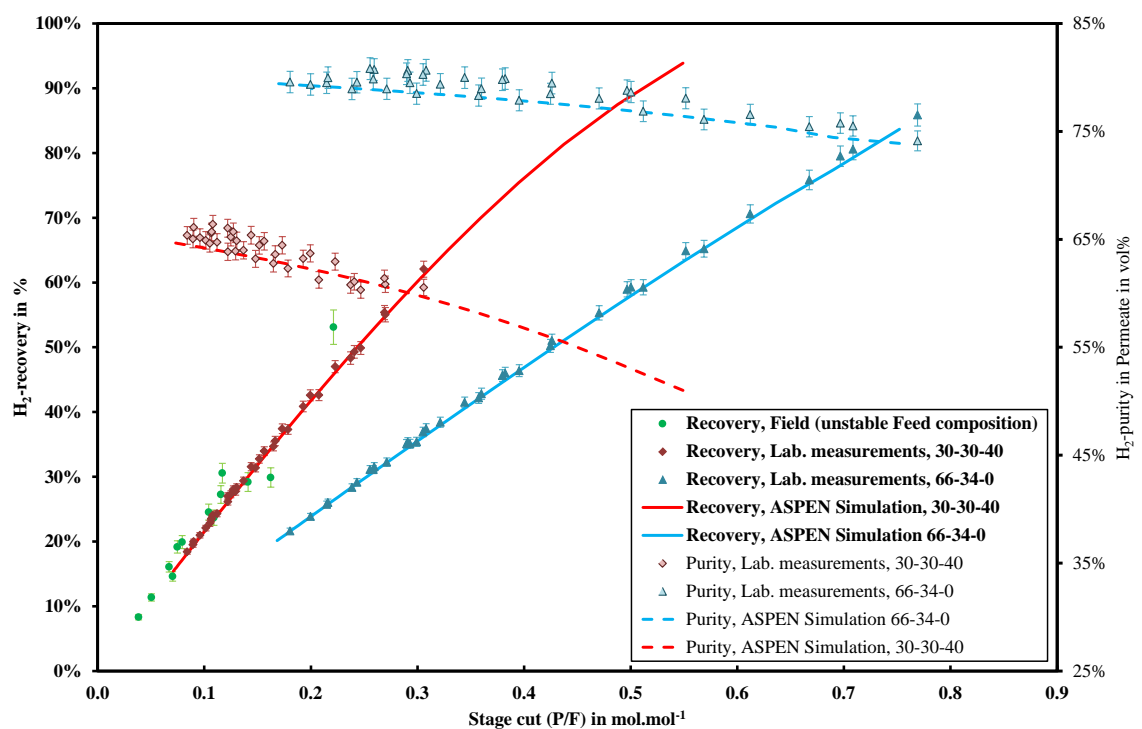


Figure 6.20: Validation of the ACM base case model with measurements

6.2.2.2. Validation due to comparison with Makaruk&Harasek model

For further validation of the ACM model it was compared with a numerical algorithm. Thereto numerous test cases were developed. The resulting findings are listed in Table 6.11. All given deviations were in relation to the calculation results of the Makaruk&Harasek model. It can be seen that the calculations of the two models

deviated in a remarkably low range. The highest difference was 17 ‰ for the membrane area. In this particular test case, a 50 vol% H₂ feed composition was applied at a pressure difference of 10 bar, with a stage cut of 0.5, and a H₂/CO₂ selectivity of 100. All deviations could be attributed to a numerical cut off error during the conversion of molar flow to volume flow at standard conditions. The algorithm used in the Makaruk&Harasek was based on volume flow while the ACM model calculated the transmembrane flow on a molar basis. It was reasonably assumed that the model works properly and can be used for the simulation and investigation of the multi-stage membrane separation processes.

Table 6.11. Deviations of the validation results for comparison with the Makaruk&Harasek model

Resulting validation parameters	Unit	Deviation	
		lower bond	upper bond
Permeate volume flow	Nm ³ /s	-0,0024%	0,0001%
Permeate H ₂ fraction	vol/vol	0,0001%	0,0090%
Retentate volume flow	Nm ³ /s	-0,0001%	0,0011%
Retentate H ₂ fraction	vol/vol	-0,0018%	-0,0006%
Membrane area	m ²	0,0100%	0,0170%

6.2.2.3. Verification of the ACM detailed model by comparison with CFD simulation

To determine the accuracy of the designed ACM detailed model, it was compared with CFD simulation. The respective CFD results were provided by Schretter, P. [pers. comm., 2015]. The defined test cases with varying feed flow rate resulted in an investigated stage cut range between 0.004 and 0.016. Figure 6.21 shows the respective permeate compositions of H₂, CO₂ and N₂ for ACM and CFD calculation over the stage cut. In this graph the highest deviation between the two models accounted for 0.22% and was detected for the N₂ composition in the permeate at a stage cut of 0.005, which refers to a feed gas flow rate of 5.14 L_N/h. With regard to the absolute flows, the highest deviation occurred again at the lowest stage cut. In this case, the hydrogen permeate flow deviated with 0.42%. It was further detected that with increasing stage cut, the deviation between the two models decreased. The trend in Figure 6.21 indicates a constant permeate composition for all components over the considered stage cut range, but this is not the case.

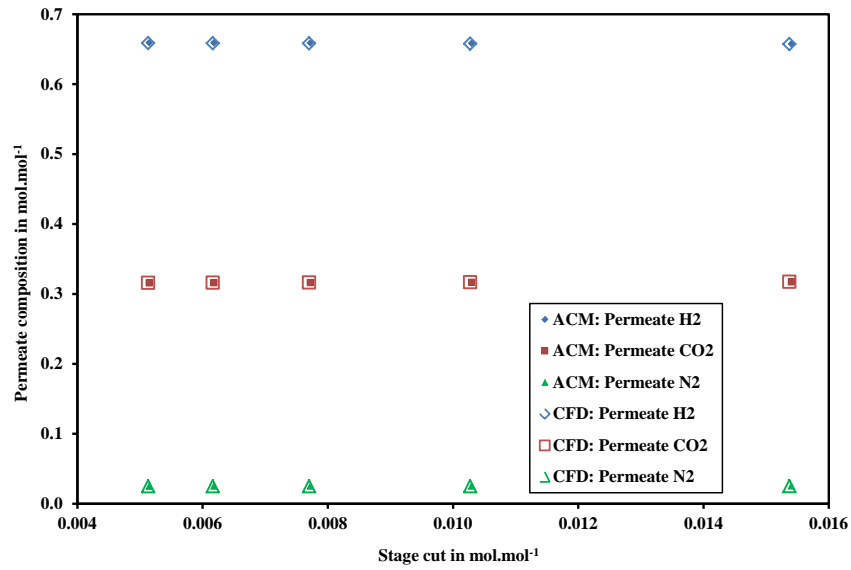


Figure 6.21: Comparison of ACM and CFD results for permeate composition depending on the stage cut

Figure 6.22 points out that the actual trend of H₂ and CO₂ composition in the permeate increases with increasing stage cut. This trend is confirmed by both simulations. Figure 6.22 furthermore shows that the deviation between the two models is not random, as there clearly is a trend visible. The CO₂-composition is under-predicted, while the H₂-composition is over-predicted by the ACM model.

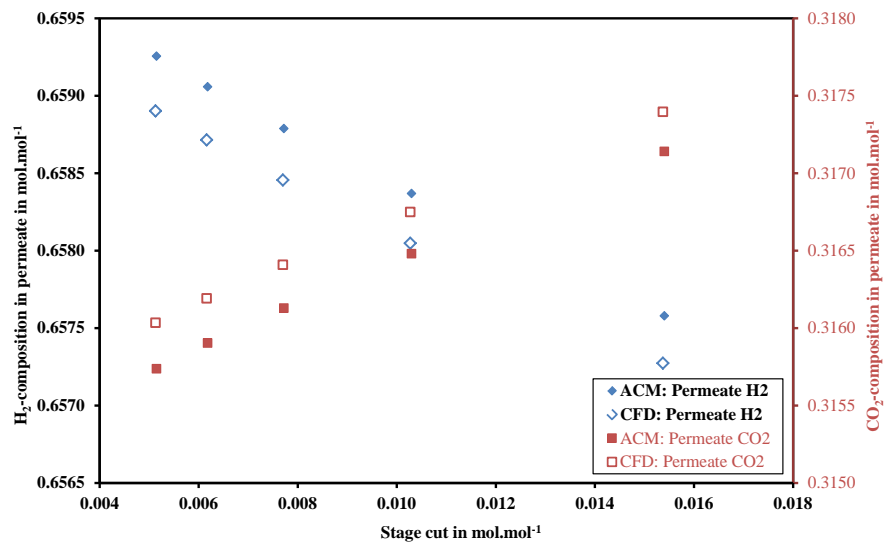


Figure 6.22: Comparison of ACM and CFD results, with detailed look at H₂ and CO₂ composition in the permeate depending on the stage cut

It was noticed that the ACM calculation resulted in higher permeate and retentate volume flow values for all components, even though the feed volume flow was the same. A comparison of both calculations' the global mass balances showed that the ACM model deviated in a range of 0.5% - 0.21% regard permeate and retentate flows. This deviation can be explained by the higher convergence criteria of the ACM model.

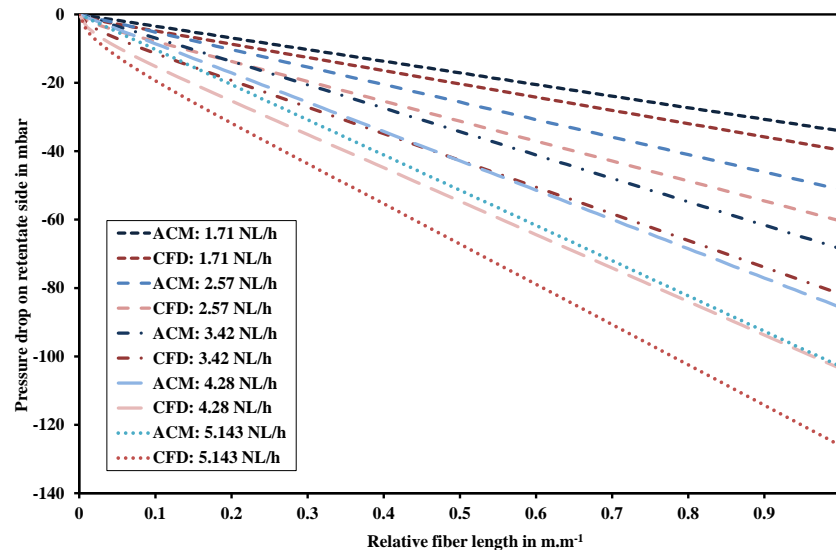


Figure 6.23: Comparison of ACM and CFD results, pressure drop over the fiber length for different gas flows

In Figure 6.23 the pressure drop along the longitudinal axis is pictured. To be able to compare ACM results with CFD modeling, fiber length is represented as a relative value. From the feed entrance at 0 to the retentate exit at 1 a pressure drop increase was detected in both simulations. For all volume flows, the CFD model predicted a higher pressure drop compared to ACM modeling. There was also trend detected, that with increasing feed gas flow the pressure drop difference between ACM and CFD calculation got bigger. This can be explained by the fact that the pressure drop in the CFD model accounts for the local flow profile. Furthermore, CFD calculations consider the expression of a parabolic flow profile in the entry regions. Compared to that, the Hagen-Poiseuille equation in the ACM model is a gross simplification. The occurring concentration polarization in the hollow fiber is also taken into account by the CFD model, which is also in favor of this modeling approach. Figure 6.24 shows the concentration gradient of H_2 inside and outside of the fiber, calculated by the CFD model. The graph on the right side depicts the H_2 concentration inside the hollow-fiber, which has a higher value in the center and decrease towards the fiber wall. This means that the concentration of the residue components increases in radial direction. On the

outside of the fiber which is pictured in the left graph of Figure 6.24, the reverse trend is detected. The H_2 -concentration decreases in with increasing radius.

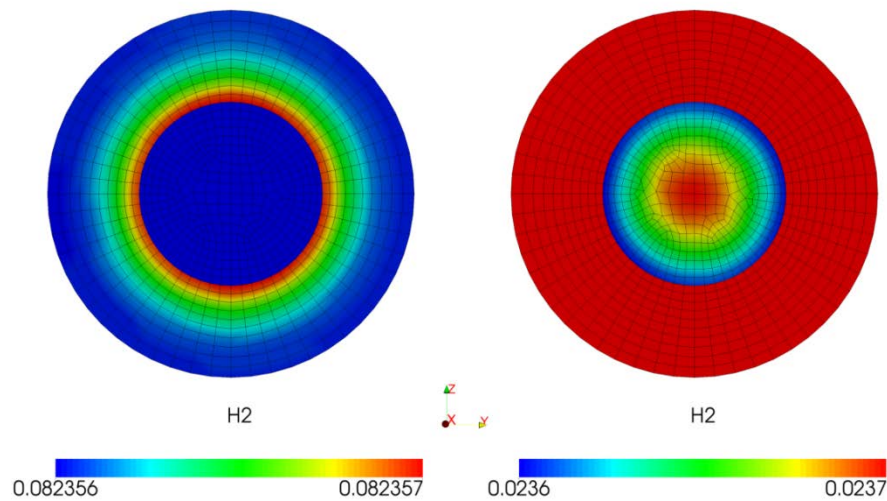


Figure 6.24: CFD results, H_2 concentration gradient outside (left) and inside (right) the fiber

Regarding the verification of the ACM detailed model it can be concluded that the predicted results are similar to the CFD calculations. The ACM pressure drop prediction also worked adequately. CFD applications for modeling of membrane separation processes showed promising results.

6.2.3. Multi-stage

The results for the investigated multi-stage gas permeation processes are presented in the following two subchapters. These include findings from the membrane area variation of different setups, followed by a comparison of all investigated multi-stage configurations.

6.2.3.1. Membrane area variation

For each of the designed multi-stage processes, which are described in chapter 5.2.4, the effect of varying membrane areas was investigated. The sensitivity analysis performed in Aspen Plus[®] showed that setups 1, 2 and 4, all using H_2 -selective membrane material, did not reach the required minimum purity and recovery. When CO_2 -selective membrane material was used, as done in setup 3, the desired purification quality was easily realized. Despite setup 3, the closest values were reached by setup 2. Figure 6.25 pictures the respective area variation results of setup 2 and setup 3. With regard to setup 2 increasing the membrane area A_1 resulted in an increase of H_2 -recovery. However, assuming a constant membrane area A_2 , the H_2 -purity in the

product would decrease. According to the graph for setup 2 in Figure 6.25 it could have been suggested to further increase area A_1 while keeping Area A_2 between 350 and 400 m^2 to reach the targeted product quality. Unfortunately this was not possible, because the maximal size of the membrane areas is restricted by the actual feed gas flow and the recycle to feed ratio. The maximum for the recycle to feed ratio was defined as 0.4, based on practical experience. As mentioned before, using CO_2 -selective membranes showed promising results. Setup 3 showed a similar trend to setup 2, where increasing area A_2 and simultaneously keeping A_1 constant resulted in an elevation of H_2 -purity and H_2 -recovery.

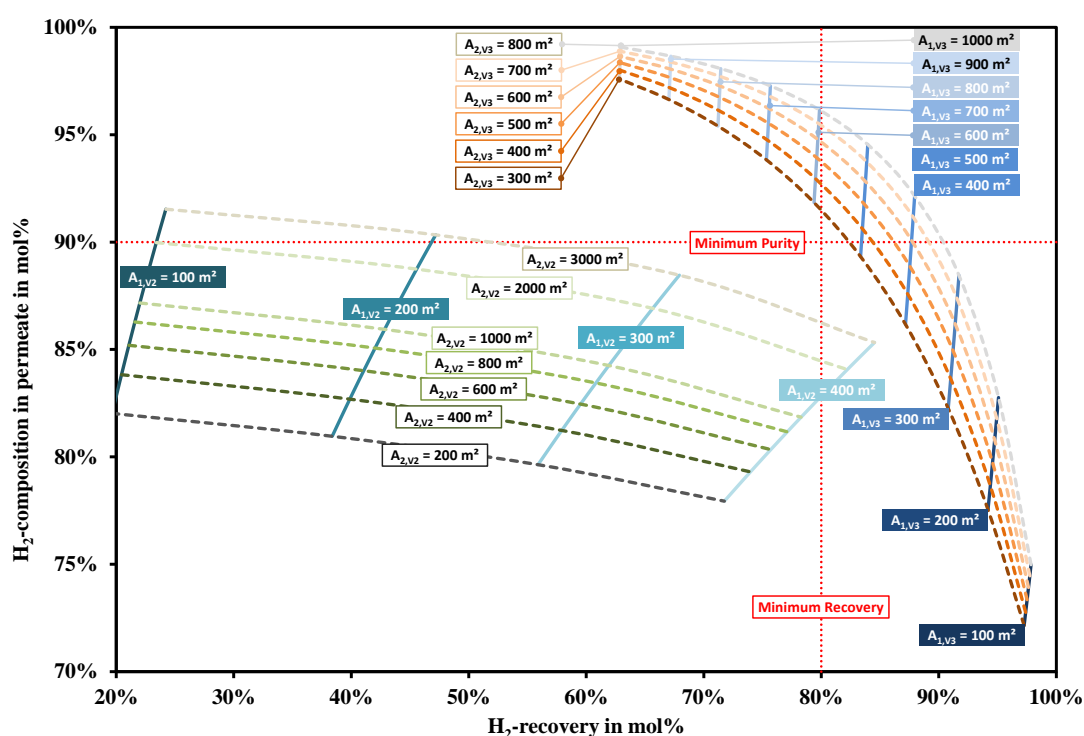


Figure 6.25: Results of the sensitivity analysis with varying membrane areas at stage one (A_1) and two (A_2) for setups 2 and 3.

To further compare the investigated multi-stage setups the H_2 -recovery was set at $80 \pm 1\%$. Aspen Plus[®] was then used to calculate the membrane areas necessary to obtain the highest possible product purity while keeping the recycle to feed ratio below 0.4.

6.2.3.2. Comparison of different setups

Table 6.12 lists the simulation results for the investigated 2-stage setups. The determining factors for comparison were the required membrane area, the possible H_2 -

purity in the product and the specific energy demand. Setup 2 required the smallest membrane area, but showed the lowest product purity. Compared to setup 1, the specific energy demand was also in favor of setup 2. It is therefore questionable if the fairly higher product purity obtained in setup 1 justifies additional expenses in equipment and membrane area. However, the utilization of CO₂-selective membrane material in setup 3 showed several advantages. Among these were a possible H₂-product purity of 95.5 vol% and the lowest specific energy demand among the investigated 2-stage setups. The only drawback was found for the required membrane area. But this could be compensated by utilizing CO₂-selective material with higher permeances.

Table 6.12: Comparison of the investigated setups with a fixed H₂-recovery

	Unit	Values		
		Setup 1	Setup 2	Setup 3
Membrane type		H ₂ -selective	H ₂ -selective	CO ₂ -selective
Number of compressors		2	1	1
Compressor 1	kW	121.7	170.4	160.3
Compressor 2	kW	120.5	-	-
Membrane area A ₁	m ²	736	451	595
Membrane area A ₂	m ²	427	287	715
H ₂ -Recovery	vol%	80.0%	79.9%	80.5%
H ₂ -Purity in product	vol%	79.9%	77.4%	95.5%
Recycle to Feed ratio	-	0.393	0.4	0.319
Specific energy demand	kWh/Nm ³ H ₂	0.463	0.315	0.296

In chapter 6.1.2 the investigated membrane material showed better performance at elevated temperature. Hence, the effect of an operational temperature increase to 80 °C on the performance of setup 1 and 2 was also investigated. Table 6.13 lists the respective results. At higher temperature setup 2 still required less membrane area, resulted in a lower specific energy demand and lower H₂-purity. A comparison of the 80 °C and 30 °C results for the respective setups showed improvements in membrane area and product purity for the processes at elevated temperature. The specific energy demand was also improved. However, it is important to mention that the required energy to heat the system at 80°C was not considered. The simulation estimated a heat demand for feed gas temperature elevation of approximately 22 kW in all setups. A possibility to provide the necessary low temperature heat could be via process integration. As mentioned before, an operational temperature increase had severe effects on the required amount of membrane area. For setups 1 and 2 the membrane area was reduced by 46% and 43%, respectively.

Table 6.13: Comparison of the investigated setups 1 and 2 at an operational temperature of 80°C and with fixed H₂-recovery

	Unit	Values	
		Setup 1 (80 °C)	Setup 2 (80 °C)
Compressor 1	kW	121.7	170.4
Compressor 2	kW	120.5	-
Membrane area A ₁	m ²	391	254
Membrane area A ₂	m ²	241	165
H ₂ -Recovery	vol%	80.0%	80.0%
H ₂ -Purity in product	vol%	80.3%	78.1%
Recycle to Feed ratio	-	0.325	0.4
Specific energy demand	kWh/Nm ³ _{H₂}	0.447	0.315

Additionally to the already discussed 2-stage processes, a 3-stage configuration was also investigated. Table 6.14 lists the results regarding setup 4 operated at 30°C. Compared to setups 1 and 2, the addition of a third membrane stage resulted in an improvement of total membrane area, slightly higher product purity and a lower specific energy demand. Furthermore, a reduction of recycle to feed ratio was also detected. With regard to the specific energy demand, setup 4 reached an even lower value than setup 3.

Table 6.14: Results of the investigated setup 4 with a fixed H₂-recovery

	Unit	Values
		Setup 4
Compressor 1	kW	33.7
Compressor 2	kW	105.2
Membrane area A ₁	m ²	240
Membrane area A ₂	m ²	426
Membrane area A ₃	m ²	105
H ₂ -Recovery	vol%	80.0%
H ₂ -Purity in product	vol%	80.0%
Recycle to Feed ratio	-	0.137
Specific energy demand	kWh/Nm ³ _{H₂}	0.256

Concluding this chapter, among all investigated configurations setup 3 showed the most fitting qualities for bio-hydrogen purification with membrane technology. In particular the high product purity was a decisive argument in favor of setup 3. If the utilization of H₂-selective membrane material were a prerequisite, setup 4 would be the best choice. However, it is important to mention that the possible utilization scenarios for the carbon dioxide rich off-gas as well as techno-economic results also need to be considered. The off-gas utilization will be addressed in the next chapter.

6.2.4. Utilization of the off-gas

Thermal utilization of the off-gas' energy content was determined to be the only eligible practical approach. This approach was applied to all 4 multi-stage setups and Table 6.15 summarizes the relevant technical parameters required for combustion. These parameters are the respective calorific values, lower heating values, relative densities, upper/lower Wobbe indices, and the upper/lower flammability limits.

Table 6.15: Combustion parameters of the off-gas stream in various setups

	Unit	Setup 1	Setup 2	Setup 3	Setup 4
Calorific value	MJ/Nm ³	4.836	6.037	3.407	5.335
Lower heating value	MJ/Nm ³	4.091	5.108	2.883	4.514
Relative density	-	0.968	0.834	1.117	1.117
Upper Wobbe index	MJ/Nm ³	4.91	6.61	3.22	5.047
Lower Wobbe index	MJ/Nm ³	4.16	5.59	2.73	4.270
Upper flammable limit	vol%	65.8	66.7	64.1	66.1
Lower flammable limit	vol%	10.1	7.8	15.3	9.8

Source: [Bjerketvedt et al.2013].

The highest calorific value and the widest flammability range could be found in setup 2. This is a result of the higher hydrogen content in the off-gas due to the lowest product purity, compared to the remaining setups. Consequently, the lowest calorific value and narrowest flammability range was found for the off-gas from setup 3. Even though the flammability limits for the various process setups differed, flammable gas mixtures could be produced for all four setups. The off-gases were therefore determined to be suitable for all variations of conventional thermal utilization, for example the combustion in a gas boiler with a hydrogen burner or cogeneration with a hydrogen-compatible gas engine. Based on the given data, it was determined that lean gas technologies were not necessary to be considered. In order to estimate which recovery method for the particular process setup may be advantageous, the combustion heat

output of the gas streams and therefrom decoupled electrical and thermal performance were calculated. The respective results are presented in Table 6.16.

Table 6.16: Output of the combustion heat of the off-gas stream in different setups as well as decoupled electric and thermic power

	Unit	Setup 1	Setup 2	Setup 3	Setup 4
Calorific value	kW	440.8	708.3	433.9	523.2
Lower heating value	kW	372.9	599.3	367.1	442.7
Pure heat extraction (only high	kW	317.0	509.4	312.0	376.3
Pure heat extraction (incl. low	kW	418.7	672.9	412.2	497.1
CHP electric (Gas motor)	kW	176.3	283.3	173.6	209.3
CHP thermic (only high temp.	kW	224.8	361.3	221.3	298.3
CHP thermic (incl. low temp.	kW	251.2	403.8	247.3	266.9

Assumptions: electric efficiency of the gas engine in the combined heat and power (CHP) unit 40% ,thermal efficiency of the high temperature heat utilization 85%, thermic efficiency of the low temperature heat utilization 95%

Based on the technical parameters presented in Table 6.16 it is apparent that in all 4 setups a CHP engine with hydrogen optimization could be used. The following cogeneration units would be required, for setups 1 and 3 a 175kW-class, for setup 2 a 300kW-class, and for setup 4 a 200kW-class. The first two categories represent a relatively small power range, but there are several manufacturers for related units on the market. Compared to that, CHPs with a capacity of 300kW are industry standard.

7. Summary and conclusion

In this work, the applicability of commercially available membrane materials for the purification of fermentatively produced hydrogen was investigated. Thereto two different approaches were applied, an experimental and a simulative approach. During experimental work three PI and one PP hollow fiber membrane modules were built and investigated in the laboratory. Thereto pure gases of H₂, CO₂ and N₂, and two different gas mixtures were applied. The respective binary (66/34/0) and ternary (30/30/40) gas mixtures contained 66 vol% H₂, 34 vol% CO₂ and 30 vol% H₂, 30 vol% CO₂ 40 vol% N₂. The experimental work showed reasonable results for the PI membrane modules during pure gas measurements, with ideal H₂/CO₂ selectivities in the range of 3.45 to 3.91. Hence, when using PP membrane material an ideal H₂/CO₂ selectivity of 2.7 could never be surpassed. This low value made a further investigation of PP irrelevant. During purification measurements with gas mixtures a selectivity decrease was detected. Depending on the composition of the feed gas, whether it was a binary or ternary mixture, the respective H₂/CO₂ selectivities were in the range of 2.29 - 2.49 or 2.43 - 2.7. These values indicate the severity secondary components can have on a purification task. The investigation with mixed gases further showed that there was a trade-off between H₂-purity and H₂-recovery in the product stream. With increasing stage-cut, the H₂-purity decreased whereas the H₂-recovery increased. For both gas mixtures certain maximum product purities were detected, which were depending on the applied operational conditions. With the 66/34/0-mixture a maximal H₂-purity was reached at 82 vol%. Compared to this, purifying the 30/30/40-mixture resulted in a maximal H₂-purity of 67 vol%. A distinct linear correlation was found for all investigated membrane modules, confirming a temperature dependency of the respective permeances according to the Arrhenius approach. The resulting estimation performance parameters at 80 °C showed that the permeances would be tripled going along with a slight increase in H₂/CO₂ selectivity. This allows higher trans-membrane flows at a similar separation rate, which would be in favor of an overall process. The laboratory results were further used for comparison with a theoretical approach. This approach is commonly used to estimate the permeate composition based on known permeances and feed gas composition. For all investigated conditions the theoretical calculation overestimated the purification performance. Therefore, this approach should only be used for a first rough estimation. During the course of the experimental work, a mobile small-scale pilot plant was designed, built and connected to a fermenter system with the purpose to use the membrane modules for online gas cleaning. During these field tests the biggest challenges for fermentative hydrogen purification were detected in the fermentation sector. Stable operation conditions were hardly reached, which also resulted in unstable purification performance. Still, the measurements were successfully executed and confirmed the findings from laboratory experiments. Overall, the experimental work

showed that an actual online fermenter gas upgrading is possible. However, the measurement results from laboratory and field tests displayed that the commercially available H₂-selective membrane material is a limiting factor, especially when using a single stage setup for hydrogen purification. The low H₂/CO₂-selectivity of the polyimide makes it impossible to reach the targeted H₂-purity with the corresponding H₂-recovery.

The second approach was the simulative investigation of commercially available H₂-selective membrane material. Thereto, a gas permeation unit operation was developed using the modelling tool Aspen Custom Modeler[®] (ACM), which simulated the occurring processes in a membrane module depending on the operational mode. This ACM base case model was then further used to investigate the performance of H₂-selective membrane modules in a multi-stage purification process. Validation of the developed ACM single-stage unit operation with measurement results confirmed the model's accuracy and its applicability in a multi-stage configuration. Comparison with calculation results from a numerical algorithm especially designed for multipermeator systems, designated as the Makaruk&Harasek model, further confirmed the correctness of the ACM base case model. Investigation concerning the influence of various parameters, such as number of cells or operational mode, showed that a 100 cell model results in a sufficient accuracy while converging for any given feed composition and flow. Regarding different operational modes, sensitivity analysis showed that the counter-current configuration is favorable. Additionally to the base case model, a detailed model was developed which considers the pressure drop in the hollow fibers. A comparison with CFD modeling resulted in promising findings, as the deviation between the ACM detailed model and CFD calculations was below 0.5%. The design of different multi-stage processes in Aspen Plus[®] was used to determine the most effective and economic separation setup. Implementing a second (setups 1 and 2) and third stage (setup 4) into the process increased the H₂-recovery compared to a single-stage configuration. But still, when using H₂-selective membranes the achievable product quality was limited. This makes a subsequent purification step inevitable. Operation under elevated temperature resulted in a reduction of membrane area and recycle to feed ratio, but barely had an effect on the product purity. Compared to setups 1 and 2, the utilization of CO₂-selective membranes (setup 3) reached the required product purity of at least 98 vol%, accompanied by a lower specific energy demand. All in all, to be able to purify fermentatively produced hydrogen to a gas quality applicable in internal combustion engines, CO₂-selective material seems more promising. A further development of PI membranes concerning H₂/CO₂-selectivity would be necessary to make them suitable. With disregard to the respective setups' applicability, the off-gas utilization gave an insight into the available unused energy potential. For all four multi-stage setups, it was shown that a thermal utilization of the off-gas' energy content could

provide a significant amount of heat and power. This surplus power could then be integrated into the process to improve the overall efficiency.

In conclusion, this thesis showed that the utilization of commercially available membrane material has its possibilities but also its restrictions. Laboratory tests and online gas purification were carried out successfully, giving an extensively insight into the membrane behavior under various conditions. The development of membrane models in ACM, as well as the implementation and utilization in Aspen Plus[®] led to important findings. Furthermore, a data reconciliation tool was also successfully developed and applied.

8. Outlook

The application of membrane processes for the purification of fermentatively produced hydrogen is a promising pathway. To further develop the overall concept research regarding the optimization of the fermentation as well as membrane purification is necessary. The commercialization of CO₂-selective material would therefore be a big step towards a better membrane purification concept. Another important factor for the optimization of the process is the development regarding simulation. There are several upsides going along with the simulation of the separation mechanism. Inter alia, it gives a better insight into the important factors of the concept and enables a fast and save estimation of a given purification task. It is therefore important to not only improve the accuracy and reliability of the developed models, but also further develop a more sophisticated mass transfer model. With respect to the ACM simulation, future work might focus on the improvement of the membrane model considering effects, such as flux coupling and dual sorption. Accounting the effects regarding plasticization as well as heat would result in a better performance prediction. Furthermore, implementing a shell-side feed application would make the ACM model more versatile and applicable for various purification tasks. As CFD simulation showed promising results, a further improvement in this field could lead to important findings.

REFERENCES

- Adhikari, S. and Fernando, S., 2006. Hydrogen Membrane Separation Techniques. *Industrial & Engineering Chemistry Research*, 45(3), 875-881.
- Al-Shorgani, N.K.N., Tibin, E.-M., Ali, E., Hamid, A.A., Yusoff, W.M.W. and Kalil, M. S., 2013. Biohydrogen production from agroindustrial wastes via *Clostridium saccharoperbutylacetonicum* N1-4 (ATCC 13564). *Clean Technologies and Environmental Policy*, 16(1), 11-21.
- Allakhverdiev, S.I., Thavasi, V., Kreslavski, V.D., Zharmukhamedov, S.K., Klimov, V.V.; Ramakrishna, S., Los, D.A.; Mimuro, M., Nishihara, H. and Carpentier, R., 2010. Photosynthetic hydrogen production *Journal of Photochemistry and Photobiology C: Photochemistry Reviews*, 11, 101-113.
- Alves, H.J. et al., 2013. Overview of hydrogen production technologies from biogas and the applications in fuel cells. *International Journal of Hydrogen Energy*, 38(13), 5215-5225.
- Azwar, M.Y., Hussain, M.A. and Abdul-Wahab, A.K., 2014. Development of biohydrogen production by photobiological, fermentation and electrochemical processes: A review. *Renewable and Sustainable Energy Reviews*, 31, 158-173.
- Baker, R.W., 2012. Membrane Technology and Applications. 3rd Edition, John Wiley & Sons.
- Balat, H. and Kirtay, E., 2010. Hydrogen from biomass – Present scenario and future prospects. *International Journal of Hydrogen Energy*, 35(14), 7416-7426.
- Ball, M. and Weeda, M., 2015. The hydrogen economy – Vision or reality?. *International Journal of Hydrogen Energy*, 40(25), 7903-7919.
- Bartels, J.R., Pate, M.B. and Olson, N.K., 2010. An economic survey of hydrogen production from conventional and alternative energy sources. *International Journal of Hydrogen Energy*, 35(16), 8371-8384.
- Barthélémy, H., 2012. Hydrogen storage – Industrial perspectives. *International Journal of Hydrogen Energy*, 37(22), 17364-17372.
- Bjerketvedt D., Bakke, J.R., Van Wingerden, K., 1997. Gas explosion handbook, *Journal of Hazardous Materials*, 52, 1-150.

-
- Borhani, T.N.G., Azarpour, A., Akbari, V., Wan A., Sharifah R. and Manan, Z.A., 2015. CO₂ capture with potassium carbonate solutions: A state-of-the-art review. *International Journal of Greenhouse Gas Control*, 41, 142-162.
- Bos, A., Pünt, I.G.M., Wessling, M. and Strathmann, H., 1999. CO₂-induced plasticization phenomena in glassy polymers. *Journal of Membrane Science*, 155(1), 67-78.
- Bulatov, I. and Klemeš, J.J., 2011. Clean fuel technologies and clean and reliable energy: a summary. *Clean Technologies and Environmental Policy*, 13(4), 543-546.
- California Department of Food and Agriculture, 2008. Specifications for hydrogen used in internal combustion engines and fuel cells. *California Code of Regulations Title 4, Division 9, (Chapter 6), Article 8*. U.S.A.
- Car, A., Stropnik, C., Yave, W. and Peinemann, K.-V., 2008. Pebax® polyethylene glycol blend thin film composite membranes for CO₂ separation: Performance with mixed gases. *Separation and Purification Technology*, 62(1), 110-117.
- Cecere, D., Giacomazzi, E. and Ingenito, A., 2014. A review on hydrogen industrial aerospace applications. *International Journal of Hydrogen Energy*, 39(20), 10731-10747.
- Chaubey, R., Sahu, S., James, O.O. and Maity, S., 2013. A review on development of industrial processes and emerging techniques for production of hydrogen from renewable and sustainable sources. *Renewable and Sustainable Energy Reviews*, 23, 443-462.
- Claassen, P.A.M., de Vrije, T., Koukios, E.G., van Niel, E.W.J., Eroglu, I., Modigell M., Friedl, A., Wukovits, W., Ahrer, W., 2010. Non-thermal production of pure hydrogen from biomass: HYVOLUTION. *Journal of Cleaner Production*, doi:10.1016/j.jclepro.2010.05.009.
- Dalebrook, A.F., Gan, W., Grasemann, M., Moret, S. and Laurency, G., 2013. Hydrogen storage: beyond conventional methods. *Chemical Communications*, 49, 8735-8751.
- David, O. C., Gorri, D., Urriaga, A. and Ortiz, I., 2011. Mixed gas separation study for the hydrogen recovery from H₂/CO/N₂/CO₂ post combustion mixtures using a Matrimid membrane. *Journal of Membrane Science*, 378(1-2), 359-368.
- de Vrije, T., Claassen, P.A.M., 2003. Dark hydrogen fermentations. In Reith, J.H., Wijffels, R.H., Barten, H. (Eds.), *Bio-methane & Bio-hydrogen. Status and*
-

-
- perspectives of biological methane and hydrogen production*, Smiet offset, The Hague, 103-123.
- Dincer, I. and Acar, C., 2015. Review and evaluation of hydrogen production methods for better sustainability. *International Journal of Hydrogen Energy*, 40(34), 11094-11111.
- Duic, N., 2015. Is the success of clean energy guaranteed?. *Clean Technologies and Environmental Policy*, 17(8), 2093-2100.
- Duthie, X., Kentish, S., Powell, C., Nagai, K., Qiao, G. and Stevens, G., 2007. Operating temperature effects on the plasticization of polyimide gas separation membranes. *Journal of Membrane Science*, 294(1-2), 40-49.
- Ehret, O. and Bonhoff, K., 2015. Hydrogen as a fuel and energy storage: Success factors for the German Energiewende. *International Journal of Hydrogen Energy*, 40(15), 5526-5533.
- Foglia, D., Ljunggren, M., Wukovits, W., Friedl, A., Zacchi, G., Urbaniec, K. and Markowski, M., 2010a. Integration studies on a two-stage fermentation process for the production of biohydrogen. *Journal of Cleaner Production*, 18(1), 72-80.
- Foglia, D., Rodrigues, D., Wukovits, W. and Friedl, A., 2010b. Model Development of a Membrane Gas Permeation Unit for the Separation of Hydrogen and Carbon Dioxide. *Chemical Engineering Transactions*, 21.
- Foglia, D., Wukovits, W., Friedl, A., Ljunggren, M., Zacchi, G., Urbaniec, K. and Markowski, M., 2011. Effects of feedstocks on the process integration of biohydrogen production. *Clean Technologies and Environmental Policy*, 13(4), 547-558.
- Gahleitner, G., 2013. Hydrogen from renewable electricity: An international review of power-to-gas pilot plants for stationary applications. *International Journal of Hydrogen Energy*, 38(5), 2039-2061.
- Ghimire, A., Frunzo, L., Pirozzi, F., Trably, E., Escudie, R., Lens, P.N.L. and Esposito, G., 2015. A review on dark fermentative biohydrogen production from organic biomass: Process parameters and use of by-products. *Applied Energy*, 144, 73-95.
- Götz, M., Lefebvre, J., Mörs, F., McDaniel Koch, A., Graf, F., Bajohr, S., Reimert, R. and Kolb, T., 2016. Renewable Power-to-Gas: A technological and economic review. *Renewable Energy*, 85, 1371-1390.
-

-
- Graham, T., 1863. On the Molecular Mobility of Gases. *Philosophical Transactions of the Royal Society of London*, 153, 385-405.
- Gupta, R. B., 2008. Hydrogen Fuel: Production, Transport, and Storage. Boca Raton, FL: CRC Press, Taylor and Francis Group, LLC.
- Haddadi, B., Jordan, C., Schretter, P., Lassmann, T. and Harasek, M., 2015, November. Designing Better Membrane Modules Using CFD. Presentation at the 12th International Conference on Membrane Science & Technology, Teheran, Iran.
- Haddadi, B., Jordan, C., Schretter, P., Lassmann, T. and Harasek, M., 2016, Designing Better Membrane Modules Using CFD. *Journal of Chemical Product and Process Modeling*, manuscript accepted for publication.
- Hallenbeck, P.C., 2013. Chapter 2 - Fundamentals of Biohydrogen; in: *Biohydrogen*. Amsterdam: Elsevier, 25-43.
- Hallenbeck, P.C., 2013. Chapter 7 - Photofermentative Biohydrogen Production; in: *Biohydrogen*. Amsterdam: Elsevier, 145-159.
- He, G., Mi, Y., Yue, P.L. and Chen, G., 1999. Theoretical study on concentration polarization in gas separation membrane processes. *Journal of Membrane Science*, 153(2), 243-258.
- Holladay, J., Hu, J., King, D. and Wang, Y., 2009. An overview of hydrogen production technologies. *Catalysis Today*, 139(4), 244-260.
- IPCC, 2007. IPCC Fourth Assessment Report, *Climate Change 2007 (AR4)*. C/O World Meteorological Organization.
- Kalamaras, C.M. and Efstathiou, A.M., 2013. Hydrogen Production Technologies: Current State and Future Developments. *Conference Papers in Science*, 690-627.
- Kanehashi, S., Tsutomu N., Kazukiyo N., Xavier D., Sandra K. and Geoff S., 2007. Effects of carbon dioxide-induced plasticization on the gas transport properties of glassy polyimide membranes. *Journal of Membrane Science*, 298(1-2), 147-155.
- Kenarsari, S.D., Yang, D., Jiang, G., Zhang, S., Wang, J., Russell, A.G., Wei, Q and Fan, M., 2013. Review of recent advances in carbon dioxide separation and capture. *RSC Advances*, 3(45), 22739-22773.
-

-
- Kohl, A.L. and Nielsen, R.B., 1997a. Chapter 6 - Water as an Absorbent for Gas Impurities; in: *Gas Purification*, Fifth Edition. Houston: Gulf Professional Publishing, 415-465.
- Kohl, A.L. and Nielsen, R.B., 1997b. Chapter 14 - Physical Solvents for Acid Gas Removal; in: *Gas Purification*, Fifth Edition. Houston: Gulf Professional Publishing, 1187-1237.
- Kohl, A.L. and Nielsen, R.B., 1997c. Chapter 5 - Alkaline Salt Solutions for Acid Gas Removal; in: *Gas Purification*, Fifth Edition. Houston: Gulf Professional Publishing, 330-414.
- Kothari, R., Buddhi, D. and Sawhney, R., 2008. Comparison of environmental and economic aspects of various hydrogen production methods. *Renewable and Sustainable Energy Reviews*, 12(2), 553-563.
- Kötter, E. Schneider, L., Sehnke, F., Ohnmeiss, K. and Schröer, R., 2015. Sensitivities of power-to-gas within an optimised energy system. *Energy Procedia*, 73, 190-199.
- Lassmann, T. Miltner, M., Harasek, M., Makaruk, A., Wukovits, W. and Friedl, A., 2015. The purification of fermentatively produced hydrogen using membrane technology: a simulation based on small-scale pilot plant results. *Clean Technologies and Environmental Policy*, 1-8; published online, Doi: 10.1007/s10098-015-0997-7.
- Lay, C.-H.; Wu, J.-H.; Hsiao, C.-L.; Chang, J.-J.; Chen, C.-C. and Lin, C.-Y. , 2010. Biohydrogen production from soluble condensed molasses fermentation using anaerobic fermentation. *International Journal of Hydrogen Energy*, 35, 13445-13451.
- Ling, J. Ntiamoah, A., Xiao, P., Webley, P.A. and Zhai, Y., 2015. Effects of feed gas concentration, temperature and process parameters on vacuum swing adsorption performance for CO₂ capture. *Chemical Engineering Journal*, 265, 47-57.
- Li, P. Wang, Z., Qiao, Z., Liu, Y., Cao, X., Li, W., Wang, J. and Wang, S, 2015. Recent developments in membranes for efficient Hydrogen purification. *Journal of Membrane Science*, 495, 130-168.
- Lüdtke, O., Behling, R. D. and Ohlrogge, K., 1998. Concentration polarization in gas permeation. *Journal of Membrane Science*, 146(2), 145-157.
-

-
- Makaruk, A. and Harasek, M., 2009. Numerical algorithm for modelling multicomponent multipermeator systems. *Journal of Membrane Science*, 344(1-2), 258-265.
- Makaruk, A., Miltner, M. and Harasek, M., 2011. Membrane systems for the recovery of hydrogen from multicomponent gas mixtures obtained in biomass gasification. *Chemical Engineering Transactions*, 25, 833-838.
- Makaruk, A., Miltner, M. and Harasek, M., 2012. Membrane gas permeation in the upgrading of renewable hydrogen from biomass steam gasification gases. *Applied Thermal Engineering*, 43, 134-140.
- Mansour, M. and Ellis, J.E., 2008. Methodology of on-line optimisation applied to a chemical reactor. *Applied Mathematical Modelling*, 32(2), 170-184.
- Marchenko, O.V. and Solomin, S.V., 2015. The future energy: Hydrogen versus electricity. *International Journal of Hydrogen Energy*, 40(10), 3801-3805.
- Miltner, A., Wukovits, W., Pröll, T. and Friedl, A., 2010. Renewable hydrogen production: a technical evaluation based on process simulation. *Journal of Cleaner Production*, 18, 51 – 62.
- Mohan, S.V. and Pandey, A., 2013. Chapter 1 - Biohydrogen Production: An Introduction; in: *Biohydrogen*. Amsterdam: Elsevier, 1-24.
- Mondal, M.K., Balsora, H.K. and Varshney, P., 2012. Progress and trends in CO₂ capture/separation technologies: A review. *Energy*, 46(1), 431-441.
- Mourgues, A. and Sanchez, J., 2005. Theoretical analysis of concentration polarization in membrane modules for gas separation with feed inside the hollow-fibers. *Journal of Membrane Science*, 252(1-2), 133-144.
- Murad Chowdhury, M.H., Feng, X., Douglas, P. and Croiset, E., 2005. A New Numerical Approach for a Detailed Multicomponent Gas Separation Membrane Model and Aspen Plus Simulation. *Chemical Engineering & Technology*, 28(7), 773-782.
- Muradov, N. Z. and Veziroglu, T. N., 2005. From hydrocarbon to hydrogen-carbon to hydrogen economy. *International Journal of Hydrogen Energy*, 30(3), 225-237.
- Narasimhan, S. and Jordache, C., 1999a. 4 - Steady-State Data Reconciliation for Bilinear Systems; in: *Data Reconciliation and Gross Error Detection*. Burlington: Gulf Professional Publishing, 85-118.
-

-
- Narasimhan, S. and Jordache, C., 1999b. 5 - Nonlinear Steady-State Data Reconciliation; in: *Data Reconciliation and Gross Error Detection*. Burlington: Gulf Professional Publishing, 119-141.
- Niaz, S., Manzoor, T. and Pandith, A. H., 2015. Hydrogen storage: Materials, methods and perspectives. *Renewable and Sustainable Energy Reviews*, 50, 457-469.
- N.C.S.U and U.O., 2003a. Module: Introduction to Data Reconciliation, *Introducing Process Integration for Environmental Control in Engineering Curricula*. North Carolina State University, USA and University of Ottawa, Canada, Online available at:
http://www.polymtl.ca/namp/docweb/Modules_Web/M11_Tier1_Chap1-3.pdf [accessed 7.10.2014].
- N.C.S.U and U.O., 2003b. Module: Introduction to Data Reconciliation, *Introducing Process Integration for Environmental Control in Engineering Curricula*. North Carolina State University, USA and University of Ottawa, Canada, Online available at:
http://www.polymtl.ca/namp/docweb/Modules_Web/M11_Tier1_Chap4-5.pdf [accessed 7.10.2014].
- Olajire, A.A., 2010. CO₂ capture and separation technologies for end-of-pipe applications – A review. *Energy*, 35(6), 2610-2628.
- Padurean, A., Cormos, C.-C. and Agachi, P.-S., 2012. Pre-combustion carbon dioxide capture by gas–liquid absorption for Integrated Gasification Combined Cycle power plants. *International Journal of Greenhouse Gas Control*, 7, 1-11.
- Parthasarathy, P. and Narayanan, K. S., 2014. Hydrogen production from steam gasification of biomass: Influence of process parameters on hydrogen yield – A review. *Renewable Energy*, 66, 570-579.
- Pfeifer, C.; Puchner, B. and Hofbauer, H., 2009. Comparison of dual fluidized bed steam gasification of biomass with and without selective transport of CO₂ *Chemical Engineering Science*, 64, 5073-5083.
- Ramachandran, R. and Menon, R. K., 1998. An overview of industrial uses of hydrogen. *International Journal of Hydrogen Energy*, 23(7), 593-598.
- Ramírez-Morales, J.E., Tapia-Venegas, E., Nemestóthy, N., Bakonyi, P., Bélafi-Bakó, K. and Ruiz-Filippi, G., 2013. Evaluation of two gas membrane modules for fermentative hydrogen separation. *International Journal of Hydrogen Energy*, 38(32), 14042-14052.
-

-
- Ren, N., Jianzheng, L., and Baikun, L., and Yong, W., and Shirui, Liu., 2006. Biohydrogen production from molasses by anaerobic fermentation with a pilot-scale bioreactor system. *International Journal of Hydrogen Energy*, 31(15), 2147-2157.
- Riis, T., Hagen, E.F., Vie, P.J.S. and Ulleberg, Ø., 2006. Hydrogen Production and Storage: RD priorities and gaps. Paris: OECD/IEA.
- Robeson, L.M., 1991. Correlation of separation factor versus permeability for polymeric membranes. *Journal of Membrane Science*, 62, 165 - 185.
- Rodrigues, D., 2009. Model development of a membrane gas permeation unit for the separation of Hydrogen and Carbon Dioxide. Vienna, Vienna University of Technology: Master Thesis.
- Rom, A., Wukovits, W. and Friedl, A., 2014. Development of a vacuum membrane distillation unit operation: From experimental data to a simulation model. *Chemical Engineering and Processing: Process Intensification*, 86, 90-95.
- Saxena, R., Adhikari, D. and Goyal, H., 2009. Biomass-based energy fuel through biochemical routes: A review. *Renewable and Sustainable Energy Reviews*, 13(1), 167-178.
- Schiebahn, S., Grube, T., Robinius, M., Tietze, V. Kumar, B. and Stolten, D., 2015. Power to gas: Technological overview, systems analysis and economic assessment for a case study in Germany. *International Journal of Hydrogen Energy*, 40(12), 4285-4294.
- Scholes, C.A., Smith, K.H., Kentish, S.E. and Stevens, G.W., 2010. CO₂ capture from pre-combustion processes — Strategies for membrane gas separation. *International Journal of Greenhouse Gas Control*, 4(5), 739-755.
- Shao, L., Low, B.T., Chung, T.-S. and Greenberg, A.R., 2009. Polymeric membranes for the hydrogen economy: Contemporary approaches and prospects for the future. *Journal of Membrane Science*, 327(1-2), 18-31.
- Shao, P. and Huang, R.Y.M., 2006. An analytical approach to the gas pressure drop in hollow fiber membranes. *Journal of Membrane Science*, 271(1-2), 69-76.
- Sharma, S. and Ghoshal, S.K., 2015. Hydrogen the future transportation fuel: From production to applications. *Renewable and Sustainable Energy Reviews*, 43, 1151-1158.
-

-
- Show, K.-Y. and Lee, D.-J., 2013. Chapter 13 - Bioreactor and Bioprocess Design for Biohydrogen Production. In Larroche, C.; Pandey, A.; Chang, J.-S. and Hallenbeck, P.C. (Eds.), *Biohydrogen*, Elsevier, 317-337.
- Suleman, F., Dincer, I. and Agelin-Chaab, M., 2015. Environmental impact assessment and comparison of some hydrogen production options. *International Journal of Hydrogen Energy*, 40(21), 6976-6987.
- Tessendorf, S., Gani, R. and Michelsen, M. L., 1999. Modeling, simulation and optimization of membrane-based gas separation systems. *Chemical Engineering Science*, 54(7), 943-955.
- Uddin, M.N. and Daud, W.M.A.W., 2014. Technological Diversity and Economics: Coupling Effects on Hydrogen Production from Biomass. *Energy & Fuels*, 28(7), 4300-4320.
- Urbaniec, K. and Bakker, R.R., 2015. Biomass residues as raw material for dark hydrogen fermentation – A review. *International Journal of Hydrogen Energy*, 40(9), 3648-3658.
- Urbaniec, K., Friedl, A., Huisingh, D. and Claassen, P., 2010. Hydrogen for a sustainable global economy. *Journal of Cleaner Production*, 18(1), 1-3.
- Varone, A. and Ferrari, M., 2015. Power to liquid and power to gas: An option for the German Energiewende. *Renewable and Sustainable Energy Reviews*, 45, 207-218.
- Verhelst, S., 2014. Recent progress in the use of hydrogen as a fuel for internal combustion engines. *International Journal of Hydrogen Energy*, 39(2), 1071-1085.
- Verhelst, S. and Wallner, T., 2009. Hydrogen-fueled internal combustion engines. *Progress in Energy and Combustion Science*, 35(6), 490-527.
- Wang, J. and Wan, W., 2009. Factors influencing fermentative hydrogen production: A review. *International Journal of Hydrogen Energy*, 34(2), 799-811.
- Wang, R., Liu, S.L., Lin, T.T. and Chung, T.S., 2002. Characterization of hollow fiber membranes in a permeator using binary gas mixtures. *Chemical Engineering Science*, 57(6), 967-976.
- Weinert, J.X., 2005. A Near-Term Economic Analysis of Hydrogen Fueling Stations. Davis, University of California: Master Thesis.
-

- Westermann, P., Jørgensen, B., Lange, L., Ahring, B.K. and Christensen, C.H., 2007. Maximizing renewable hydrogen production from biomass in a bio/catalytic refinery. *International Journal of Hydrogen Energy*, 32(17), 4135-4141.
- Wijmans, J.G. and Baker, R.W., 1995. The solution-diffusion model: a review. *Journal of Membrane Science*, 107(1-2), 1-21.
- Wilk, V. and Hofbauer, H., 2016. Analysis of optimization potential in commercial biomass gasification plants using process simulation. *Fuel Processing Technology*, 141, Part 1, 138-147.
- Wind, J.D., Sirard, S.M., Paul, D.R., Green, P.F. Johnston, K.P. and Koros, W.J., 2003. Carbon Dioxide-Induced Plasticization of Polyimide Membranes: Pseudo-Equilibrium Relationships of Diffusion, Sorption, and Swelling. *Macromolecules*, 36(17), 6433-6441.
- Yave, W., Car, A. and Peinemann, K.-V., 2010. Nanostructured membrane material designed for carbon dioxide separation. *Journal of Membrane Science*, 350(1-2), 124-129.
- Zhang, J., Liu, D., He, M., Xu, H. and Li, W., 2006. Experimental and simulation studies on concentration polarization in H₂ enrichment by highly permeable and selective Pd membranes. *Journal of Membrane Science*, 274(1-2), 83-91.
- Zhang, X., Chan, S.H. and Ho, H. K., Tan, S.-C., Li, M., Li, G., Li, J. and Feng, Z., 2015. Towards a smart energy network: The roles of fuel/electrolysis cells and technological perspectives. *International Journal of Hydrogen Energy*, 40(21), 6866-6919.
- Zhang, Z., Wang, Y., Hu, J., Wu, Q. and Zhang, Q., 2015a. Influence of mixing method and hydraulic retention time on hydrogen production through photo-fermentation with mixed strains. *International Journal of Hydrogen Energy*, 40, 6521-6529

Appendix

A. Fermentation

The following is a detailed description of the problems that occurred during the course of fermentation, with the most important events during the course of fermentation presented in Figure A.1 with red malfunction bar.

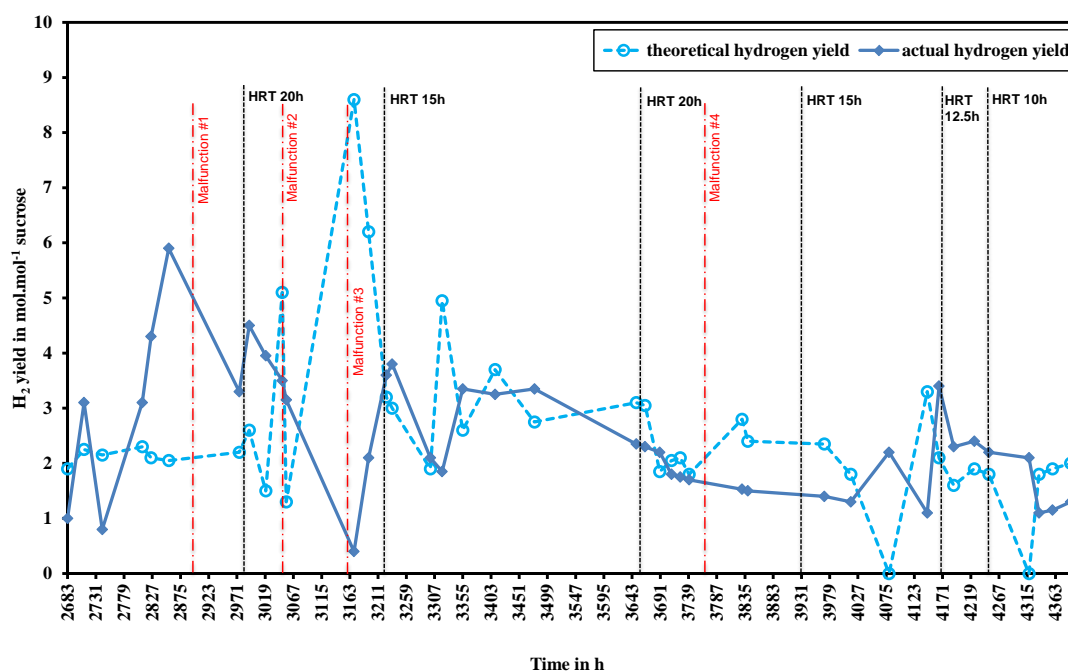


Figure A.1: Fermentation, H₂ yield over course of time, including malfunctions during operation

After the continuous fermentation was well underway, a H₂-productivity of 0.28 L/L/h and an H₂-yield of 5.8 mol/mol sucrose at a residence time of 20 h were achieved. At this time, the fermentation went well, the yield was 75% of the theoretical maximum, and the productivity was very satisfactory.

Malfunction #1: At fermentation time 2900 h an error occurred in the dosage equipment for molasses, which turned to permanent instead of the set interval circuit. As a result, too much molasses was dosed and the sugar content exceeded the maximum concentration of substrate inhibition. This caused a massive inhibition of the process.

Malfunction #2a: At fermentation time 3040 h the central recirculation pump failed, which prevented the system from mixing.

Malfunction #2b: At fermentation time 3050 h a failure the heating system occurred. This caused a temperature drop to 30 °C, at which the used microorganisms were no longer active. This caused a sharp drop in the production of hydrogen.

After restoring the correct fermentation temperature the hydrogen production rose again sharply. The residence time was then changed to 15 h. However, after a short-term increase in hydrogen formation, the trend reversed which forced a reset of the residence time to 20 h and 12L sewage sludge (ca. 5 % of the working volume) were inoculated (3350 h). There was a slight improvement in the H₂-formation, but it remained at a very moderate level. The main reason for the very modest production of H₂ was cross-contamination caused by the surrounding air. After another pump failure (3470 h) the hydrogen production decreased again. As a result about half of the fermenter volume was replaced and revaccinated with fresh inoculum to establish the origin population again.

Malfunction #3: At fermentation time 3750 h extremely low outer temperatures caused an iced water supply line, and as a result the fermenter could no longer be supplied with water. By metering in concentrated nutrient salts and native molasses the pipes were defrosted but this caused a renewed slump in the production of hydrogen.

The medium was then diluted and fresh inoculum added. Given the short time remaining for the fermentation At the end of the 15 h residence time the H₂ productivity rose back to 0.15 L/L/h with a respective H₂ yield of 3.5 mol/mol sucrose.

B. Measurement data

B.1 Pure gas measurements

Table B.1: Pure gas measurement results for membrane module M-2

Experimental conditions		Ideal selectivity			Permeance in $\text{Nm}^3/(\text{m}^2\cdot\text{s}\cdot\text{bar}) \cdot 10\text{E}-6$		
T in °C	p in bar	H ₂ /CO ₂	H ₂ /N ₂	CO ₂ /N ₂	H ₂	CO ₂	N ₂
30	2	4.23	n.d.	n.d.	42.6	10.1	n.d.
30	3.5	3.79	n.d.	n.d.	44.6	11.8	n.d.
30	5	3.81	n.d.	n.d.	45.9	12.	n.d.
30	6.5	3.71	156.65	42.17	46.7	12.6	0.3
30	8	3.56	131.85	37.02	47.4	13.3	0.4
30	9	3.51	164.88	47.04	48.1	13.7	0.3
30	10	3.47	n.d.	n.d.	48.2	13.9	n.d.
<i>average (30 °C)</i>		<i>3.70</i>	<i>145.96</i>	<i>39.43</i>	<i>46.2</i>	<i>12.5</i>	<i>0.3</i>
40	2	5.39	n.d.	n.d.	65.8	12.2	n.d.
40	3.5	4.55	n.d.	n.d.	65.6	14.4	n.d.
40	5	4.21	n.d.	n.d.	65.3	15.5	n.d.
40	6.5	4.03	n.d.	n.d.	64.7	16	n.d.
40	8	3.91	n.d.	n.d.	64.2	16.4	n.d.
40	9	3.80	n.d.	n.d.	63.8	16.8	n.d.
40	10	3.71	n.d.	n.d.	63.1	17	n.d.
<i>average (40 °C)</i>		<i>4.17</i>	<i>n.d.</i>	<i>n.d.</i>	<i>64.6</i>	<i>15.5</i>	<i>n.d.</i>
50	2	5.97	n.d.	n.d.	77.2	12.9	n.d.
50	3.5	4.69	n.d.	n.d.	78.2	16.7	n.d.
50	5	4.28	n.d.	n.d.	78.2	18.3	n.d.
50	6.5	4.10	n.d.	n.d.	78	19	n.d.
50	8	3.93	n.d.	n.d.	77.5	19.7	n.d.
50	9	3.86	n.d.	n.d.	77.3	20	n.d.
50	10	3.71	n.d.	n.d.	76.2	20.5	n.d.
<i>average (50 °C)</i>		<i>4.26</i>	<i>n.d.</i>	<i>n.d.</i>	<i>77.5</i>	<i>18.2</i>	<i>n.d.</i>

n.d.: not detected, because the volume flow rate was too low or not distinctly.

Table B.2: Pure gas measurement results for membrane module M-4

Experimental conditions		Ideal selectivity			Permeance in Nm ³ /(m ² .s.bar) *10E-6		
T in °C	p in bar	H ₂ /CO ₂	H ₂ /N ₂	CO ₂ /N ₂	H ₂	CO ₂	N ₂
30	2	3.84	n.d.	n.d.	143.1	37.3	n.d.
30	3.5	3.77	n.d.	n.d.	142.8	37.9	n.d.
30	5	3.61	139.29	38.62	144	39.9	1
30	6.5	3.61	n.d.	n.d.	144.6	40.1	n.d.
30	8	3.62	122.79	33.92	145.4	40.2	1.2
30	9	3.62	133.19	36.79	146	40.3	1.1
30	10	3.64	n.d.	n.d.	144.7	39.7	n.d.
<i>average (30 °C)</i>		<i>11.57</i>	<i>130.68</i>	<i>11.29</i>	<i>144.4</i>	<i>12.5</i>	<i>1.1</i>
40	2	3.99	n.d.	n.d.	173	43.3	n.d.
40	3.5	3.86	n.d.	n.d.	169.4	43.9	n.d.
40	5	3.81	n.d.	n.d.	168	44.1	n.d.
40	6.5	3.78	n.d.	n.d.	167.1	44.2	n.d.
40	8	3.78	n.d.	n.d.	166.8	44.1	n.d.
40	9	3.78	n.d.	n.d.	166.2	43.9	n.d.
40	10	3.78	n.d.	n.d.	167.4	44.3	n.d.
<i>average (40 °C)</i>		<i>3.83</i>	<i>n.d.</i>	<i>n.d.</i>	<i>168.3</i>	<i>44</i>	<i>n.d.</i>
50	2	3.99	n.d.	n.d.	186.6	46.8	n.d.
50	3.5	3.87	n.d.	n.d.	185	47.8	n.d.
50	5	3.88	n.d.	n.d.	184.4	47.5	n.d.
50	6.5	3.88	n.d.	n.d.	184.7	47.6	n.d.
50	8	3.92	n.d.	n.d.	185.2	47.2	n.d.
50	9	3.92	n.d.	n.d.	185.4	47.3	n.d.
50	10	3.90	n.d.	n.d.	185.3	47.5	n.d.
<i>average (50 °C)</i>		<i>3.91</i>	<i>n.d.</i>	<i>n.d.</i>	<i>185.2</i>	<i>47.4</i>	<i>n.d.</i>

n.d.: not detected, because the volume flow rate was too low or not distinctly.

Table B.3: Comparison of pure gas permeances before and after the field tests for membrane module M-2

Pressure difference	Permeance					
	N ₂		CO ₂		H ₂	
	before	after	before	after	before	after
in bar	in Nm ³ /(m ² .s.bar) *10E-6		in Nm ³ /(m ² .s.bar) *10E-6		in Nm ³ /(m ² .s.bar) *10E-6	
1	0.12	8.43	1.8	6.9	31.7	31
2	0.19	4.42	8.5	11.5	40.8	42.9
3	0.20	3.08	10.6	13	43.8	46.8
4	0.21	2.4	11.7	13.8	45.3	48.8
5	0.22	2.01	12.4	14.2	46.2	50
6	0.23	1.74	12.8	14.6	46.8	50.8
7	0.23	1.55	13.2	14.8	47.2	51.4
8	0.23	1.41	13.4	14.9	47.5	51.8
9	0.23	1.3	13.6	15.1	47.8	52.1
10	0.23	1.21	13.8	15.2	48	52.4

Table B.4: Comparison of ideal selectivities before and after the field tests for membrane module M-2

Pressure difference	Selectivity					
	H ₂ /N ₂		CO ₂ /N ₂		H ₂ /CO ₂	
	before	after	before	after	before	after
in bar	-	-	-	-	-	-
1	3.67	258.36	0.82	14.71	4.48	17.56
2	9.7	220.63	2.6	45.73	3.73	4.82
3	15.2	213.11	4.23	51.91	3.59	4.11
4	20.25	209.89	5.72	54.55	3.54	3.85
5	24.88	208.1	7.09	56.02	3.51	3.71
6	29.16	206.96	8.36	56.96	3.49	3.63
7	33.12	206.18	9.53	57.61	3.48	3.58
8	36.79	205.6	10.62	58.08	3.47	3.54
9	40.22	205.16	11.63	58.44	3.46	3.51
10	43.41	204.81	12.57	58.73	3.45	3.49

C. SEM pictures of fibers

The utilized scanning electron microscope (SEM) was provided by the Institute of Chemical Technologies and Analytics and the pictures were made under the guidance of Dipl. Ing. Marie-Christine Huemer and Dipl. Ing. Elke Ludwig. For preparation, the fibers were frozen by putting them into liquid nitrogen and subsequently broken.

C.1 Polyimide fibers

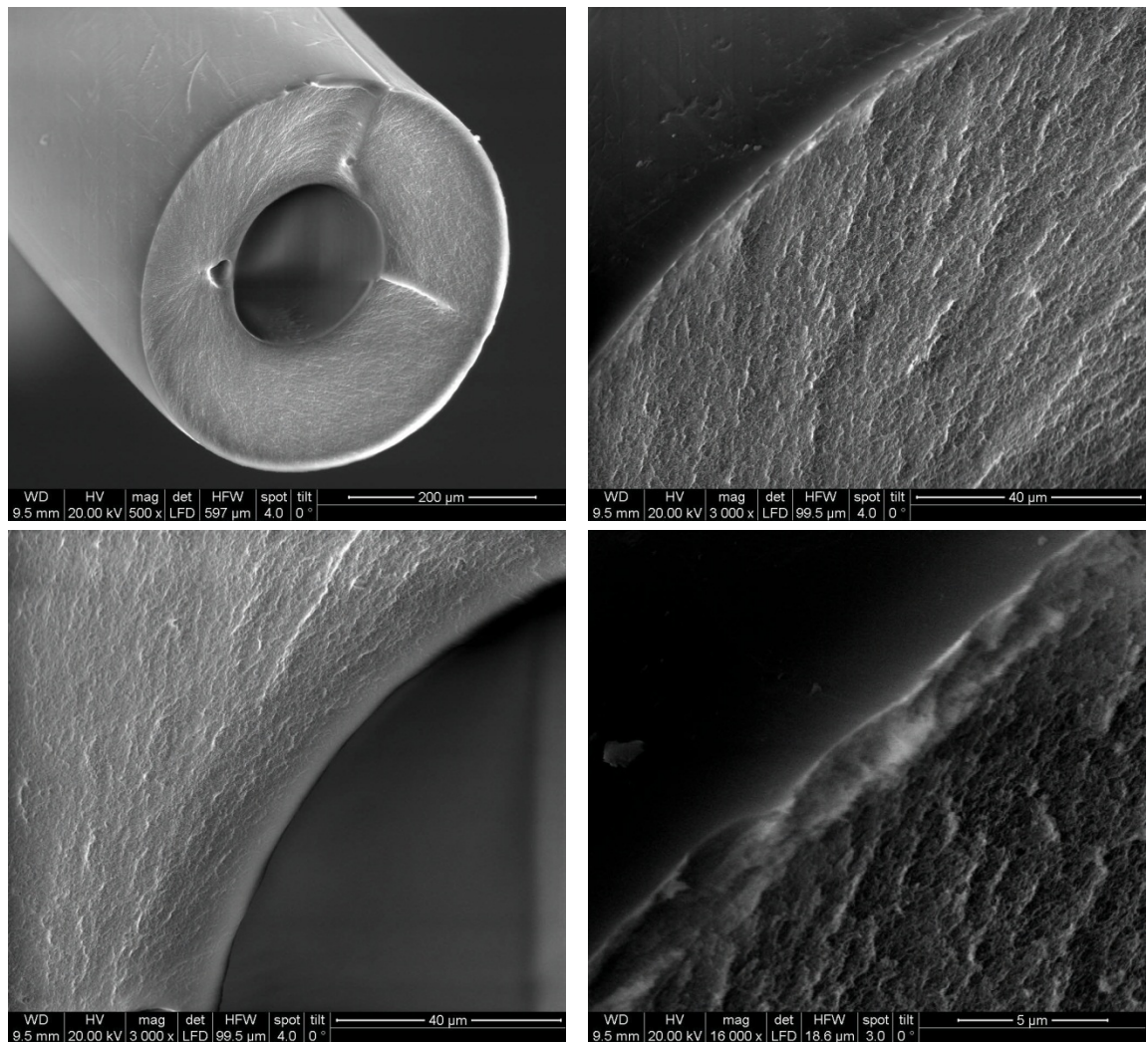


Figure C.1: SEM pictures of the utilized polyimide fibers, magnification: upper left x500, upper right x3000, lower left x3000, lower right x16000

C.2 Polypropylene fibers

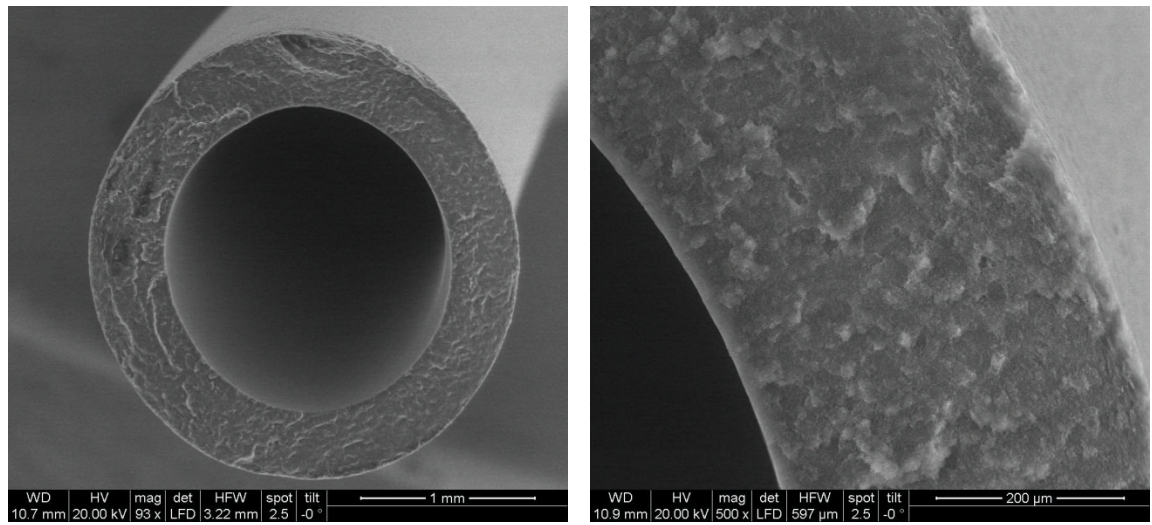


Figure C.2: SEM pictures of the utilized polypropylene fibers, magnification: left x93, right x500